Probing complex electron dynamics in multieclecton atoms and one electron molecule ion in presence of ultra short laser pulse

By

Kobra Nasiri Avanak

Submitted to the Department of Chemistry and the
Graduate Faculty of the University of Kansas
in partial fulfillment of the requirements for the degree of
Doctor of Philosophy

Shih-I Chu, Chairperson

Krzysztof Kuczera

Committee members

Thomas E. Cravens

Christopher Elles

Marco Caricato

Date defended: May 2nd, 2017

The Dissertation Committee for Kobra Nasiri Avanak certifies
that this is the approved version of the following dissertation :

Probing complex electron dynamics in multieclecton atoms and one electron molecule ion in presence of ultra short laser pulse

Shih-I Chu, Chairperson

Date approved: May 2nd, 2017

Abstract

We performed an *ab initio* and accurate exploration of complex electron dynamics in multieclecton atoms and one electron molecule ion in presence of ultra short laser pulse. Particularly, an *ab initio* 3D precision calculation and analysis of high-order harmonic generation (HHG) of one electron molecule ion subject to intense elliptically polarized laser pulses is presented along with the time-dependent generalized pseudospectral (TDGPS) method in two-center prolate spheroidal coordinates. The calculations are implemented for the ground and first excited electronic states of the interest molecule at the equilibrium internuclear separation as well as for the stretched molecule case. Weak even harmonics were detected in the HHG spectra of stretched molecules which were explained by the broken inversion symmetry due to dynamic localization of the electron density near one of the nuclei. A clear theoretical explanation of the phenomenon is given within the Floquet formalism. The studies in presence of laser field, proceed by investigation on anomalous dependence of near-threshold harmonics on the ellipticity of the driving near-infrared laser field which originates from the near-resonant excitation of π-symmetry molecular orbitals. In presence of linear polarized field, we also studied the sub-cycle transient multiphoton ionization dynamics of atomic and molecular systems subject to intense near-infrared laser fields on the sub-femtosecond time scale. Multiple ionization bursts within a single optical cycle are pronounced in the time-dependent ionization rates not only for some diatomic molecular ions but also for hydrogen atoms. The analysis of the electron density informs that several distinct density portions can be formed and separated from the target within half cycle of the laser field.

For the multi-electronic system, we present a comprehensive theoretical and computational study on harmonic generation (HG) of Li atoms in one- and two-photon Rabi-flopping regimes. Our all-electron approach is established on the time-dependent density-functional theory and includes polarization of the core and dynamic response of the electrons to the laser field. The results show that the population oscillations in the time domain with the Rabi frequency are reflected in the fine structure of the HG spectra and the finer structures of the harmonic peaks on the smaller frequency scale arise from the pulse-shape-related interference effects. These features are clearly seen in one-photon Rabi-flopping regime between some specific states however the pattern is more complex in the two-photon Rabi-flopping regime. Our findings can be used for developing coherent control methods for HG in the Rabi-flopping regime.

Acknowledgements

First and foremost, I would like to express my sincere gratitude to my advisor, Prof. Shih-I Chu, for giving me the opportunity to work with him and for his constant support, encouragement, guidance, and inspiration. His passion for science and beyond will be always in my memory. To me, he is not only a role model as the great scholar but also the great mentor in many aspects.

Also I would like to thank my committee members; Prof. Thomas Cravens, Prof. Krzysztof Kuczeran, Prof. Christopher Elles, and Prof. Marco Caricato for their suggestions and thoughtful review on this work.

My special thanks go to Prof. Dmitry A. Telnov for his insightful explanations and fruitful discussions, kind and friendly assistance and advice. It is my pleasure to thank former member of the group Dr. Sang-Kil Son and the other members of the group from National Taiwan university; Prof. Peng Cheng Li, Dr. John Heslar and Liao Sheng-Lun for all their help, advice, invaluable discussion and more importantly for making close friendship. I greatly appreciate all the supports from the Chemistry Department at University of Kansas. Particularly Prof. Braian Laird, the chair of Chemistry department at KU for his kindness and support.

With all my respects, I would like to thank my parents for their endless support and love from far distance. With all my hearts, I wish to thank my great office mate, my dear husband, Hossein who have been supportive in every way, and my dear son, Milan who always been a source of joy, love and happiness in my life.

I am so grateful to have my siblings who have cherished with me every great moment

and supported me whenever I needed it with their encouragement and love. I would like to thank all of the people who made this work possible.

Contents

List of Figures

List of Tables

Chapter 1

Introduction

The study of atomic and molecular processes in intense ultrashort laser fields is of great current interest in the forefront field of ultrafast science and technology. When the field strength is comparable to or exceeds to the Coulomb field experienced by outer-shell electrons in atoms, many of nonlinear optical phenomena in the strong-field regime, such as multiphoton excitation (MPE), ionization (MPI), and dissociation (MPD), above-threshold ionization (ATI) and dissociation (ATD), multiple high-order harmonic generation (HHG), etc. play significant roles. Multiphoton and above-threshold ionization of atoms and molecules in intense laser fields belongs to the most fundamental as well as explored and understood strong-field phenomena (see the review papers [79, 99]). Multiphoton ionization (MPI) is also an initial step in many other processes such as high harmonic generation [26] and high-order above-threshold ionization [96]. Novel phenomena including generation of attosecond pulses [46, 95], ultrafast molecular imaging [56, 76], attosecond photoelectron holography [8], electron diffraction [82, 103], etc. (see review in Ref. [67]) are also closely related to multiphoton ionization. Regarding the MPI measurements, since the first experiments on above-threshold ionization (ATI) [3], the research has been focused on the properties of the emitted electrons in the *energy* domain (electron energy spectra, which manifest the famous ATI peak structure). However, recent advances in laser technology opened a possibility of "clocking" the electron dynamics on a attosecond scale in the *time* domain [44, 114], thus in-

troducing a concept of attosecond metrology [67]. The time-domain analysis can uncover novel new features in the well-researched phenomenon of multiphoton ionization. On the other hand, the study of the high harmonic generation (HHG) dynamics and spectroscopy in intense laser fields is one of the forefront topics in ultrafast science and technology [73, 15]. Most of the studies so far have been focused on the use of linearly polarized (LP) laser fields, where the semiclassical 3-step model[26, 69] can provide qualitative understanding of the underlying processes. The use of elliptically polarized (EP) laser fields opens a new direction access to strong-field atomic, molecular, and optical (AMO) and chemical processes that are either hindered or not present under the linear polarization. Earlier study of HHG spectrum in EP fields showed that the HHG yield is decreased with increasing ellipticity [9, 77]. There have been also extensive studies of the polarization properties of HHG generated in atomic gases [33, 34, 83]. For the last decade, HHG has become the most important method for generating the extreme ultraviolet (XUV) attosecond pulses from intense infrared lasers [15, 67]. Since the HHG yield is sensitive to driving laser ellipticity, it has been found recently that the EP light can be used for the generation of isolated attosecond pulses via polarization gating [88]. The study of HHG in EP laser pulses is thus of considerable current interest both theoretically and experimentally [63, 39]. For the molecular systems, the extra internuclear degree of freedom and the ellipticity of the laser field provide extra control parameters for laser-molecule inter-actions and introduce some novel features in strong-field HHG processes. However, these extra degrees of freedom also pose considerable challenge for the accurate theoretical and computational study.

In strong field regime, all the above mentioned novel high-order processes cannot be treated by the traditional perturbative techniques. From the theoretical aspect, it requires a non-perturbative treatment to understand both the electronic structure and the multiphoton quantum dynamics. For the fully *ab initio* treatment of strong-field processes, one needs to solve the $3n+1$ dimensional non-relativistic time-dependent Schrödinger equation (TDSE) including the light–matter interaction term, where n is the number of electrons. This is a demanding task for $n \geq 2$.

In this dissertation, for one electronic atomic/molecular system, we present a time-dependent

generalized pseudospectral (TDGPS) approach in spherical/prolate spheroidal coordinates for fully *ab initio* nonperturbative treatment of multiphoton dynamics in intense laser fields. As for the multi electron systems like Li atoms interacting with strong laser fields, the system is described in the framework of the self-interaction-free time-dependent density-functional theory, taking into account dynamic multielectron response to the external field. Using the time-dependent generalized pseudospectral method with sufficient number of spatial grid points and time steps ensures the accuracy and efficiency of the computational procedure.

We successfully did some original research mainly focused on theoretical exploration of the strong-field multiphoton processes with novel theoretical and computational approaches in space and time. Our studies are mostly focused on development and application of fully *ab initio* theoretical formalisms and high-precision computational methods for the nonperturbative treatment of a broad range of highly nonlinear atomic molecular optics(AMO) multiphoton phenomena. We have uncovered the dynamical origins of several novel strong-field phenomena in ultrashort attosecond laser pulses for the first time.

In chapter 2, we perform an *ab initio* and accurate exploration of the sub-cycle transient multiphoton ionization dynamics of atomic and molecular systems subject to intense near-infrared laser fields on the sub-femtosecond time scale. The analysis of the electron density reveals that several distinct density portions can be shaped and detached from the target within half cycle of the laser field.

In chapter 3 and 4, we studied the high-order harmonic generation (HHG) of the hydrogen molecular ion subject to intense elliptically polarized laser pulses by means of the time-dependent generalized pseudospectral (TDGPS) method in two-center prolate spheroidal coordinates. The spectral and temporal structures of the HHG signal are explored by means of the wavelet time-frequency analysis. Several novel ellipticity-dependent dynamical behaviors are uncovered. We found that the production of above-threshold harmonics for non-zero ellipticity is generally reduced, as compared with linear polarized (LP) fields. However, below-threshold harmonics still appear quite strong except when the polarization plane is perpendicular to the molecular axis.

Weak even harmonics are detected in the HHG spectra of stretched molecules. This effect can be explained by the broken inversion symmetry due to dynamic localization of the electron density near one of the nuclei. An intuitive picture of the process is provided by the analysis of the time evolution of the electron density and time-frequency spectra of the dipole acceleration. A clear theoretical explanation of the phenomenon is given within the Floquet formalism.

In chapter 5, anomalous dependence of near-threshold harmonics in H_2^+ molecular ion on the ellipticity of the driving near-infrared laser field is studied theoretically based on accurate solution of the time-dependent Schrödinger equation in prolate spheroidal coordinates with the help of the generalized pseudospectral method. For these harmonics, the maximum radiation energy corresponds to a non-zero ellipticity of the driving field. Our analysis reveals that the origin of the phenomenon lies in the near-resonant excitation of π-symmetry molecular orbitals. The excited states responsible for the anomalous ellipticity dependence of different near-threshold harmonics are identified.

In chapter 6, we present a comprehensive theoretical and computational study on harmonic generation (HG) of Li atoms in one- and two-photon Rabi-flopping regimes where the population transfer from the ground $2s$ state to the excited $2p$, $3s$, and $3d$ states is substantial. Our all-electron approach is based on the time-dependent density-functional theory and takes into account polarization of the core and dynamic response of the electrons to the laser field. We show that the population oscillations in the time domain with the Rabi frequency Ω are reflected in the fine structure of the HG spectra in the frequency domain on the scale of 2Ω. Our results also manifest that even finer structures of the harmonic peaks on the smaller frequency scale originate from the pulse-shape-related interference effects. These features are clearly seen in one-photon Rabi-flopping regime and the pattern in the HG spectra becomes more complex in the two-photon Rabi-flopping regime. Our findings can be used for developing coherent control methods for HG in the Rabi-flopping regime.

Chapter 2

Theoretical methods in solving time-dependent Schrödinger equation in one electron molecule ions in presence of ultra short laser pulse

2.1 Introduction

We shall present a time-dependent method for numerical integration of the Schrödinger equation which is computationally efficient and capable of providing more accurate wavefunctions for reliable MPI and HHG calculations. The significant improvement of the time-dependent wavefunctions is obtained both by the use of a generalized pseudospectral method for a more optimal discretization of the spatial coordinates and by a new time propagation method presented. The method can be extended for the exploration of the dynamics and coherent control of HHG by intense ultrashort laser fields. We have the time-dependent Schrödinger equation as follow:

$$i\frac{\partial}{\partial t}\Psi(\boldsymbol{r},t) = H(t)\Psi(\boldsymbol{r},t), \tag{2.1}$$

where $H(t)$ is the full Hamiltonian, including the time-dependent interaction with the laser field:

$$H(t) = -\frac{1}{2}\nabla^2 + U(\boldsymbol{r}) + V(\boldsymbol{r},t). \tag{2.2}$$

In Eq. (2.2), $U(\boldsymbol{r})$ is the atomic (molecular) core potential and $V(\boldsymbol{r},t)$ is the interaction with the laser field. The latter is described within the electric dipole approximation:

$$V(\boldsymbol{r},t) = zF(t), \tag{2.3}$$

where $F(t)$ is the time-dependent field strength, and linear polarized case it is assumed along the z axis. Eq. (2.1) is solved with the help of the time-dependent generalized pseudospectral (TDGPS) method. First, the wave function and kinetic energy operator are discretized on a non-uniform and optimal spatial grids, with denser mesh nearby each nucleus and sparser mesh at longer range, leading to efficient and accurate solution with the use of only a modest number of spatial grid points. Further improvement of the accuracy is achieved by solving the problem in the finite volume which results in a denser grid for the same number of grid points. The boundary value R_b for the linear dimension of the volume is chosen large enough for proper description of the ionization dynamics. Details of the generalized pseudospectral (GPS) discretization scheme can be found in the next sections and also Refs. [23, 123] for the case of prolate spheroidal coordinates (diatomic molecular systems) and in Refs. [128, 125] for the case of spherical coordinates (atomic systems).

2.2 Time-dependent Schrödinger equation for the molecule of H_2^+ in the laser field

To calculate the ionization probability and HHG spectra, we solve the time-dependent Schrödinger equation for the molecule H_2^+ in the laser field. The initial wave function is an unperturbed eigen-

function of H_2^+. For our calculations, we pick the ground ($1\sigma_g$) and two excited ($1\sigma_u$ and $1\pi_u$) electronic states. The nuclei are fixed at their positions, and the nuclear motion is not taken into account. To describe the diatomic molecular ion H_2^+, we make use of the prolate spheroidal coordinates ξ, η, and φ which are related to the Cartesian coordinates x, y, and z as follows [2]:

$$x = a\sqrt{(\xi^2-1)(1-\eta^2)}\cos\varphi, \tag{2.4}$$

$$y = a\sqrt{(\xi^2-1)(1-\eta^2)}\sin\varphi, \tag{2.5}$$

$$z = a\xi\eta, (1 \le \xi < \infty, -1 \le \eta \le 1) \tag{2.6}$$

Here, we assume that the molecular axis is directed along the z axis, and the nuclei are positioned on this axis at the positions -a and a, so the internuclear separation $R = 2a$.

In the first step, we solve the unperturbed eigenvalue problem and obtain the eigenvalues and eigenfunctions:

$$[-\frac{1}{2}\nabla^2 + U(\xi,\eta)]\Psi(\xi,\eta,\varphi) = E\Psi(\xi,\eta,\varphi). \tag{2.7}$$

Here the kinetic energy operator in the prolate spheroidal coordinates reads as:

$$\begin{aligned} -\frac{1}{2}\nabla^2 = -\frac{1}{2a^2}\frac{1}{(\xi^2-\eta^2)}\Big[&\frac{\partial}{\partial\xi}(\xi^2-1)\frac{\partial}{\partial\xi} \\ &+ \frac{\partial}{\partial\eta}(1-\eta^2)\frac{\partial}{\partial\eta} + \frac{\xi^2-\eta^2}{(\xi^2-1)(1-\eta^2)}\frac{\partial^2}{\partial\varphi^2}\Big], \end{aligned} \tag{2.8}$$

and the Coulomb interaction term with the nuclei is as follows (the charge of each center is unity):

$$U(\xi,\eta) = -\frac{2\xi}{a(\xi^2-\eta^2)}. \tag{2.9}$$

For the unperturbed molecule, the projection m of the angular momentum onto the molecular axis

is conserved. Thus the wave function $\Psi(\xi,\eta,\varphi)$ can be represented in a separable form:

$$\Psi(\xi,\eta,\varphi) = \psi(\xi,\eta)\exp(im\varphi), \tag{2.10}$$

and separate eigenvalue problems for different $|m|$ are obtained:

$$\begin{aligned} &-\frac{1}{2a^2}\frac{1}{(\xi^2-\eta^2)}\Big[\frac{\partial}{\partial\xi}(\xi^2-1)\frac{\partial}{\partial\xi}+\frac{\partial}{\partial\eta}(1-\eta^2)\frac{\partial}{\partial\eta} \\ &-\frac{m^2}{\xi^2-1}-\frac{m^2}{1-\eta^2}\Big]\psi_m-\frac{2\xi}{a(\xi^2-\eta^2)}\psi_m = E\psi_m. \end{aligned} \tag{2.11}$$

To solve eq. (2.11), we first convert it to equivalent variational forms, which is different for even and odd m. This is done to provide accurate numerical solutions of the differential equations for both even and odd projections of angular momentum (note that the exact eigenfunctions have factors $(\xi^2-1)^{|m|/2}(1-\eta^2)^{|m|/2}$ which are non-analytical at nuclei for odd $|m|$). The variational forms of eq.(2.11)are as follows:

$$\begin{aligned} &\delta\Big(\frac{1}{2a^2}\int_1^\infty d\xi\int_{-1}^1 d\eta\Big[(\xi^2-1)\frac{\partial\psi_m^*}{\partial\xi}\frac{\partial\psi_m}{\partial\xi}+(1-\eta^2)\frac{\partial\psi_m^*}{\partial\eta}\frac{\partial\psi_m}{\partial\eta} \\ &+\Big(\frac{m^2}{\xi^2-1}+\frac{m^2}{1-\eta^2}\Big)\psi_m^*\psi_m\Big]-\frac{2}{a}\int_1^\infty d\xi\int_{-1}^1 d\eta\,\xi\,\psi_m^*\psi_m - E\int_1^\infty d\xi\int_{-1}^1 d\eta(\xi^2-\eta^2)\psi_m^*\psi_m\Big) = 0 \end{aligned} \tag{2.12}$$

for even $|m|$ and

$$\begin{aligned} &\delta\Big(-\frac{2}{a}\int_1^\infty d\xi\int_{-1}^1 d\eta\,\xi\,\psi_m^*\psi_m+\frac{1}{2a^2}\int_1^\infty d\xi\int_{-1}^1 d\eta\Big[\frac{(\xi^2-1)^2}{\xi^2}\frac{\partial}{\partial\xi}\Big(\frac{\xi}{\sqrt{\xi^2-1}}\psi_m^*\Big)\frac{\partial}{\partial\xi}\Big(\frac{\xi}{\sqrt{\xi^2-1}}\psi_m\Big) \\ &+\frac{(1-\eta^2)^2}{\eta^2}\frac{\partial}{\partial\eta}\Big(\frac{\eta}{\sqrt{1-\eta^2}}\psi_m^*\Big)\frac{\partial}{\partial\eta}\Big(\frac{\eta}{\sqrt{1-\eta^2}}\psi_m\Big)+\Big[\frac{m^2-1}{\xi^2-1}+\frac{m^2-1}{1-\eta^2}+2+\frac{2}{\xi^2}\Big]\psi_m^*\psi_m\Big] \\ &-E\int_1^\infty d\xi\int_{-1}^1 d\eta(\xi^2-\eta^2)\psi_m^*\psi_m\Big) = 0 \end{aligned} \tag{2.13}$$

2.3 Time-dependent pseudospectral discretization(TDGPS) method

For atomic structure calculations involving the Coulomb potential, one typical problem associated with commonly used equal-spacing grid methods is the Coulomb singularity at $r = 0$ and the long range nature of the potential. Generally one truncates the semi-infinite $(0,\infty)$ domain into finite domain $[r_{min}, r_{max}]$ to avoid the Coulomb singularity at the origin and the infinite domain. For this purpose, r_{min} must be chosen sufficiently small and r_{max} sufficiently large. This results in the need of a large number of grid points. Further, extreme care must be exercised to ensure the wavefunctions obtained from such discretization is of sufficient accuracy for performing reliable high-order harmonic generation calculations. For optimal discretization of the radial coordinates to overcome some of the above mentioned problems, we take advantage of extended generalized pseudospectral (GPS)approach in molecules. Then we apply pseudospectral discretization to Eqs.(2.12) and (2.13). The coordinate ξ is mapped to the interval $[-1,1]$ according to the following formulas:

$$\begin{aligned} \xi &= 1 + R_l \frac{1+x}{1-x+\dfrac{2R_l}{R_b-1}} \\ \xi' \equiv \frac{d\xi}{dx} &= 2R_l \frac{1+\dfrac{R_l}{R_b-1}}{(1-x+\dfrac{2R_l}{R_b-1})^2} \end{aligned} \tag{2.14}$$

Here R_l and R_b are the parameters of the transformation (2.14). The parameter R_b is the maximum value of the coordinate ξ; it corresponds to $x = 1$. Making this parameter finite, we can solve the problem in the finite volume around the nuclei that significantly improves the accuracy. The zero boundary conditions are imposed on the wave function at $\xi = R_b$. In the time-independent calculations, R_b value is large enough to ensure high accuracy of sufficient number of both discrete and continuous eigenstates. When solving the time-dependent equation in the laser field, some measures should be taken to prevent an unphysical reflection from the boundary. We use an absorbing layer located before R_b which smoothly brings down the wave function and prevents the reflection.

The variable x is discretized using the Legendre–Gauss–Radau scheme (x_i are the collocation points and w_i are the quadrature weights)[2]:

$$\begin{aligned} x_i: \qquad & P_{N_x}(x_i) - P_{N_x+1}(x_i) = 0 \\ & w_i^x = \frac{1}{(N_x+1)^2} \frac{1+x_i}{[P_{N_x}(x_i)]^2} \end{aligned} \tag{2.15}$$

Here N_x is the number of collocation points used, $P_{N_x}(x)$ is the Legendre polynomial; the collocation points are obtained as roots of the difference of two polynomials with orders N_x and N_x+1, respectively. The Gauss–Radau scheme allows easily implement boundary conditions at the end of the interval since $x = 1$ is always a collocation point, irrespectively of N_x. The integration and differentiation formulas in the Legendre–Gauss–Radau scheme can be written as follows ($f(x)$ is an arbitrary function):

$$\int_{-1}^{1} f(x)dx = \sum_{i=1}^{N_x+1} f(_i) w_i^x \tag{2.16}$$

$$\frac{df}{dx}(x_i) = \sum_{i=1}^{N_x+1} D_{ii'}^x f(x_{i'}) \tag{2.17}$$

Here the derivative matrix $D_{ii'}^x$ is defined as follows:

$$D_{ii'}^x = d_{ii'}^x \frac{(1+x_{i'})P_{N_x}(x_i)}{(1+x_i)P_{N_x}(x_{i'})} \tag{2.18}$$

$$\begin{aligned} d_{ii'}^x &= \frac{1}{x_i - x_{i'}} (i \neq i') \\ d_{ii}^x &= \frac{1}{2(1+x_i)} \\ d_{N_x+1,N_x+1}^x &= \frac{1}{4} N_x(N_x+2) \end{aligned} \tag{2.19}$$

The coordinate η does not need any additional mapping transformation since it originally spans the interval $[-1,1]$. However, in the most general case such a transformation can be applied, so we will assume that η is mapped to the variable y within the interval $[-1,1]$ (in practical calculations we used the identity transformation $\eta = y$). Unlike the variable x, we discretize y using the Legendre–Gauss scheme for we don't have to apply any boundary conditions at the points $y = \pm 1$. The collocation points for this scheme are defined as the roots of the Legendre polynomial P_{N_y} , and the quadrature weights are expressed through the derivatives of this polynomial (N_y is the number of collocation points used)[2]:

$$\begin{aligned} y_j: \qquad & P_{N_y}(y_j) = 0 \\ & w_j^y = \frac{1}{(1-y_j^2)[P'_{N_y}(y_j)]^2} \end{aligned} \tag{2.20}$$

The integration and differentiation in the Legendre–Gauss scheme are performed as follows ($g(y)$ is an arbitrary function):

$$\int_{-1}^{1} g(y)dy = \sum_{j=1}^{N_y+1} g(y_j)w_j^y \tag{2.21}$$

$$g'(y_j) = \sum_{j'=1}^{N_y} D^y_{jj'} g(y_{j'}), \qquad D^y_{jj'} = d^y_{jj'} \frac{P'_{N_y}(y_j)}{P'_{N_y}(y_{j'})} \tag{2.22}$$

with the derivative matrix $d^y_{jj'}$ defined as

$$d^y_{jj'} = \frac{1}{y_j - y_{j'}} (j \neq j'), \qquad d^y_{jj} = \frac{y_j}{1-y_j^2} \tag{2.23}$$

Once the basic expressions of the pseudospectral discretization are established by Eqs.(2.15)–(2.23), one can proceed to discretize the variational eigenvalue problems (2.12) and (2.13). The matrix

eigenvalue problems which appear upon discretization of eq.(2.11) can be written as follows for even m values:

$$\sum_{i'j'}\Big[T^{e}_{ij;i'j'}+\Big(\frac{m^2}{2a^2(\xi_i^2-1)(1-\eta_j^2)}-\frac{2\xi_i}{a(\xi_i^2-\eta_j^2)}\Big)\delta_{ii'}\delta_{jj'}\Big]\phi_{m;i'j'}=E\phi_{m;i'j'} \tag{2.24}$$

and odd m values:

$$\sum_{i'j'}\Big[T^{o}_{ij;i'j'}+\Big(\frac{m^2-1}{2a^2(\xi_i^2-1)(1-\eta_j^2)}+\frac{1+\xi_i^{-2}}{a(\xi_i^2-\eta_j^2)}-\frac{2\xi_i}{a(\xi_i^2-\eta_j^2)}\Big)\delta_{ii'}\delta_{jj'}\Big]\phi_{m;i'j'}=E\phi_{m;i'j'} \tag{2.25}$$

respectively. Here the quantities $\phi_{m;i'j'}$ are related to the wave function at the discretized coordinates:

$$\psi_m(\xi_i,\eta_j)=\frac{\phi_{m;i'j'}}{\sqrt{\xi_{i'}\eta_{j'}}}\sqrt{\frac{1-y_j^2}{1+x_i^2}}\frac{P_{N_x}(x_i)P'_{N_y}(y_j)}{\sqrt{\xi_i^2-\eta_j^2}} \tag{2.26}$$

$P_{N_x}(x)$ and $P'_{N_y}(y)$ being the Legendre polynomial and its derivative, respectively. The kinetic energy matrices $T^{e}_{ij;i'j'}$ and $T^{o}_{ij;i'j'}$ are calculated as follows:

$$\begin{aligned}T^{e}_{ij;i'j'}=&\frac{1}{2a^2}\frac{1}{\sqrt{(\xi_i^2-\eta_j^2)(\xi_{i'}^2-\eta_{j'}^2)}}\times\Big[\delta_{jj'}\sqrt{\frac{(1+x_i)(1+x_{i'})}{\xi_i\xi_{i'}}}\sum_{k=1}^{N_x}\frac{\xi_k^2-1}{\xi_k'(1+x_k)}d^x_{ki}d^x_{ki'}\\&+\delta_{ii'}\sqrt{\frac{(1-y_j^2)(1-y_{j'}^2)}{\eta_j'\eta_{j'}'}}\sum_{k=1}^{N_y}\frac{1-\eta_k^2}{\eta_k'(1-y_k^2)}d^y_{kj}d^y_{kj'}\Big]\end{aligned} \tag{2.27}$$

and

$$\begin{aligned}T^{o}_{ij;i'j'}=&\frac{1}{2a^2}\frac{1}{\sqrt{(\xi_i^2-\eta_j^2)(\xi_{i'}^2-\eta_{j'}^2)}}\times\Big[\delta_{jj'}\frac{\xi_i\xi_{i'}}{\sqrt{\xi_i'\xi_{i'}'}}\sqrt{\frac{(1+x_i)(1+x_{i'})}{(\xi_i^2-1)(\xi_{i'}^2-1)}}\sum_{k=1}^{N_x}\frac{(\xi_k^2-1)^2}{\xi_k^2\xi_k'(1+x_k)}d^x_{ki}d^x_{ki'}\\&+\delta_{ii'}\frac{1}{\sqrt{\eta_j'\eta_{j'}'}}\sqrt{\frac{(1-y_j^2)(1-y_{j'}^2)}{(1-\eta_j^2)(1-\eta_{j'}^2)}}\sum_{k=1}^{N_y}\frac{(1-\eta_k^2)^2}{\eta_k'(1-y_k^2)}d^y_{kj}d^y_{kj'}\Big]\end{aligned} \tag{2.28}$$

The discretized coordinates ξ_i and η_j as well as the collocation points x_i and y_j are defined in the Appendix. Note that the potential terms are diagonal in the pseudospectral method. They are represented by their values at the discretized coordinates, so no calculation of potential energy matrix elements is required. The kinetic energy matrices are given by simple analytical expressions (2.27) and (2.28)) which can be readily programmed into the computer code. Straightforward programming implementation and high accuracy for moderate number of collocation points constitute the most attractive features of the generalized pseudospectral method. Solving the eigenvalue problems (2.24) and (2.25), we obtain unperturbed energy values and eigenstates of H_2^+ which are used as initial states for time propagation as well as for construction of propagation matrices.

2.4 Time evolution of wave function in the laser field

The time-dependent Schrödinge equation in the laser field is solved by means of the split-operator method in the energy representation. We employ the following split-operator, second-order short-time propagation formula:

$$\begin{aligned}\Psi(\boldsymbol{r},t+\Delta t) = \exp\left[-i\frac{\Delta t}{2}H_0(\boldsymbol{r})\right] \times \exp\left[-i\Delta t V(\xi,\eta,t+\frac{\Delta t}{2}\right] \\ \times \exp\left[-i\frac{\Delta t}{2}H_0(\boldsymbol{r})\right]\Psi(\boldsymbol{r},t) + O(\Delta t^3).\end{aligned} \tag{2.29}$$

Here Δt is the time propagation step, H_0 is the unperturbed electronic Hamiltonian which includes the kinetic energy and the interaction with the nuclei, $V(\xi,\eta,t)$ is the term due to the coupling to the external field. If the laser field is linearly polarized, the dipole approximation is well justified. Without loss of generality, we can also assume that the polarization vector of the field lies in the plane x–z. Then using the length gauge, we can write the interaction potential $V(\xi,\eta,t)$ in the following form:

$$V(\xi,\eta,\varphi,t) = \mathbf{r}.\mathbf{F}(t) = a\xi\eta F_z. \tag{2.30}$$

The time-dependent function $F(t)$ contains the carrier and envelope factors. In our calculations, we use the sine-squared pulse shape, then the function $F(t)$ can be written as follows:

$$F(t) = F_0 \sin^2\left(\frac{\pi t}{NT}\right) \tag{2.31}$$

Here F_0 is the peak field amplitude, $T = 2\pi/\omega_0$ is the duration of one optical cycle, and N is the number of optical cycles in the pulse. The time propagation process based on Eq.(2.29) can be described as follows. Since the unperturbed Hamiltonian commutes with the projection of the angular momentum on the molecular axis, the field-free propagator $\exp\left(-i\frac{\Delta t}{2}H_0\right)$ is block-diagonal and can be represented in the following form:

$$\exp\left[-i\frac{\Delta t}{2}H_0\right] = \sum_{m=-\infty}^{\infty} \exp\left[-i\frac{\Delta t}{2}H_0^{(|m|)}\right] |m><m| \tag{2.32}$$

where $H_0^{(|m|)}$ are the unperturbed Hamiltonian corresponding to particular angular momentum projections m, as expressed by Eqs.(2.25) and (2.26), and $|m><m|$ are the projecting operators onto the states with definite m. The propagator matrices $\exp\left[-i\frac{\Delta t}{2}H_0^{(|m|)}\right]$ are built of the unperturbed eigenvectors $\psi_k^{(|m|)}$ and eigenvalues $E_k^{(|m|)}$ when the eigenvalue problems (2.25) and (2.26) are solved:

$$\exp\left[-i\frac{\Delta t}{2}H_0^{(|m|)}\right] = \sum_k \exp\left[-i\frac{\Delta t}{2}E_k^{(|m|)}\right] \times |\psi_k^{(|m|)}><\psi_k^{(|m|)}| \tag{2.33}$$

Working in the energy representation, we can control the contributions to the sum (2.33). For example, removing the contributions with very high energies, we can get rid of spurious transitions to irrelevant regions of the energy spectrum and improve the numerical stability of the propagation. To apply the propagator in the form (2.32), we expand the total time-dependent wave function in the Fourier series with respect to the angular coordinate φ:

$$\Psi(\xi,\eta,\varphi,t) = \sum_{m=-\infty}^{\infty} \psi_m(\xi,\eta,t)\exp(im\varphi) \tag{2.34}$$

Then each term in the series (2.34) is acted upon by only one term in the series (2.32), and the result of the field-free propagation can be written as follows:

$$\begin{aligned}\Psi^{(1)}(\xi,\eta,\varphi,t) &\equiv \exp\Big[-i\frac{\Delta t}{2}H_0^{(|m|)}\Big]\Psi(\xi,\eta,\varphi,t)\\ &= \sum_{m=-\infty}^{\infty}\exp(im\varphi)\exp\Big[-i\frac{\Delta t}{2}H_0^{(|m|)}\Big]\psi_m(\xi,\eta,t)\end{aligned} \tag{2.35}$$

Using this procedure for the field-free propagation step, we can significantly reduce the dimensions of the propagator matrices and speed up the computations. In practical calculations, the infinite series (2.34) should be truncated. We found that for the calculations in linear polarized field, retaining the m values -8 to 8 is sufficient to get converged results. The external field operator $\exp\Big(-i\Delta t V\Big)$ is a multiplication in coordinate representation when using the length gauge, and the next part of the short-time propagation is achieved straightforwardly:

$$\Psi^{(2)}(\xi,\eta,\varphi,t) \equiv \exp\Big[-i\Delta t V(\xi,\eta,\varphi,t+\frac{1}{2}\Delta t)\Big]\Psi^{(1)}(\xi,\eta,\varphi,t) \tag{2.36}$$

Then $\Psi^{(2)}(\xi,\eta,\varphi,t)$ is re-expanded in the Fourier series:

$$\Psi^{(2)}(\xi,\eta,\varphi,t) = \sum_{m=-\infty}^{\infty}\psi_m^{(2)}(\xi,\eta,t)\exp(im\varphi) \tag{2.37}$$

and the next unperturbed propagation is applied:

$$\begin{aligned}\Psi^{(3)}(\xi,\eta,\varphi,t) &\equiv \exp\Big[-i\frac{\Delta t}{2}H_0\Big]\Psi^{(2)}(\xi,\eta,\varphi,t)\\ &= \sum_{m=-\infty}^{\infty}\exp(im\varphi)\exp\Big[-i\frac{\Delta t}{2}H_0^{(|m|)}\Big]\psi_m^{(2)}(\xi,\eta,t)\end{aligned} \tag{2.38}$$

This completes the short-time propagation according to Eq.(2.29) since $\Psi^{(3)}$ is the wave function Ψ at the time $t+\Delta t$: The procedure described above is to be applied sequentially starting at $t=0$ and ending at $t=T$. As a result, the wave function $\Psi(\xi,\eta,\varphi)$ is obtained on a uniform time grid within the interval $[0,T]$.

2.5 Calculation of HHG spectra in presence of laser field

Once the wave function is computed, we can proceed to calculate the spectra of the emitted high-order harmonic radiation. To calculate the HHG spectra, we employ the widely-used semi-classical approach, replacing the classical quantities with the corresponding quantum expectation values. The spectral density of the radiation energy emitted for all the time is given either by the length form

$$S(\omega) = \frac{2\omega^4}{3\pi c^3}|\boldsymbol{D}_\omega|^2, \tag{2.39}$$

or acceleration form,

$$S(\omega) = \frac{2}{3\pi c^3}|\boldsymbol{A}_\omega|^2. \tag{2.40}$$

Here $\boldsymbol{D}_\omega$ and $\boldsymbol{A}_\omega$ are the Fourier transforms of the time-dependent dipole moment and dipole acceleration, respectively.

$$\boldsymbol{D}_\omega = \int_{-\infty}^{\infty} dt \mathbf{D}(t)\exp(i\omega t), \tag{2.41}$$

$$\boldsymbol{A}_\omega = \int_{-\infty}^{\infty} dt \mathbf{A}(t)\exp(i\omega t). \tag{2.42}$$

The time-dependent dipole moment and acceleration are evaluated as expectation values with the time-dependent wave function $\Psi(\xi,\eta,\varphi,t)$

$$\boldsymbol{D}(t) = \langle\Psi|\mathbf{r}|\Psi\rangle, \tag{2.43}$$

$$\boldsymbol{A}(t) = -\langle\Psi|(\overrightarrow{\nabla}U)|\Psi\rangle - \mathbf{f}(t), \tag{2.44}$$

2.6 Wavelet time-frequency spectra

The dynamics of the HG process can be explored in more detail using the time-frequency analysis of the dipole acceleration by means of the wavelet transformation [24]:

$$\tilde{\boldsymbol{A}}_{\mathrm{w}}(\omega,t) = \sqrt{\omega}\int_{-\infty}^{\infty} dt' W[\omega(t'-t)]\boldsymbol{A}(t'). \tag{2.45}$$

For our purposes, the natural choice of the mother wavelet $W(x)$ is the Morlet wavelet:

$$W(x) = \exp(ix)\exp\left(-\frac{x^2}{2\tau^2}\right), \tag{2.46}$$

so Eq. (2.45) represents a type of short-time Fourier transform. For the window width parameter τ, we use the value $\tau = 15$, previously tested and adopted for the time-frequency analysis of HG signals [23, 131]. The quantity $\tilde{\boldsymbol{A}}_{\mathrm{w}}(\omega,t)$ provides the time profile of the harmonic with the frequency ω and thus reveals what parts of the laser pulse on the time scale are mainly responsible for generation of the harmonic signals with specific frequencies.

Chapter 3

Sub-cycle Transient Structures in Time-dependent Multiphoton Ionization Rates

3.1 Introduction

Multiphoton ionization (MPI) is an initial step in many processes such as high harmonic generation [26] and high-order above-threshold ionization [96]. The time-domain analysis of MPI can uncover novel new features in the well-researched phenomenon of multiphoton ionization. Recently, a theoretical study on H_2^+ in an intense infrared laser field [118, 119] revealed multiple ionization bursts within a half-cycle of the laser field oscillation. The phenomenon was explained by transient electron localization near one of the nuclei on the attosecond time scale [118], which is in turn related to existence of two electronic states with opposite parities strongly coupled by the field (the charge resonance states [92]). Here, we show that multiple ionization bursts per half-cycle of the laser field can exist not only in homonuclear molecules with odd number of electrons, which possess the charge resonance states, but also in heteronuclear molecules, and even in atoms. To the best of our knowledge, this is the first time sub-cycle transient structures in time-dependent MPI

rates are reported for heteronuclear molecules and atoms.

3.2 Theoretical method to calculate the time-dependent MPI rates

In this chapter, we analyze the time-dependent MPI rates of three one-electron systems, the hydrogen atom and molecular ions H_2^+ and HHe^{2+}. We solve the time-dependent Schrödinger equation

$$i\frac{\partial}{\partial t}\Psi(\boldsymbol{r},t) = H(t)\Psi(\boldsymbol{r},t), \tag{3.1}$$

where $H(t)$ is the full Hamiltonian, including the time-dependent interaction with the linear polarized field along z axis.laser field: Eq. (3.1) is solved with the help of the time-dependent generalized pseudospectral (TDGPS) method as we explained in details in chapter 2. To achieve high accuracy in the present calculations, we use 160 grid points for the radial (pseudoradial) coordinate and 32 grid points for the angular (pseudoangular) coordinate.

Since the atomic and molecular systems subject to laser fields can be ionized, only outgoing wave components (describing ionization) should be present in the wave function at large distances from the core. Thus the correct boundary conditions for the wave function are the outgoing-wave boundary conditions. In our present calculations, the boundary conditions are imposed by an absorber placed at some distance from the core (in the layer between the length values R_a and R_b). The absorber prevents the electron density from moving back to the core thus imposing the outgoing-wave boundary conditions.

For the time evolution of the wave function, we employ the following split-operator, second-order short-time propagation formula:

$$\Psi(\boldsymbol{r},t+\Delta t) = \exp\left(-\frac{i}{2}\Delta t\, H_0\right) \times \exp\left(-i\Delta t\, V(\boldsymbol{r},t+\frac{1}{2}\Delta t)\right) \times \exp\left(-\frac{i}{2}\Delta t\, H_0\right)\Psi(\boldsymbol{r},t) + O((\Delta t)^3). \tag{3.2}$$

Here Δt is the time propagation step, H_0 is the unperturbed electronic Hamiltonian which includes the kinetic energy and the core potential. The operator $\exp\left(-\frac{i}{2}\Delta t\, H_0\right)$ is constructed by the spectral expansion:

$$\exp\left(-\frac{i}{2}\Delta t\, H_0\right) = \sum_n \exp\left(-\frac{i}{2}\Delta t\, E_n\right) |\psi_n\rangle\langle\psi_n| \tag{3.3}$$

where ψ_n and E_n are the eigenvectors and eigenvalues, respectively, of the unperturbed Hamiltonian H_0. In practical calculations, the summation in (3.3) includes all eigenvectors with the energies $E_n < E_b$ where the upper limit E_b should be large enough to describe all relevant physical processes. With the control of high-energy contributions to the propagator matrix, we can avoid population of physically irrelevant regions of the energy spectrum and improve numerical stability of the computations. In the present work, we use E_b=10 a.u.; this is a reasonable value for the carrier frequency and intensities of the laser field used in the present calculations. For the given Δt, the propagator matrix $\exp\left(-\frac{i}{2}\Delta t\, H_0\right)$ is time-independent and constructed only once before the propagation process starts. The matrix $\exp\left(-i\Delta t\, V(\boldsymbol{r}, t+\frac{1}{2}\Delta t)\right)$ is time-dependent and must be calculated at each time step. However, for the interaction with the laser field in the length gauge, this matrix is diagonal in the GPS method, and its calculation is not time-consuming (all potential terms are represented by their values on the coordinate grid and appear as diagonal matrices in the GPS method; no calculation of potential energy matrix elements is required). In the present work, we use 4096 time steps per optical cycle; this is enough to achieve convergence for the intensities and wavelengths used in the calculations.

Because of the absorber, the normalization integral of the wave function $\Psi_{n\sigma}(\boldsymbol{r}, t)$ decreases in time. The parts of the wave packet absorbed in the layer between the distance values R_a and R_b describe unbound states populated during the ionization process.

The time-dependent ionization rate can be defined as a logarithmic derivative of the time de-

pendent population $P(t)$:

$$P(t) = \int_{r \leq R_b} d^3 r |\Psi(\boldsymbol{r},t)|^2, \tag{3.4}$$

$$\Gamma(t) = -\frac{d}{dt} \ln P(t). \tag{3.5}$$

We have performed a series of calculations on H, H_2^+, and HHe^{2+} for the laser fields with several intensities and wavelengths in the near-infrared range (780 nm to 1064 nm). The sub-cycle structures appear a universal feature of multiphoton ionization and become well pronounced for sufficiently strong laser fields. Here we report some representative results. For the diatomic molecules H_2^+ and HHe^{2+}, we report the time-dependent MPI rates obtained from the Floquet states in the monochromatic laser field. The scheme for the calculation of the Floquet states is similar to that for the calculation of ordinary time-dependent wave functions but includes an additional procedure for construction and diagonalization of the one-optical-cycle propagator (see Ref. [121]).

3.2.1 Sub-cycle structures in time-dependent ionization rate of H_2^+

For H_2^+, we choose a stretched configuration for the ground electronic $1\sigma_g$ state with the internuclear separation $R = 3$ a.u. This makes the ionization potential lower and allows to obtain noticeable ionization rates for moderate laser intensities. In Fig. 3.1, we show the results for the field with the wavelength 800 nm and intensity 1×10^{14} W/cm^2, with the molecular axis orientation parallel to the laser field. In this calculation, we use $R_b = 50$ a.u. and $R_a = 30$ a.u. As expected, the MPI rate has two main maxima per optical cycle, corresponding to the peak values of the laser field. However, each maximum is split in two subpeaks with the local minimum between them.

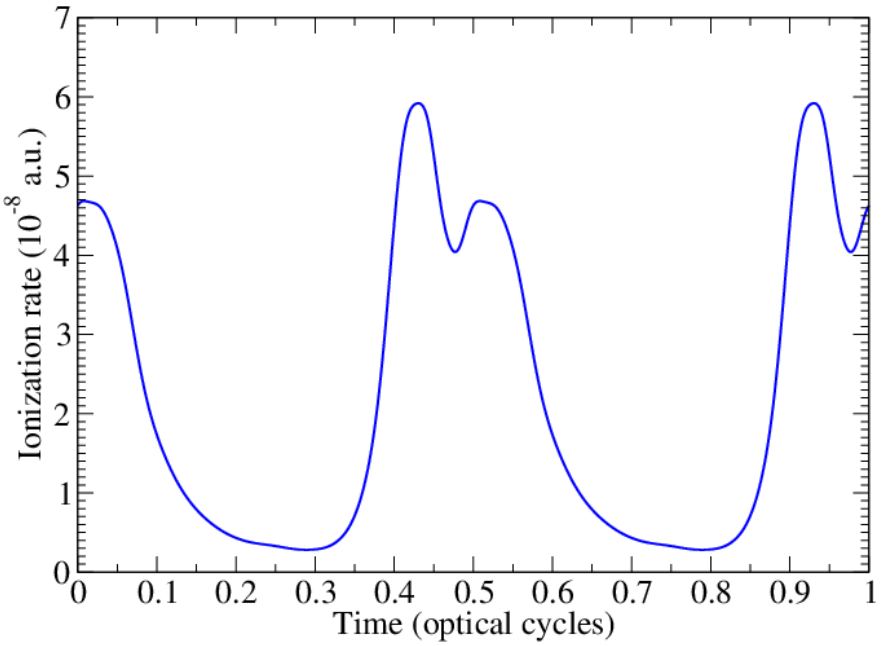

Figure 3.1: Time-dependent ionization rate of H_2^+ at the internuclear separation of 3 a.u. (Floquet state originating from the unperturbed $1\sigma_g$ state) calculated as a logarithmic derivative of the population within the sphere with the radius 50 a.u. The wavelength of the laser field is 800 nm and the intensity is 1×10^{14} W/cm^2.

3.2.2 Sub-cycle structures in time-dependent ionization rate of of HHe^{2+}

For HHe^{2+}, the bonding orbital is not the ground electronic state but the first excited state 2σ. We have performed the calculations for the internuclear separation of 4 a.u. which is close to the equilibrium distance. The laser field has the wavelength 780 nm, intensity 5×10^{13} W/cm^2, and is directed along the molecular axis. Here we use $R_b = 40$ a.u. and $R_a = 20$ a.u. The results for the MPI rate are shown in Fig. 3.2. As for the H_2^+ molecule, we can see two main maxima per optical cycle corresponding to the peak values of the laser field. However, unlike the H_2^+ case, the MPI rates at these maxima are different: the positive and negative directions of the field are not equivalent for HHe^{2+} because of its heteronuclear nature. Each main maximum is again split into subpeaks. Since HHe^{2+} is a heteronuclear diatomic molecule with highly asymmetric electron density distribution, we can conclude that the fine subpeak structure of the time-dependent MPI rate is not related to the two-center nature of the molecule but shaped in the vicinity of one nucleus only. This observation is confirmed by our calculations of the hydrogen atom in the laser field.

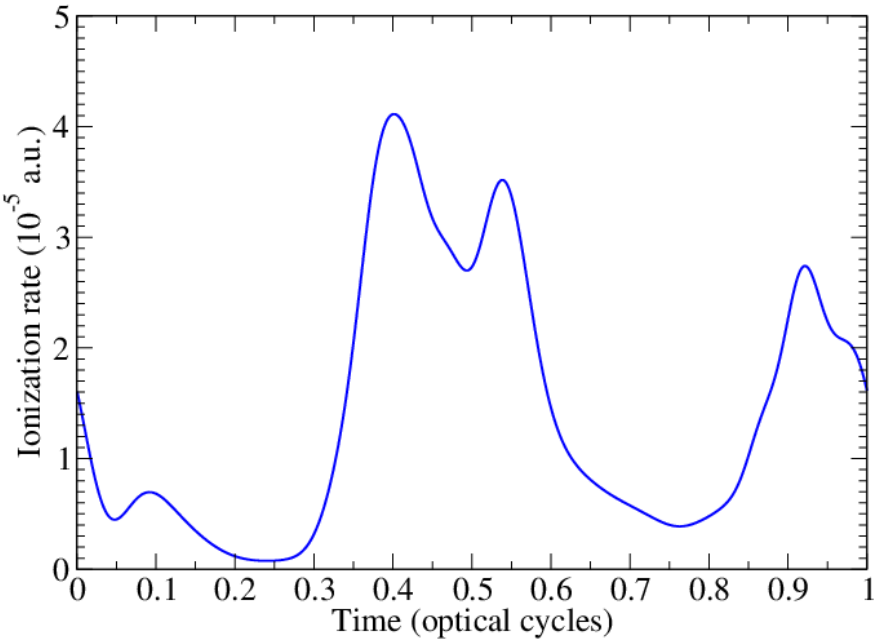

Figure 3.2: Time-dependent ionization rate of HHe^{2+} at the equilibrium internuclear separation of 4 a.u. (Floquet state originating from the unperturbed 2σ state) calculated as a logarithmic derivative of the population within the sphere with the radius 40 a.u. The wavelength of the laser field is 780 nm and the intensity is 5×10^{13} W/cm^2.

3.2.3 Sub-cycle structures in time-dependent ionization rate of Hydrogen atom

In Fig. 3.3, we show the time-dependent MPI rates for the hydrogen atom initially in the ground state. The laser field has a carrier wavelength 800 nm and the peak intensity 5×10^{13} W/cm^2. We use the values $R_b = 60$ a.u. and $R_a = 40$ a.u. The field is switched on during the first 5 optical cycles with the $\sin^2$ ramp until it reaches the peak intensity. Then the intensity is kept constant for the next 15 optical cycles. Thus the total time for the propagation of the wave function is 20 optical cycles. We should note that the resulting wave function at the end of the propagation time differs very little from the Floquet state in the monochromatic field with the same wavelength and intensity. We perform the MPI rate analysis on the last optical cycle, approximately between the time moments 50.7 fs and 53.4 fs. For better understanding of the electron dynamics during this period of time, in Fig. 3.3a we show the force experienced by the electron from the laser field. For the first half-cycle, the force is negative pushing the electron to the negative side of the z axis; for

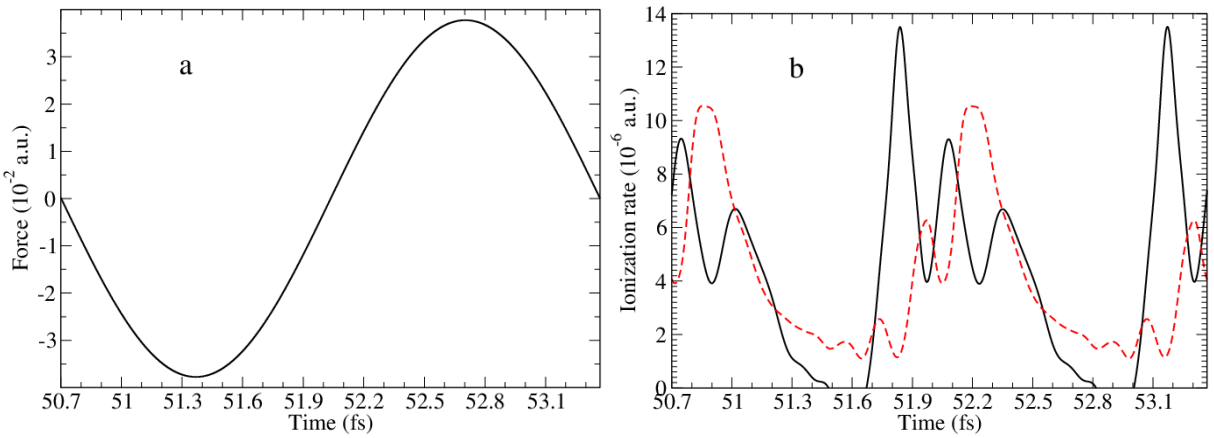

Figure 3.3: (a) Force acting on the electron from the laser field with the wavelength 800 nm and intensity 5×10^{13} W/cm^2. Shown is the time interval between 50.7 fs and 53.4 fs corresponding to one optical cycle. (b) Time-dependent ionization rate of the hydrogen atom calculated as a logarithmic derivative of the population within the sphere with the radius 20 a.u. (full black curve) and 40 a.u. (dashed red curve). The wavelength of the laser field is 800 nm, the peak intensity is 5×10^{13} W/cm^2.

the second half-cycle, the picture is reversed. The MPI rate is defined by Eqs. (3.4) and (3.5) for the whole spherical volume with the radius R_b where the time-dependent Schrödinger equation is solved. However, we can also define the MPI rate on the boundary of a smaller spherical volume with the radius $R_0 < R_b$. Defined in this way, the quantity dP/dt represents the electron current through the sphere of radius R_0, that is the observable which can be measured experimentally if the detector is placed at the distance R_0 from the target. In Fig. 3.3b, the time-dependent MPI rates of the hydrogen atom are shown for two different spherical volumes, with the radius $R_0 = 20$ a.u. and $R_0 = 40$ a.u. As in the case of diatomic molecules, the maxima of the MPI rates exhibit a fine subpeak structure. In Fig. 3.3b, one can see three distinct subpeaks corresponding to each maximum. The shape of the subpeaks depends, however, on the radius R_0 (that is the distance from the nucleus) where the rate is measured. Their position on the time scale is shifted from that of the field peak values and also depends on R_0.

3.3 Exploring MPI subcycle with electron density analysis

To get a better understanding of this phenomenon, it is instructive to study the electron density evolution subject to the influence of both the nucleus and the laser field.

In Fig. 3.4, we show the electron density evolution within the 0.7 fs time interval corresponding to multiple current density bursts on the spherical surface with the radius of 20 a.u. (see Fig. 3.3b). The evolution of the density for the full optical cycle is presented as a motion picture in the supplemental material [sup]. In both Fig. 3.4 and the movie [sup], one can clearly see formation of distinct density portions and their motion in the negative z direction where the force from the laser field is directed for this time interval. At the time 51.68 fs, the force is near the peak value, and the first portion of the density is approaching but not yet crossing the spherical surface at 20 a.u. The ionization rate has its minimum at this time moment. The next time moment, 51.83 fs, corresponds to the maximum of the ionization rate. The first portion of the electron density is crossing the boundary while the second one is clearly seen between the z values -15 a.u. and -10 a.u. At the time 51.97 fs, the first portion has already moved beyond the boundary, the second portion has approached the boundary but not crossed it; the third portion is shaped and clearly seen at $z = -10$ a.u. This is again a minimum in the ionization rate. The force from the laser field is still negative but close to zero. At the next time moment, 52.08 fs, the force is also weak but has already changed the sign, now pointing at the positive z direction. Nevertheless, the second portion of the electron density continues moving in the negative z direction and passes the boundary at 20 a.u. In Fig. 3.3b, this time moment corresponds to the second maximum of the ionization rate. At the time 52.25 fs, the third portion of the electron density has approached but not yet crossed the boundary; the ionization rate has its minimum. Finally, at 52.39 fs, the third portion of the density crosses into the outer domain giving rise to the third maximum in the ionization rate. However, the force from the laser field has already been positive for some time and become quite strong by this moment. That is why the negative velocity of the third portion of the density has become small, and the the third maximum in the ionization rate is quite weak.

As the analysis of the time evolution of the electron density reveals, several distinct density por-

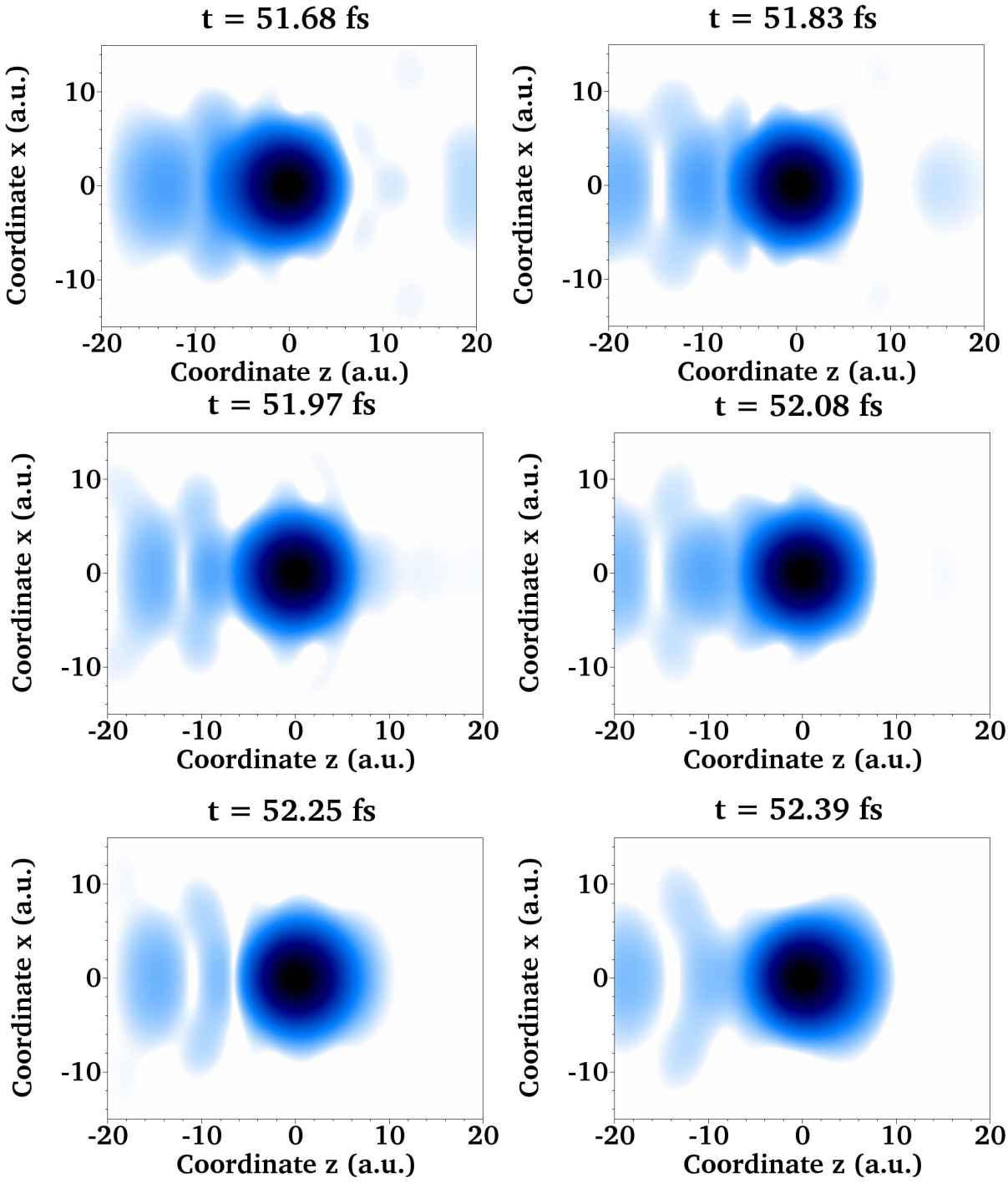

Figure 3.4: Electron density of the hydrogen atom subject to the laser field with the wavelength 800 nm and the peak intensity 5×10^{13} W/cm^2. The color scale for the density is logarithmic.

tions are shaped and detached from the target within half cycle of the laser field. These portions of the electronic wave packet contain contributions with various energies, which move with different velocities when leaving the core. Thus it is not surprising that the shape of the structures changes as the ionized wave packet moves away from the nucleus. Therefore the transient structures in time-dependent multiphoton ionization rates (including the number of subpeaks) depend on the radius R_0 of the sphere where the electron current is measured. Eventually, as R_0 becomes very large, one may expect a re-arrangement in the time-dependent rates according to the energies of the outgoing electrons, with the fast electrons coming first to the detector, and slower electrons coming later. The asymptotic (large R_0) time-dependent rates should correspond to the well-known ATI structures in the energy domain with the peaks separated by the photon energy. However, this large R_0 behavior of the ionization rates is beyond the scope of our study; we focus on the nanometer length scale where the physical picture is quite different.

3.4 Sub-cycle Structures in time-dependent MPI rates for different laser wavelengths and intensities

The sub-cycle transient structures in the time-dependent MPI rates depend also on the wavelength and intensity of the laser field. In Fig. 3.5, we show the MPI rates of H_2^+ and atomic hydrogen at different wavelengths and intensities. The data are obtained from the Floquet state corresponding to the ground electronic states of the target. For the box size and absorber position, we use the values $R_b = 60$ a.u. and $R_a = 40$ a.u., respectively. For H_2^+, the calculations are performed for the equilibrium internuclear separation $R = 2$ a.u., laser wavelength 800 nm and two intensities, 3×10^{14} W/cm^2 and 5×10^{14} W/cm^2. For the hydrogen atom, we fix the intensity at 5×10^{13} W/cm^2 and perform the calculations for two different wavelengths, 780 nm and 1064 nm. As Fig. 3.5 shows, the sub-cycle structures change their form significantly when the wavelength or intensity of the laser field is changed. However, we do not see any simple rule that can describe correspondence between the sub-cycle pattern (including the number of subpeaks) and the laser field parameters.

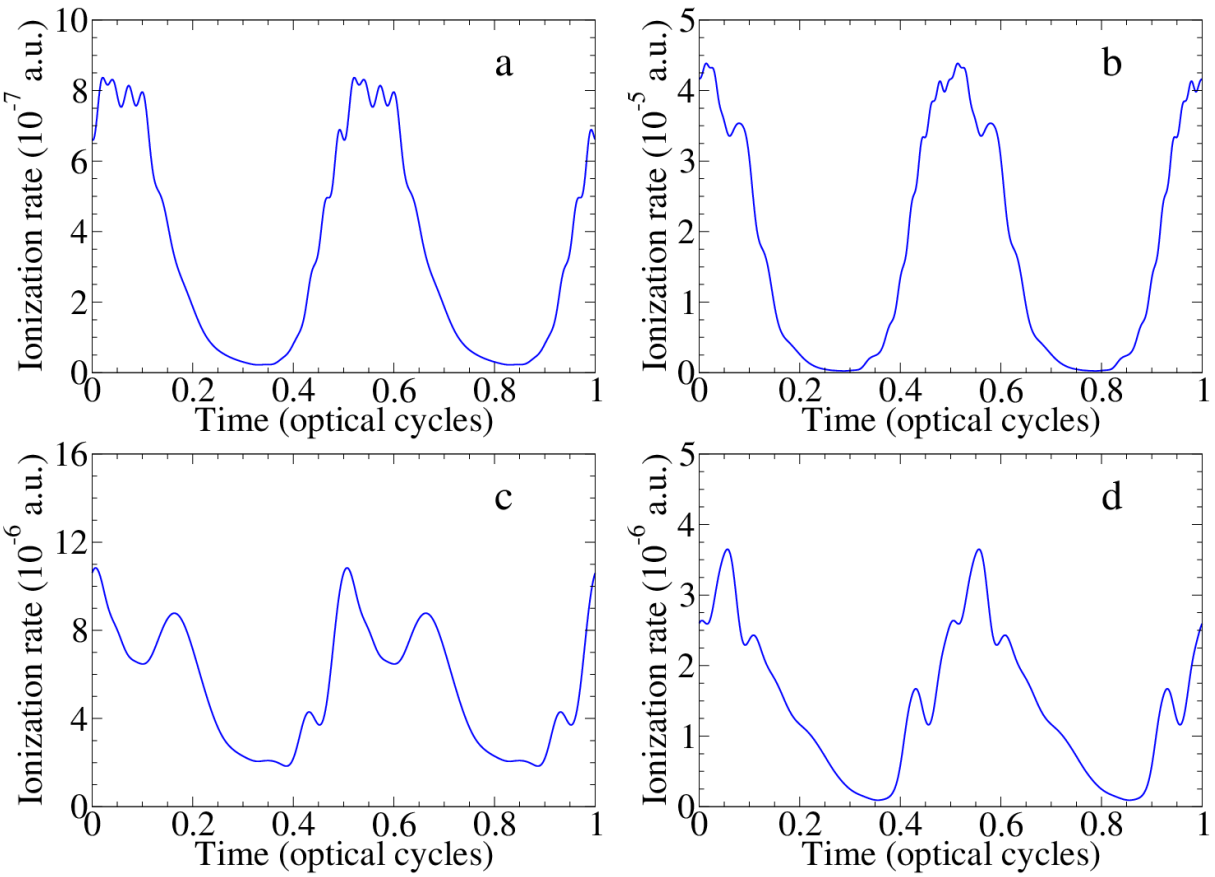

Figure 3.5: Sub-cycle structures in time-dependent MPI rates for different laser wavelengths and intensities (Floquet states). (a) H_2^+ at the internuclear separation of 2 a.u., wavelength 800 nm, and intensity 3×10^{14} W/cm^2. (b) H_2^+ at the internuclear separation of 2 a.u., wavelength 800 nm, and intensity 5×10^{14} W/cm^2. (c) Hydrogen atom at the wavelength 780 nm and intensity 5×10^{13} W/cm^2. (d) Hydrogen atom at the wavelength 1064 nm and intensity 5×10^{13} W/cm^2.

3.5 Conclusion

In summary, we have performed a computational study of multiphoton ionization dynamics on the sub-femtosecond time scale for the hydrogen atom and two one-electron molecular systems, H_2^+ and HHe^{2+}, subject to intense near-infrared laser fields. Our calculations show multiple peaks structure of the time-dependent multiphoton ionization rate within a single optical cycle. The nature of this phenomenon is revealed by the analysis of the time-dependent electron density, which exhibits multiple portions of the density detached from the core at different times, not necessarily when the external field reaches its maximum values. The oscillations of the electron density are caused by transitions to excited bound and continuum states in the laser field. A large dynamic polarizability of the initial state may play a role here. However, at this time we cannot suggest a simple model explaining the phenomenon.

We note that the structures of the multiphoton ionization rates in the *time domain* discussed in this study are not related to the above-threshold peak structures of the electron spectra in the *energy domain*. When created under the influence of the external field, the portions of the outgoing wave packet are localized in space and time but contain various energy contributions. That is why the shape of the structure is changed as the outgoing wave packet moves away from the core. The structures described above can be observed on the nanometer length scale. Certainly, recording the time information close to the target is a very difficult experimental task. Possibly, it can be done by the experimental methods mapping time into momentum such as streak camera, or reconstruction of attosecond beating by two-photon interference (RABBITT). Measurements could be more feasible at sufficiently large distances from the target. Of course, in the far asymptotic region, the time-dependent signal would be reshaped according to the time of flight of the electrons with different energies. In this case, a theoretical reconstruction procedure could help, which maps the properties of the outgoing wave packet at large distances to earlier times and smaller distances. Development of such a procedure can be a subject of a separate study.

Chapter 4

Above- and Below- Threshold High-Order Harmonic Generation of H_2^+ in Intense Elliptically Polarized Laser Fields

4.1 Introduction

Most of the studies so far have been focused on the use of linearly polarized (LP) laser fields, where the semiclassical 3-step model[26, 69] can provide qualitative understanding of the underlying processes. Earlier study of HHG spectrum in EP fields showed that the HHG yield is decreased with increasing ellipticity [9, 77]. There have been also extensive studies of the polarization properties of HHG generated in atomic gases[33, 34, 83]. In this chapter, we perform for the first time a fully *ab initio* 3D and accurate investigation of the effect of ellipticity on the HHG dynamics and spectroscopy of H_2^+ molecules below- and above- the ionization threshold. We show that the generation mechanism of HHG in EP light is considerably different from that in the LP light. Further, in the EP case, particular attention must be paid to follow closely the subtle electron dynamics on the sub-femtosecond time scale and the delicate generation mechanism of HHG below- and above- the ionization threshold. The novel features of HHG in EP light are presented and their quantum

origins are explored in details.

4.2 Solving the TD- Schrödinger equation in elliptical polarized laser field

The simplest diatomic molecule, hydrogen molecular ion H_2^+, has been treated many times previously to study various multiphoton processes in strong laser fields but it still remains an important proto-type system for the investigation of the novel elliptical field effects in HHG of diatomic molecules. In order to get high precision electronic structure results with the use of only a modest number of grid points, we apply the two-center time-dependent generalized pseudospectral (TDGPS) scheme in prolate spheroidal coordinates for accurate and efficient treatment of the time-dependent Schrödinger equation (TDSE) for diatomic molecular systems. The methodology for the HHG calculation starts with solving TDSE in prolate spheroidal coordinates, which are convenient for describing two-center problems as we explained in details in Chapter 2. It should be noted that here we have the elliptical polarzied field interacting with system and we assume that the laser field is in the x–z plane:

$$f(t) = f_0\Big(\frac{\varepsilon}{\sqrt{1+\varepsilon^2}}\widehat{e}_x cos(\omega_0 t) + \frac{1}{\sqrt{1+\varepsilon^2}}\widehat{e}_z sin(\omega_0 t)\Big). \tag{4.1}$$

Here ε the ellipticity parameter and ω_0 the carrier frequency. Then using the dipole approximation and the length gauge, we can write the interaction potential $V_{ext}(\xi,\eta,t)$ in the following form:

$$V_{\rm ext}(\boldsymbol{r},t) = \mathbf{r}.\mathbf{f}(t) = \frac{a f_0(t)}{\sqrt{1+\varepsilon^2}}\Big(\xi\eta\sin(\omega_0 t) + \varepsilon\sqrt{(\xi^2-1)(1-\eta^2)}\cos\varphi\cos(\omega_0 t)\Big), \tag{4.2}$$

In our calculations, we use the sine-squared pulse shape, and the function can be written as follows:

$$f(t) = f_0 \sin^2\left(\frac{\pi t}{NT}\right) \tag{4.3}$$

Here f_0 is the peak field amplitude, $T = 2\pi/\omega_0$ is the duration of one optical cycle, and N is the number of optical cycles in the pulse.

4.3 Calculation of HHG spectra in elliptical polarized laser field

Once the wave function is computed, we can proceed to calculate the spectra of the emitted high-order harmonic radiation. By adjusting the numerical parameters of the present calculations such as the number of grid points, the box size, and absorber position, we reproduce the ground state and low-lying excited states energies of H_2^+ with the machine accuracy. To achieve convergence of the computed HHG spectra for the laser field parameters and internuclear separations used in the calculations (see Sec.4.3.1 below), we set the number of grid points to 160 and 48 for the ξ and η coordinates, respectively, and include the angular momentum projections -24 to 24. For the time propagation, we use 4096 time steps per optical cycle (81920 steps for the whole pulse of 20 optical cycles). To accommodate all important physics in the laser field, the linear dimension of the box is chosen at 60 a.u. In the layer between 40 a.u. and 60 a.u., we place an absorber which prevents spurious reflections of the wave packet from the grid boundary. Our numerical scheme and selection of the parameters secure the accuracy of the results obtained. In the calculations of the HHG spectra, we use the length form (2.42); the acceleration form provides almost identical results, indicating a good quality of our wave functions.

4.3.1 Computational set up for HHG calculation of H_2^+

We have performed the calculations of HHG spectra emitted by H_2^+ in $1\sigma_g$ and $1\sigma_u$ electronic states in an intense EP laser field. In all cases we used a 20 optical cycles laser pulse with the sine-

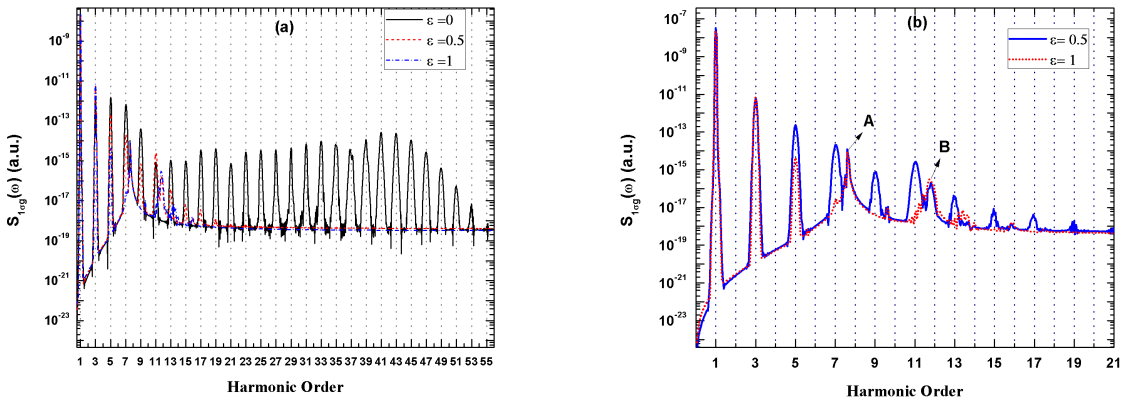

Figure 4.1: panel(a) shows the HHG spectrum $S(\omega)$ from $1\sigma_g$ state of H_2^+ at $R = 2$ a.u. in the laser field with $\lambda = 800$ nm and peak intensity 2×10^{14} W/cm^2 for different ellipticity parameters($\varepsilon = 0, 0.5, 1.0$). Panel(b) demonstrates resonance structures for($\varepsilon = 0.5, 1.0$) near $7th$ and $11th$ harmonics. Arrows mark the resonance peaks in the spectrum in CP field. Resonance A corresponds to excitation of $1\sigma_u$ state, resonance B is due to coupling to $1\pi_u$ state.

squared envelope, the carrier wavelength 800 nm (corresponding to the photon energy 1.55 eV), and the peak intensity 2×10^{14} W/cm^2 . According to the well-known atomic recollision model [26] , the HHG spectra should present a plateau region with a cutoff at the energy $I_P + 3.17U_P$ where I_P is the ionization energy of the initial state and U_P is the ponderomotive potential (for the LP laser field, $U_P = I/4\omega_0^2$, I being the laser intensity). For diatomic molecules, the collision with the parent core resembles the single atom case and leads to the same harmonic spectrum cutoff position independent of the laser field intensity and internuclear separation. However, there is a possibility of collision with the other nucleus. In the latter case, the field intensity and frequency as well as the distance between the nuclei can affect the return kinetic energy of the electron [65]. The vertical ionization potential I_P of H_2^+ is equal to 30 eV for the $1\sigma_g$ state and 18 eV for the $1\sigma_u$ state, at the equilibrium internuclear separation of 2 a.u. Then the cutoff corresponds to the harmonic orders 43 and 36, respectively.

4.3.2 HHG Spectra of H_2^+ in $1\sigma_g$ electronic state($R = 2$ a.u.)

Fig.4.1(a) shows the HHG spectral density of H_2^+ for $1\sigma_g$ electronic state with different ellipticity parameters. As one can see, the semiclassically predicted cutoff positions are in fair agreement with our calculations in the LP filed. Generally, elliptical polarization (and circular polarization to more extent) will reduce the probability of recollision and thus reduce the intensity of above-threshold harmonics (that is harmonics with the photon energies above the ionization threshold). The intensity of below-threshold harmonics (harmonics with the photon energies below the ionization threshold) is also reduced because the dipole transitions are forbidden if the angular momentum projection m is changed more than by unity (and each absorbed circularly polarized photon increases m by 1). All this is true for atoms in laser fields. For molecules, the picture is different: first, due to broken spherical symmetry and m selection rule; second, because the recollision can take place not only on the parent nucleus but also on the other nucleus. Our results demonstrate specific difference between the atoms and molecules. As expected, the HHG cutoff position is shifted to lower frequencies as the ellipticity parameter increases from 0 (linear polarization) to 1 (circular polarization). Interestingly, just a few of the lower harmonics show up in the circularly polarized (CP) filed. Comparing the intensity of the harmonics in different cases($\varepsilon = 0.0, 0.5, 1.0$)presented in Fig.4.1(a), we can see that the intensities of lower-order harmonics are comparable. However, as we go to higher harmonics, their intensities in the EP and CP fields decrease by several orders of magnitude with respect to the linear polarization case. Looking carefully at Fig.4.1(b), one can notice the peaks at the harmonic orders 7.65 and 11.65 , which do not correspond to odd integer numbers. Based on the unperturbed electronic energy values of H_2^+, we attribute the first peak, located near the $7th$ harmonic (harmonic order 7.65), to the resonance with the first excited ($1\sigma_u$) state. Accordingly, the second peak, which appears close to the $11th$ harmonic (harmonic order 11.65), is attributed to the resonance with the second excited ($1\pi_u$) state. We note that the first resonance peak shows up in the HHG spectrum irrespectively of the ellipticity parameter, while the second resonance is absent in the linear polarization case($\varepsilon = 0$). This is well explained by the dipole selection rules: transitions between σ and π states are forbidden when the external field is

directed along the molecular axis.

To explore the detailed spectral and temporal structure of HHG and the underlying mechanisms in different regimes, we perform the time-frequency analysis by means of the wavelet transform [131, 24] of the induced dipole,

$$d_\omega(t_0) = \int_{-\infty}^{\infty} dt \mathbf{D}(t) W_{t_0,\omega}(t), \tag{4.4}$$

with the wavelet kernel$W_{t_0,\omega}(t) = \sqrt{\omega} W(\omega(t-t_0))$ For the harmonic emission, a natural choice of the mother wavelet is given by the Morlet wavelet [24]:

$$W(x) = \left(\frac{1}{\sqrt{\tau}}\right) \exp(ix) \exp\left(-\frac{x^2}{2\tau^2}\right). \tag{4.5}$$

Here the wavelet window function varies with the frequency but the total number of oscillations (proportional to τ) within the window is fixed, however in the Gabor transform [24] the width of the window function is held constant. For the calculations discussed below, we choose $\tau = 15$ to perform the wavelet transform.

In Figs.4.2(a, b), we show the absolute value of the time-frequency spectrum $|d_\omega(t)|$ for the $1\sigma_g$ state of H_2^+ at $R = 2$ a.u. in laser fields with peak intensity 2×10^{14} W/cm^2 and ellipticity parameters ($\varepsilon = 0.0$)and ($\varepsilon = 0.5$). The $1\sigma_u$ resonance is clearly seen at the harmonic order 7.65 in both LP and EP fields, while the $1\pi_u$ resonance shows up at the harmonic order 11.65 in the case of elliptical polarization only.

The cross section of the time-frequency profile corresponding to a specific harmonic order yields a function of time which exhibits a different pattern depending on the harmonic order. For the lowest few harmonics and all ellipticities that we study here, we obtain a smooth function, which resembles the envelope of the driving laser pulse. This is a manifestation of the dominant multiphoton mechanism in lower harmonic regime. In this regime, the probability of absorbing of N photons is about I^N (I is the laser intensity and proportional to $f(t)^2$). In this part of the HHG spectrum, the smooth time profile becomes narrower as the harmonic order is increased.

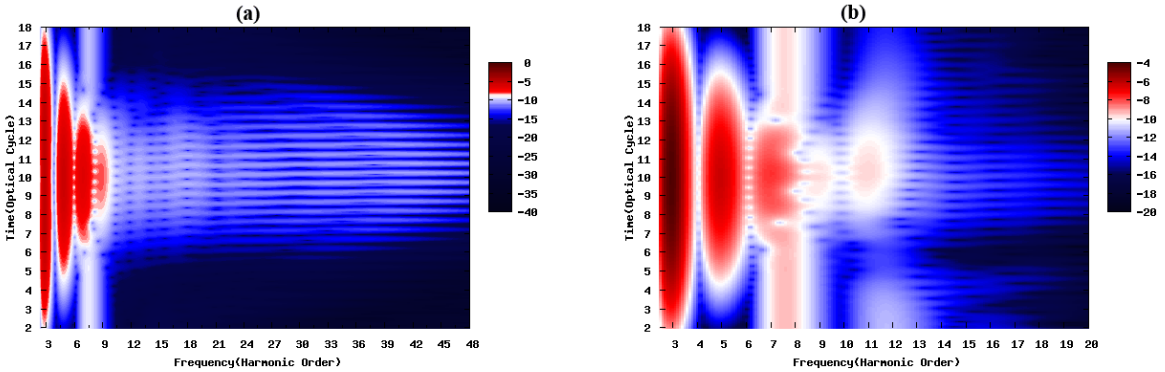

Figure 4.2: Time-frequency spectra for $1\sigma_g$ state of H_2^+ at $R = 2$ a.u. in the laser field with $\lambda = 800$ nm and peak intensity 2×10^{14} W/cm^2 for different ellipticity parameters $\varepsilon = 0.0$in panel(a).and $\varepsilon = 0.5$ in Panel(b)The color scale is logarithmic.

In the frequency domain, the corresponding frequency profile becomes wider (see Fig.4.2). As the harmonic order is further increased in the below-threshold region, the time profiles develop spread fine structures, which resemble the pattern for the above-threshold harmonics and may be attributed to the effect of the quasi-continuum formed by highly excited bound states.

For higher harmonics above the ionization threshold, the time profiles manifest multiple bursts, with two bursts per optical cycle. Each burst is due to the recollision of the electronic wave packet with the ionic core. Transformation of the time-frequency spectra with increasing harmonic order is well illustrated by Fig.4.2.

One can see that the (multiphoton-dominant) low-order harmonics form continuous time profiles at a given frequency. However, for higher harmonic orders, the tunneling-recollision mechanism becomes dominant, and the time-frequency profiles show a netlike structure. This structure is more pronounced for the LP field (Fig.4.2(a)) than in the case of elliptical polarization (Fig.4.2(b)). This is well understood since the recollision becomes increasingly suppressed when the ellipticity parameter increases.

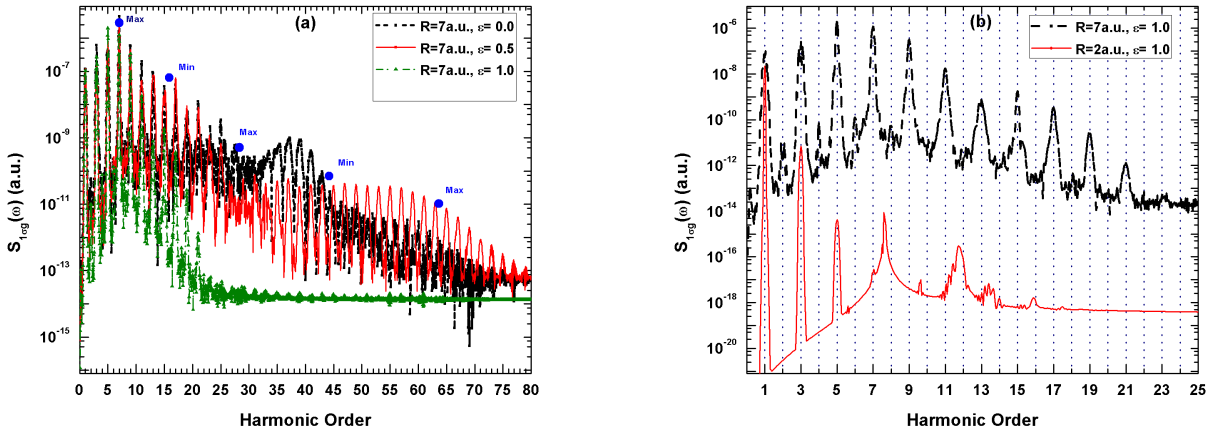

Figure 4.3: HHG spectrum $S(\omega)$ from $1\sigma_g$ state of H_2^+ at $R = 7$ a.u. in the laser field with $\lambda =$ 800 nm and peak intensity 2×10^{14} W/cm^2.(a) HHG spectra for different ellipticity parameters ($\varepsilon = 0.5, 1.0$). (b) Comparison of HHG spectra for the same laser field parameters for CP at $R = 2$ a.u. and $R = 7$ a.u.

4.3.3 HHG Spectra of H_2^+ in $1\sigma_g$ electronic state($R = 7$ a.u.)

We have also performed calculations on stretched H_2^+ molecules with the internuclear separation $R = 7$ a.u. The HHG spectra $S(\omega)$ are shown in Fig.4.3(a-b). The two lowest electronic states,$1\sigma_g$ and $1\sigma_u$, become nearly degenerate at larger (at $R = 7$ a.u., their vertical ionization potentials are 17.6 eV and 17.4 eV, respectively). In the presence of the external fields, the electric dipole coupling of $1\sigma_g$ and $1\sigma_u$ is proportional to R and becomes very significant. This phenomenon, known as the "charge resonance" (CR) effect, takes place only in the odd-charged molecular-ion systems. In LP fields, the combined effect of CR and the multiphoton transitions to excited electronic states is the main mechanism responsible for the enhanced ionization phe-nomenon [22]. Compared with the case $R = 2$ a.u., the ionization probability of H_2^+ is greatly increased due to reduced ionization potential in stretched molecules at $R = 7$ a.u.(the minimum number of photons required for ionization of the $1\sigma_g$ state is equal to 11 compared to 20 at $R = 2$ a.u.). According to the three-step model [65], it leads to enhancement in HHG, resulting in more intense signal and appearance of more distinct harmonics in the high-energy region of the spec-trum (see Fig.4.3(b)).

4.3.4 Interference and mutiple steps in HHG Spectra of H_2^+ at $R = 7$ a.u.

The HHG spectra in Fig.4.3(a) for LP and EP fields exhibit several maxima and minima that can be related to the two-center nature of diatomic molecules [20] (see also discussion in Refs. [122, 123]). Since the returning electron can experience a recollision at any nucleus, the contributions to the recombination amplitude from both nuclei are added coherently, giving rise to the interference structure in the HHG spectra. Using a simple recollision model, one can easily obtain the interference minima or maxima positions in the case of LP fields [72]:

$$cos(\alpha) = \frac{n\pi}{R\sqrt{2E_{ke}}}, n = 1, 2, 3, .. \tag{4.6}$$

where E_{ke} is the kinetic energy of the recolliding electron, α is the angle between the polarization vector of the laser field and the molecular axis, and R is the distance between the two centers (that is, internuclear distance for diatomic molecules).

Assuming all the kinetic energy of the electron is transformed into the harmonic radiation energy during the recollision ($E_{ke} = N_h\omega_0$, where N_h is the harmonic order), for the laser field parallel to the molecular axis ($cos\alpha = 1$), and for the given internuclear separation R and laser frequency, one can obtain the harmonic order N_h where the minimum or maximum should be located. For the $1\sigma_g$ state,$n = 1, 3, 5, ...$ in Eq.4.6 correspond to a minimum, and $n = 2, 4, 6, ...$ correspond to a maximum. Thus a simple calculation can give us an estimate of the harmonic order where the interference maxima or minima are expected in the HHG spectrum. For H_2^+ at the internuclear separation $R = 7$ a.u. subject to the 800 nm LP laser field, only the first few minima and maxima can be relevant for the two-center interference analysis of the HHG spectrum. For $n = 3$ and $n = 5$, the minima can be expected at the harmonic orders 16 and 44, respectively. The maxima for $n = 2, 4, 6.$ can be found around the harmonic orders 7, 28 and 63. These positions are marked in Fig.4.3(a) with blue circles. Except the maximum at the harmonic order 28, the other predictions are in fair agreement with our calculations. We should note that Eq.4.6 represents a rough model and is derived in the case of linear polarization; for EP fields, the estimates based on

this equation become even less accurate.

4.3.5 Even Harmonics in HHG Spectra of H_2^+ at $R = 7$ a.u.

At the internuclear separation $R = 7$ a.u., a comb of well-resolved odd- and even-order harmonics, particularly in the lower energy part of the HHG spectra, is observed. The odd harmonics are at least four orders of magnitude stronger than the even harmonics (see Fig.4.3(b) where the spectra at $R = 2$ a.u. and $R = 7$ a.u. are compared in the case of CP field). By varying numerical simulation parameters such as the number of grid points, the box size, and the absorber position, we have confirmed that the results are converged and existence of even harmonics cannot be attributed to numerical inaccuracy. This is surprising since one would not normally expect generation of even harmonics from homonuclear diatomic molecules.

Generally, generation of even harmonics is forbidden by a fundamental symmetry, which combines the inversion symmetry of the media and the half-wave symmetry of the driving field. Thus in atoms, the presence of only odd harmonics are an indication of the spatial inversion symmetry of the electron–atom interaction energy [84, 80]; the same is true for homonuclear diatomic molecules. It is proven that if heteronuclear diatomic molecules in the gas are oriented [40] or if the half-wave symmetry of the driving field is broken [66], then the HHG spectrum consists of both odd and even harmonics. Strictly speaking, if the driving field represents a pulse but not a continuous wave, the half-wave symmetry is broken, and generation of even harmonics is possible. However, this effect is negligible for long enough pulses. Indeed, for the pulse duration of 20 optical cycles, we do not see even harmonics at the internuclear distance $R = 2$ a.u., but those harmonics do appear at $R = 7$ a.u. We explain this phenomenon by the effect of a dynamical rupture of symmetry (DRS) [14, 94]. The idea behind DRS is that the electron, initially symmetrically distributed over the two nuclei, be-comes essentially localized over one of the nuclei, and periodically bounces back and forth from nucleus to nucleus. During the confinement time over one of the two nuclei, the electron experiences a non-symmetric potential, which is the sum of the symmetric atomic potential of the near nucleus plus the tail of the potential of the far nucleus; this DRS causes

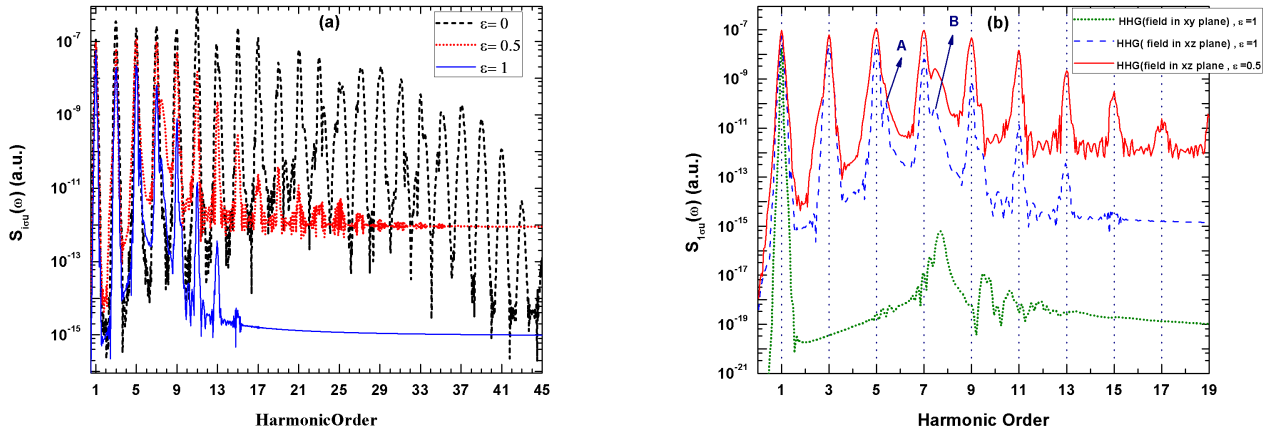

Figure 4.4: HHG spectrum $S(\omega)$ from $1\sigma_u$ state of H_2^+ at $R = 2$ a.u. in the laser field with $\lambda =$ 800 nm and peak intensity 2×10^{14} W/cm^2. (a) HHG spectra for the field polarized in x-z plane and ($\varepsilon = 0.0, 0.5, 1.0$). (b) HHG spectra for with resonance structures near the 5th and 7th harmonics. The arrows mark the resonance peaks in the spectrum. Resonance A corresponds to excitation of $2\sigma_g$ state, resonance B is due to coupling to $1\sigma_g$, $3\sigma_g$, and $1\pi_g$ states. Also shown is the HHG spectrum for the CP field in x-y plane.

the emission of even harmonics [14, 94]. For H_2^+ at the internuclear separation $R = 7$ a.u., the DRS effect is enhanced by existence of the CR states. In the laser field with the intensity as high as 2×10^{14} W/cm^2, a significant amount of the electron population is transferred from the initial $1\sigma_g$ state to the $1\sigma_u$ state, resulting in a non-symmetric electron density distribution. We will discuss this phenomena in details in Chapter.4.

4.3.6 HHG spectra of H_2^+ in $1\sigma_u$ electronic state($R = 2$ a.u.)

We have also performed the calculations of the HHG spectra emitted by H_2^+ in the $1\sigma_u$ (first excited) electronic state. The parameters $\varepsilon = 0.0, 0.5, 1.0$ of the laser pulse are the same as in the previous calculations at $R = 2$ a.u. Fig.4.4(a) displays the HHG spectra of H_2^+ for the $1\sigma_u$ electronic state with different ellipticity parameters . We can see that the HHG cutoffs are shifted to lower energies as the ellipticity parameter increases from linear to circular polarization, in agreement with general predictions for EP laser fields. It appears that the HHG signal for the initial

$1\sigma_u$ state is several orders of magnitude stronger than that for the $1\sigma_g$ state, with the same laser pulse parameters, as one can see from Fig.4.4(a,b). This is well explained by much lower ionization potential (and, hence, much higher ionization probability) of the $1\sigma_u$ state at the internuclear separation $R = 2$ a.u. Analysis of below-threshold harmonics (the minimum number of photons required for ionization is 12 while the cutoff is around harmonic order 36) in the cases $\varepsilon = 0.5$ and $\varepsilon = 1.0$ (Fig.4.4(b)) reveals resonance peaks in the vicinity of the 5th and 7th harmonics. The unperturbed bound state energies of H_2^+ suggest that the first peak, which appears near the 5th harmonic, corresponds to the resonance with the $2\sigma_g$ state. As to the second peak, located near the 7th harmonic, it can be attributed to the resonances with the $1\sigma_g$, $3\sigma_g$, and $1\pi_g$ states. These resonances are not resolved into separate peaks since their transition energies are very close to each other. Since the diatomic molecule H_2^+ does not possess the spherical symmetry, the effect of EP laser field depends on the orientation of the molecular axis with respect to the polarization plane of the field. Above we have studied one representative case, when the molecular axis lies in the polarization plane and is directed along the major axis of the polarization ellipse. Now we consider another important case, when the molecular axis is perpendicular to the polarization plane (that is, the field is polarized in the x-y plane):

$$f(t) = f_0\Big(\frac{\varepsilon}{\sqrt{1+\varepsilon^2}}\widehat{e}_x cos(\omega_0 t) + \frac{1}{\sqrt{1+\varepsilon^2}}\widehat{e}_y sin(\omega_0 t)\Big), \tag{4.7}$$

$$\begin{aligned} V_{\text{ext}}(\boldsymbol{r},t) = \mathbf{r}.\mathbf{f}(t) = a f_0 \sin^2\Big(\frac{\pi t}{NT}\Big)\sqrt{(\xi^2-1)(1-\eta^2)} \\ \Big(\frac{\varepsilon}{\sqrt{1+\varepsilon^2}} cos(\varphi) cos(\omega_0 t) + \frac{1}{\sqrt{1+\varepsilon^2}} sin(\varphi) sin(\omega_0 t)\Big), \end{aligned} \tag{4.8}$$

Here we report the results regarding the circular polarization ($\varepsilon = 1.0$) only. For the polarization in the x-y plane, the situation resembles the atomic case since the same selection rules apply to the angular momentum projection onto the axis perpendicular to the polarization plane (that is, the molecular axis). For the unperturbed molecule, the angular momentum projection m on

the molecular (z) axis is conserved. In the CP field in the x-y plane, absorption of each photon changes this projection by $\Delta m = -1$ or $\Delta m = 1$ for the right and left polarization, respectively. Thus absorption of several photons from the field leads to population of the states with large m values; dipole transitions from such states to the ground state with emission of a single photon are forbidden by the selection rules. In Fig.4.4(b), we can see strong suppression of HHG for both below-threshold and above-threshold harmonics. For the polarization in the x-z plane, the situation is different: the HHG is suppressed but not that much as in the x-y polarization case. Moreover, the below-threshold harmonics are quite strong, and this happens because there is no $\Delta m = \pm 1$ selection rule (for each absorbed photon) with respect to the molecular axis.

4.3.7 Time-frequency spectrum analysis of H_2^+ in $1\sigma_u$ electronic state

To illustrate the mechanisms of HHG in the $1\sigma_u$ state of H_2^+, we perform a time-frequency analysis and plot the time-frequency spectrum $|d_\omega(t)|$for the case of circular polarization in the x-z plane (Fig.4.5). One can clearly see the resonances near the 5th and 7th harmonics; the resonance lines remain quite strong even at the end of the pulse, when the external field vanishes. The HHG mechanisms are revealed by the time profiles of the harmonics in different energy regions obtained by performing the cross section of the time-frequency spectrum. For the lowest few harmonics, the time profile (at a given frequency) shows a smooth function corresponding to the envelope of the driving laser pulse. This behavior resembles what we obtain for the state and manifests the dominant multiphoton mechanism in the low energy region. Development of extended fine structures in the time profiles of the higher harmonic order can be attributed to the effect of excited states and the onset of the continuum. In the intermediate energy regime, where both multiphoton and tunneling mechanisms contribute, the time-frequency profiles show a net like structure, as seen in Fig.4.5. Since the HHG spectrum in the circular polarization case is quite short, and there is no clear plateau well above the ionization threshold, the fast burst time profiles corresponding to the tunneling regime are developed by a few harmonic only.

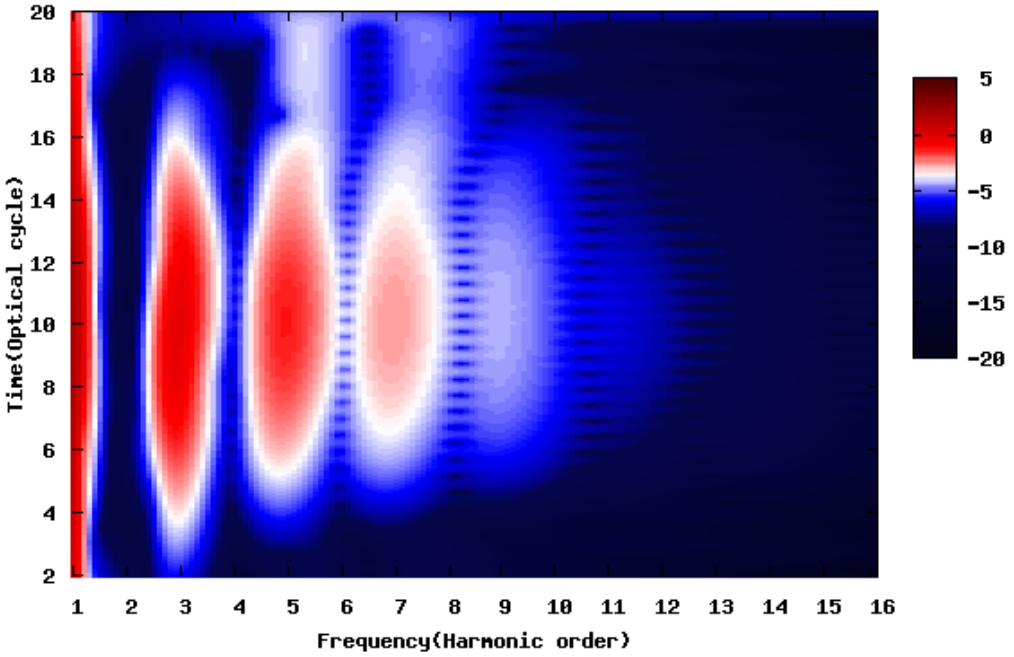

Figure 4.5: Time-frequency spectra for $1\sigma_u$ state of H_2^+ at $R = 2$ a.u. in the laser field with $\lambda = 800$ nm and peak intensity 2×10^{14} W/cm^2.and the ellipticity parameter $\varepsilon = 1.0$. The color scale is logarithmic.

4.4 Conclusion

In conclusion, we have presented *ab* initio high-precision study of high-order harmonic generation of the hydrogen molecular ion in intense laser fields. It is found that the HHG yield is very sensitive to the ellipticity of the driving laser field. The reduction in the production of above-threshold harmonics for non-zero ellipticity, particularly for $\varepsilon = 0.5$ and $\varepsilon = 1.0$ is partially explained by the third step of the recollision model: the transverse component of the laser field tilt the trajectory of the electron and prevent it from recombining with the parent nucleus (it may recombine with the other nucleus, however). If the polarization plane of the laser field contains the molecular axis, the below-threshold harmonics still appear quite strong, even for circular polarization, in contrast with the case when the polarization plane is perpendicular to the molecular axis. This happens because the excited bound states with the angular momentum projections $m = 0$ and $m = 1$ onto the molecular axis (that is, σ and π states) still can be populated by absorption of multiple photons in the CP field, provided the molecular axis has a non-zero projection in the polarization plane. These excited states then allow transitions to the ground state with emission of a single photon.

Such multiphoton excitations followed by transitions to the ground state with emission of a single photon are not permitted for atoms since atomic states possess definite angular momentum, which must increase by one after absorption of each CP photon. Thus the reduced symmetry of diatomic molecules, as compared with atoms, leads to qualitative differences between the atomic and molecular HHG spectra in EP laser fields, with higher HHG yield from molecules. Another feature revealed by the present calculations is also related to the reduced symmetry. Weak even harmonics observed in the HHG spectra of H_2^+ molecules stretched at the internuclear distance $R = 7$ a.u. can be explained by dynamically broken inversion symmetry, when the electron density is periodically localized near one of the two nuclei.

Chapter 5

Generation of Below-threshold Even Harmonics by Stretched H_2^+ Molecular Ion in Intense Linearly and Circularly Polarized Laser Fields

5.1 Introduction

Recently more attention has been paid to generation of the below-threshold harmonics (BTH) as a potential approach to produce novel light sources in the vacuum-ultraviolet (VUV) band due to the higher conversion efficiency [16]. Several theoretical and experimental studies [78, 45, 53], particularly in elliptically polarized field [10], for BTH have been performed. For a certain order of BTH, abnormal ellipticity dependence of the harmonic yield was observed [61]. However, the mechanism of the BTH generation is still not understood very well and remains an open question. Even though the traditional three-step model [26] of high harmonic generation cannot be applied directly to this energy region, one can still use it as a qualitative tool to understand the harmonic generation (HG) process in linearly polarized laser fields [136, 117, 53, 60]. According to the

generalized semiclassical model [136], the atomic (molecular) core potential plays an important role during the excursion of the electron in the laser field and makes it possible for the returning electron to have the total energy less than zero thus leading to emission of below-threshold harmonics. It was found that only the long trajectories in the tunneling ionization regime can contribute to BTH through this mechanism. For elliptical and circular polarization of the driving field, the recollision is not intuitive. The transverse component of the laser field tilts the trajectory of the electron and prevents it from recombining with the parent nucleus. However, in two-center systems such as diatomic molecules, recombination can still occur on the other nucleus [65]. Another contribution to generation of BTH comes from the multiphoton mechanism [136]. The phases of these two contributions have different dependence on the intensity of the driving laser field; their interference results in prominent steps in the intensity-dependent yield of these harmonics [136]. Recent calculations by Xiong *et al.* [135] reveal that, besides the quantum path interference mechanism, resonance effects have a crucial impact on the BTH generation. Thus it appears that several mechanisms beyond the perturbation theory can be involved in the HG process below the ionization threshold, and the HG spectra in this energy region cannot be fully explained using only one mechanism.

In chapter 4, we reported an observation of weak yet well pronounced even harmonics in the below-threshold region of the HG spectra in stretched H_2^+ molecules. To the best of our knowledge, the mechanism of generation of even harmonics in this quantum system has not been fully investigated. Because of the fundamental symmetry, which includes the inversion symmetry of the media and the half-wave symmetry of the driving field, generation of even harmonics is forbidden. In atoms, due to the spatial inversion symmetry of the electron-nucleus interaction, only odd harmonics are present in the HG spectra [81]. Strictly speaking, if the driving field represents a pulse and not a continuous wave, the half-wave symmetry is broken, and generation of even harmonics is possible [66]. However, this effect is negligible for long enough pulses like those containing 20 optical cycles. The same argument is valid for homonuclear diatomic molecules. Only for the gas of *oriented heteronuclear* diatomic molecules one can expect to see both odd and even harmonics

in the HG spectra [40].

The HG spectra of the stretched ($R = 7$ a.u.) homonuclear diatomic molecular ion H_2^+ in circularly polarized laser fields showed a comb of well-resolved odd and even harmonics, particularly in below-threshold region of the spectra. We explained this unexpected pattern in the HG spectra by the effect of a dynamical rupture of symmetry (DRS) [27]. In the unperturbed H_2^+, the electron density is symmetrically distributed over the two nuclei. Under the influence of the external field, the electron density becomes sequentially localized over one of the nuclei, and repeatedly bounces back and forth from one nucleus onto another. During the localization time over one of the nuclei, the electron experiences a non-symmetric potential, which is the sum of the symmetric atomic potential of the near nucleus plus the tail of the potential of the far nucleus; this dynamic breaking of the inversion symmetry causes the emission of even harmonics. In the stretched configuration, the two lowest electronic states of H_2^+, $1\sigma_g$ and $1\sigma_u$, become nearly degenerate as the internuclear separation R increases. The electric dipole coupling of these two states at large R grows linearly with R and becomes very significant. This phenomenon takes place only in the odd-charged molecular-ion systems and it is known as the "charge resonance" (CR) effect [92]. In H_2^+ subject to laser fields, DRS is also enhanced by existence of the CR effect. In the present chapter, we elaborate on the dynamically broken inversion symmetry in stretched H_2^+ molecules using various laser wavelengths and internuclear distances in the calculations. Although the phenomenon is not specific for non-zero ellipticity only, it becomes more pronounced when the ellipticity parameter is large enough, particularly in the case of the circular polarization of the driving field.

5.2 Solving TD- Schrödinger equation in presence of circular polarized laser field

In this chapter we analyze the elliptical field and internuclear separation effects in harmonic generation of diatomic molecules, using the simplest diatomic molecule, hydrogen molecular ion H_2^+. Detailed numerical procedures can be found in chapter2. Adopting proper numerical parameters

such as the number of grid points, the box size, and absorber position, we reproduce the ground state of H_2^+ with the machine accuracy. To obtain the HG spectra for the laser field parameters and internuclear separations used in the calculations, we set the grid size (for the ξ, η, and φ coordinates, respectively) to $180 \times 58 \times 48$ in the circularly polarized (CP) field and to $224 \times 32 \times 16$ in the linearly polarized (LP) field. We use 4096 time steps per optical cycle (81920 steps for the total pulse of 20 optical cycles) in the time propagation process. All spatial and temporal parameters have been varied to make sure all the harmonic spectra are fully converged. Choosing the linear dimension of the box at 60 a.u., we guarantee the accurate description of all the important physics for the laser field parameters used in the calculations. In order to prevent artificial reflections of the wave packet from the grid boundary, we place an absorber in the layer between 40 and 60 a.u.

Once the time-dependent wave function is available, we can proceed to calculate the spectra of the emitted harmonic radiation. The spectral density of the harmonic radiation energy is given by either the length form or acceleration form which provide almost identical results for HG spectra, indicating good quality of our wave functions.

5.3 Even harmonic generation in stretched molecule of H_2^+ at different carrier wavelengths

We have performed the calculations of the HG spectra emitted by a stretched H_2^+ molecule initially in the $1\sigma_g$ electronic state. We used both the LP and CP laser fields with three different carrier wavelengths in the near-infrared range (640, 800, and 1064 nm). In all cases, the laser pulse has a sine-squared envelope and total duration of 20 optical cycles. Since HG is a highly nonlinear process, the key role is played not by the time average of the energy flux (intensity) but by the peak value of the electric field strength. For the same peak value of the electric field F_0, the intensity of the LP field ($I = cF_0^2/(8\pi)$, c being the speed of light) is twice as small as that of the CP field ($I = cF_0^2/(4\pi)$). Thus it makes more sense to compare the HG spectra in the LP and CP laser fields at *different* intensities, with the intensity of the CP field two times larger than that of the

LP field. fig. 5.1 shows the HG spectra of the H_2^+ molecular ion initially in the $1\sigma_g$ state with the internuclear separation $R = 7$ a.u. for both CP and LP fields and all three carrier wavelengths. The peak intensity is 1×10^{14} W/cm^2 for the LP field and 2×10^{14} W/cm^2 for the CP field.

According to the well-known atomic recollision model [26], in the case of the LP field with the intensity I, the cutoff in the HG spectrum is located around the energy $I_P + 3.17U_P$ where U_P is the ponderomotive potential ($U_P = I/4\omega_0^2$) and I_P is the ionization energy of the initial state. For H_2^+ in the $1\sigma_g$ state at $R = 7$ a.u., the vertical ionization energy is 0.648 a.u. At $I = 1 \times 10^{14}$ W/cm^2, the harmonic orders corresponding to the cutoff are equal to 15, 23, and 43 for the wavelengths 640, 800, and 1064 nm, respectively. The below-threshold region in the HG spectrum is defined as that with the photon energies less or equal to I_P. Thus the below-threshold harmonics are those with the orders less or equal to 9, 11, and 15 for the wavelengths 640, 800, and 1064 nm, respectively. Normally one expects to see only odd harmonics in the HG spectra. However, the spectra in fig. 5.1 also exhibit weak even harmonics in the below-threshold region. These even harmonic peaks appear more distinct in the case of CP field and become larger as the carrier wavelength increases. They become less pronounced in the above-threshold region.

5.4 Even harmonic generation in H_2^+ at different internuclear separations

We have further studied generation of even harmonics at different internuclear separations. fig. 5.2 shows the HG spectra of the H_2^+ molecular ion under LP and CP fields with the carrier wavelength 1064 nm at the internuclear separations 3 to 6 a.u., for the initial $1\sigma_g$ state. The peak intensity in this set of calculations is 1×10^{14} W/cm^2 for the LP field and 2×10^{14} W/cm^2 for the CP field. When the internuclear distance R increases, the vertical ionization potential decreases, so does the energy difference between the $1\sigma_g$ and $1\sigma_u$ states. At the smallest $R = 3$ a.u. used in the calculations (figs. 5.2a and 5.2b), there are no visible even harmonics in the spectra; however, one can notice the enhanced 5th harmonic and an extra peak at the harmonic order 5.28. The 3rd, 7th,

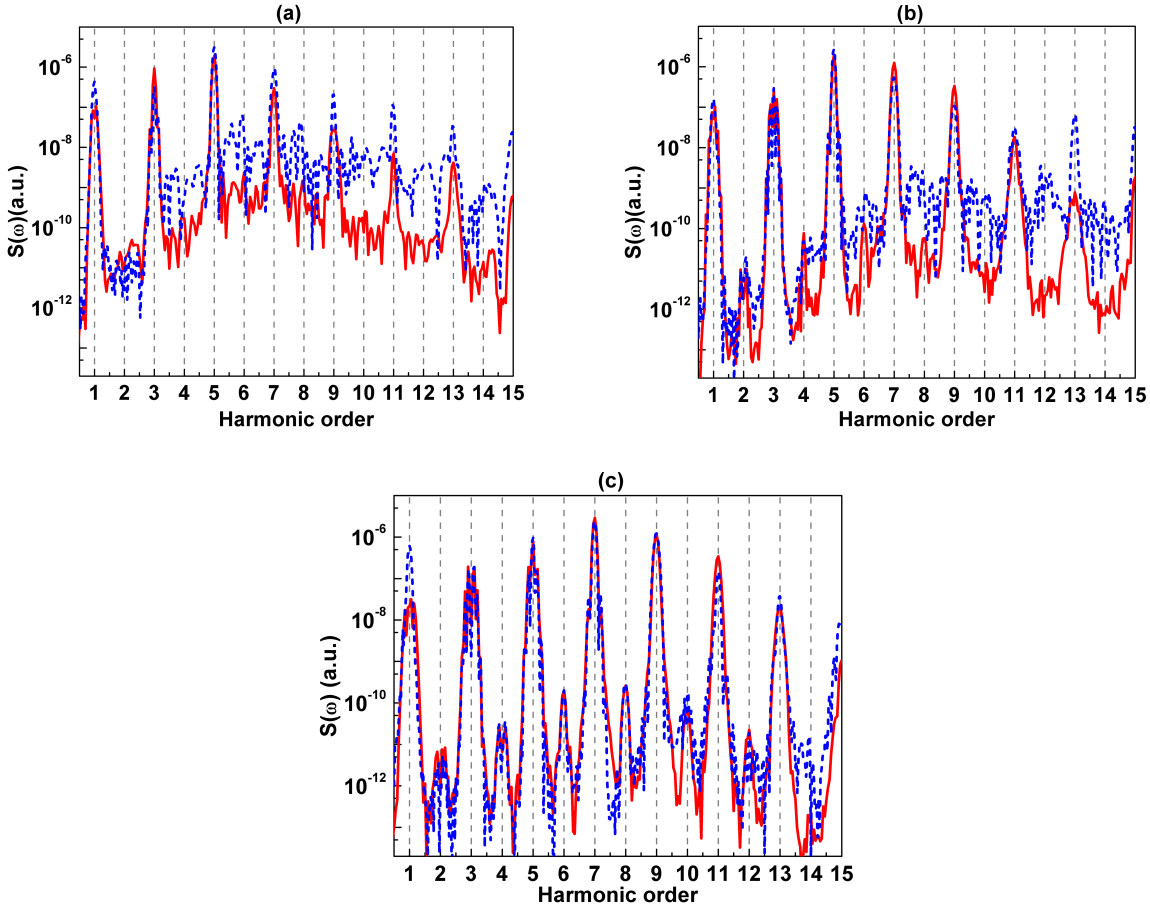

Figure 5.1: HG spectra of H_2^+ molecular ion initially in $1\sigma_g$ state at internuclear separation $R = 7$ a.u. Shown are the results for LP field with the peak intensity of 1×10^{14} W/cm^2 (dashed blue line) and CP field with the peak intensity of 2×10^{14} W/cm^2 (solid red line): panel (a), the carrier wavelength 640 nm; panel (b), the carrier wavelength 800 nm; panel (c), the carrier wavelength 1064 nm.

and 9th harmonics are also split in two peaks each. We attribute this behavior of the HG spectra to the 5-photon resonance between the ground $1\sigma_g$ state and the first excited state $1\sigma_u$ state. For larger R, the HG spectra in the below-threshold region appear more complex. At $R = 5$ a.u. (figs. 5.2e and 5.2f), the even harmonics are as strong as the odd harmonics and have a double-peak structure. At $R = 6$ a.u. (figs. 5.2g and 5.2h), they still exhibit a double-peak structure but become weaker. As we will discuss below, enhanced generation of even harmonics and their double-peak structure are related to strong coupling between the $1\sigma_g$ and $1\sigma_u$ states, particularly in the vicinity of the one-photon resonance at $R = 5$ a.u.

5.4.1 Time-frequency analysis of HG spectra in stretched molecule of H_2^+

To illustrate the dynamics of HG in both LP and CP fields, we have performed the time-frequency analysis of the dipole acceleration according to Eq. (2.45). fig. 5.3 shows an absolute value of the wavelet transform (2.45) for the z-projection of the dipole acceleration. The results are presented for the carrier wavelength 1064 nm and internuclear distances $R = 3$ a.u. and $R = 5$ a.u. The peak intensity of the laser pulse is 1×10^{14} W/cm^2 for LP field and 2×10^{14} W/cm^2 for CP field. As one can see, for the same internuclear separation, the time-frequency spectra for the LP and CP fields are very similar. As expected, the main contribution to the harmonic signal comes from the central part of the laser pulse where the field is the strongest. At $R = 3$ a.u. one can see a strong line close to the harmonic order 5, which does not vanish even at the end of the pulse. This line is due to the 5-photon resonance between the ground $1\sigma_g$ and first excited $1\sigma_u$ states. Before the laser pulse, the $1\sigma_u$ state is not populated. However, because of the resonance, it gains a significant population when the laser field is switched on. This population remains in the $1\sigma_u$ state until the end of the pulse giving rise to emission of radiation. While only odd harmonic lines are present in the time-frequency spectra at $R = 3$ a.u., both odd and even lines show up at $R = 5$ a.u. Moreover, the even 4th and 6th harmonics appear the most intense among all below-threshold harmonics.

Generation of even harmonics indicates that the half-wave symmetry may be broken in this

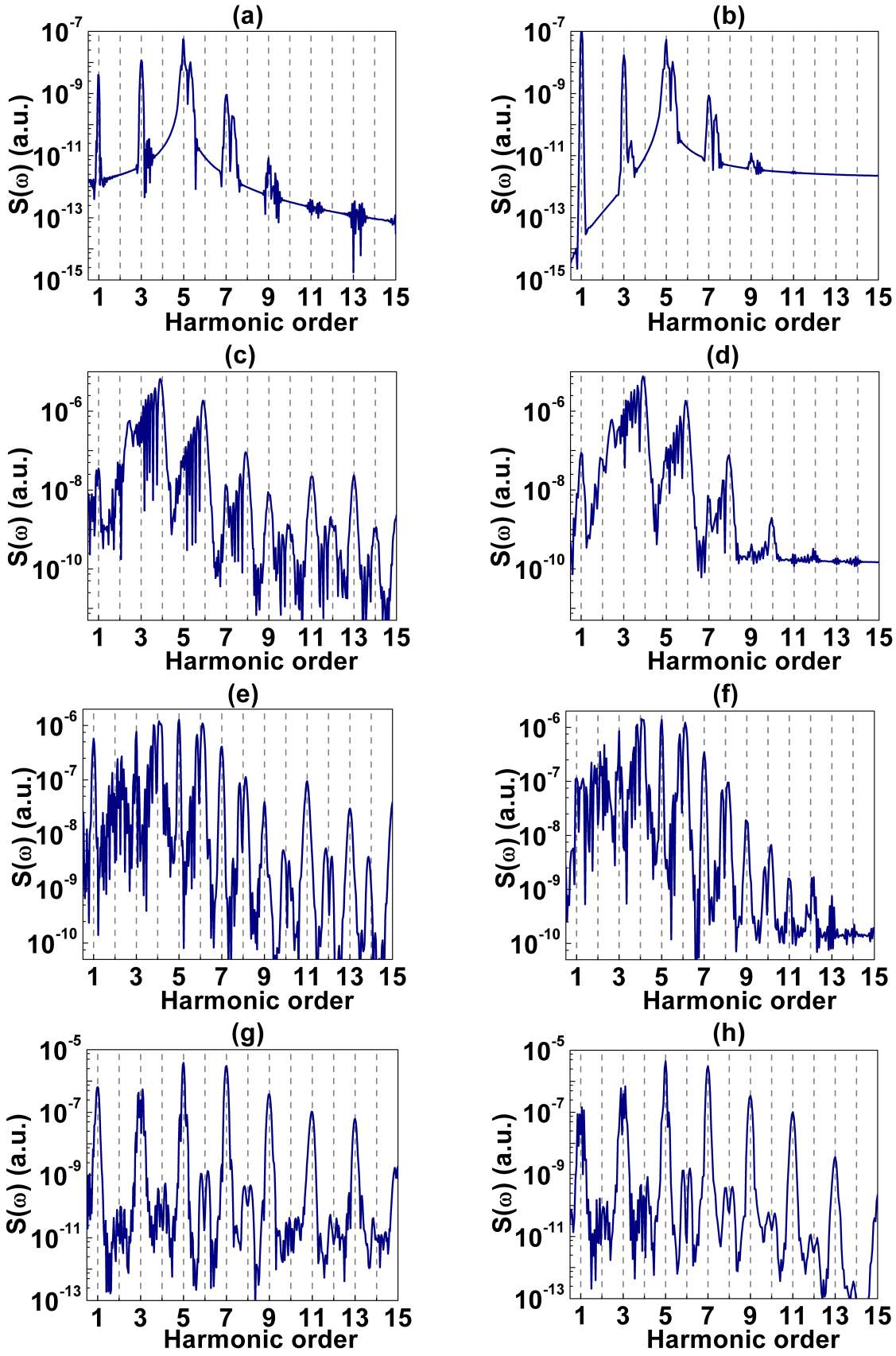

Figure 5.2: HG spectra of H_2^+ molecular ion initially in $1\sigma_g$ state at different internuclear separations: $R = 3$ a.u. [panels (a) and (b)], $R = 4$ a.u. [panels (c) and (d)], $R = 5$ a.u. [panels (e) and (f)], and $R = 6$ a.u. [panels (g) and (h)]. Left panels represent LP field with the peak intensity 1×10^{14} W/cm^2, right panels – CP field with the peak intensity 2×10^{14} W/cm^2. The carrier wavelength is 1064 nm.

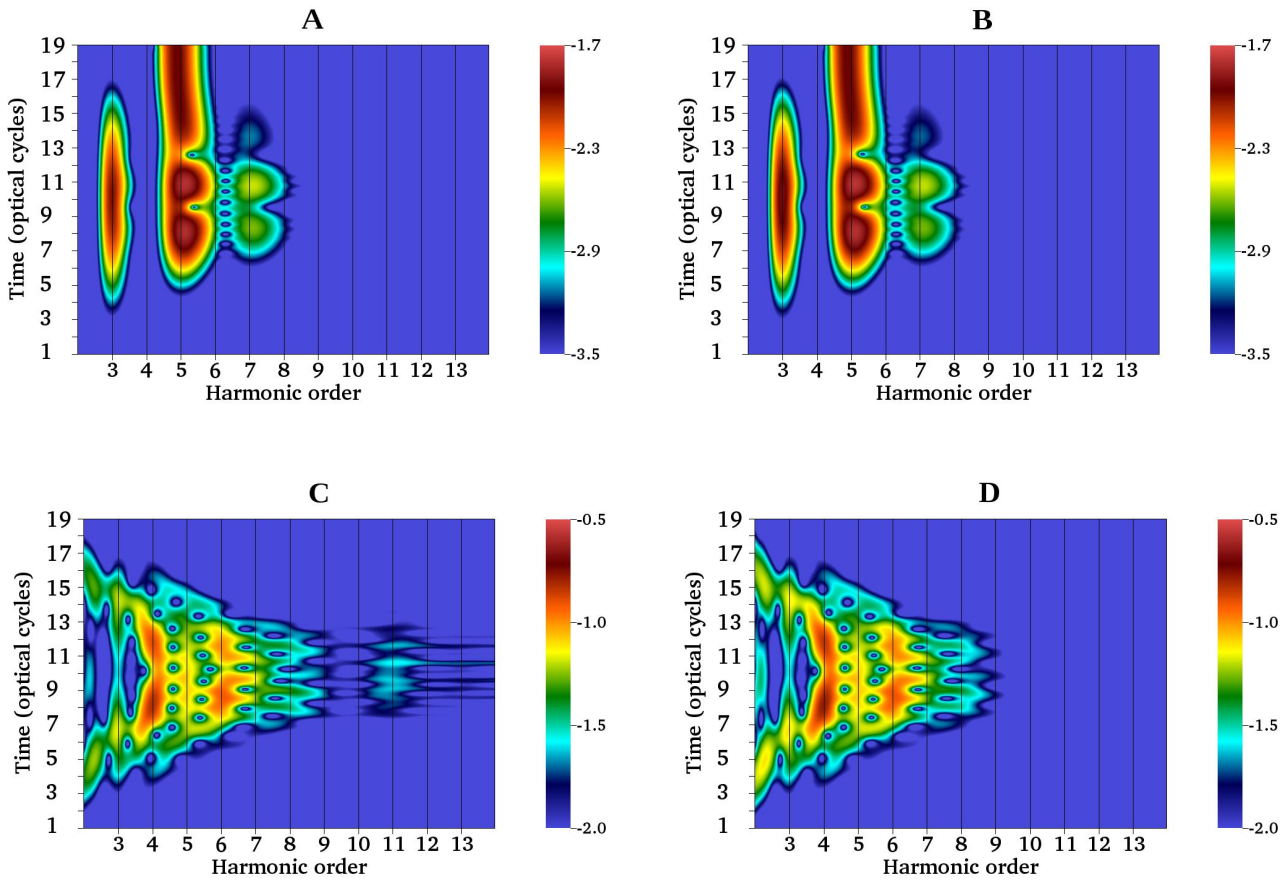

Figure 5.3: Wavelet time-frequency spectra (absolute value) of the dipole acceleration along the molecular axis (z direction) in stretched H_2^+ molecules subject to laser pulses with the carrier wavelength 1064 nm. Panel A: LP field at $I = 1 \times 10^{14}$ W/cm^2 and $R = 3$ a.u. Panel B: CP field at $I = 2 \times 10^{14}$ W/cm^2 and $R = 3$ a.u. Panel C: LP field at $I = 1 \times 10^{14}$ W/cm^2 and $R = 5$ a.u. Panel D: CP field at $I = 2 \times 10^{14}$ W/cm^2 and $R = 5$ a.u. The color scale is logarithmic.

process. The half-wave symmetry of the time-periodic external field is expressed by the equation

$$V_{\text{ext}}(-\boldsymbol{r}, t + T/2) = V_{\text{ext}}(\boldsymbol{r}, t) \tag{5.1}$$

where T is the period. It results in a similar relation for the electron density of the quantum system in the field,

$$\rho(-\boldsymbol{r}, t + T/2) = \rho(\boldsymbol{r}, t), \tag{5.2}$$

provided the initial field-free state possesses the inversion symmetry. Strictly speaking, Eq. (5.1) holds only for the continuous-wave field and is not valid for the pulse with the time-dependent envelope. However, for a long enough laser pulse such as that containing 20 optical cycles, Eq. (5.2) is generally satisfied with a high accuracy, and even harmonics do not show up in the HG spectra. An exception is made by the case when the initial state does not possess the inversion symmetry or *may lose the symmetry* under the influence of the external field when the latter is switched on.

5.4.2 Evidence on half-wave symmetry broken phenomena

To illustrate the possible half-wave symmetry breaking in the laser field, we have calculated the time-dependent probability to find the electron in the left half-space ($z < 0$) and right half-space ($z > 0$). The plane $z = 0$ is the symmetry plane for H_2^+ since the nuclei are located on the z-axis at the points $z = -R/2$ and $z = R/2$. figure 5.4 shows the results for both LP and CP fields in the two cases where the HG spectra differ qualitatively, $R = 3$ a.u. and $R = 5$ a.u. As one can see, at $R = 3$ a.u. the probabilities to find the electron in the left half-space and the right half-space (that is, in the vicinity of the first nucleus and the second nucleus) correspond to the half-wave symmetry equation (5.2): the electron density oscillates between the two nuclei in phase with the laser field. The picture is totally different at $R = 5$ a.u. Here the half-wave symmetry is broken in the central part of the laser pulse where the field reaches its peak intensity. During this period of time (optical cycles 9 to 11), the electron predominantly resides in the vicinity of only one nucleus.

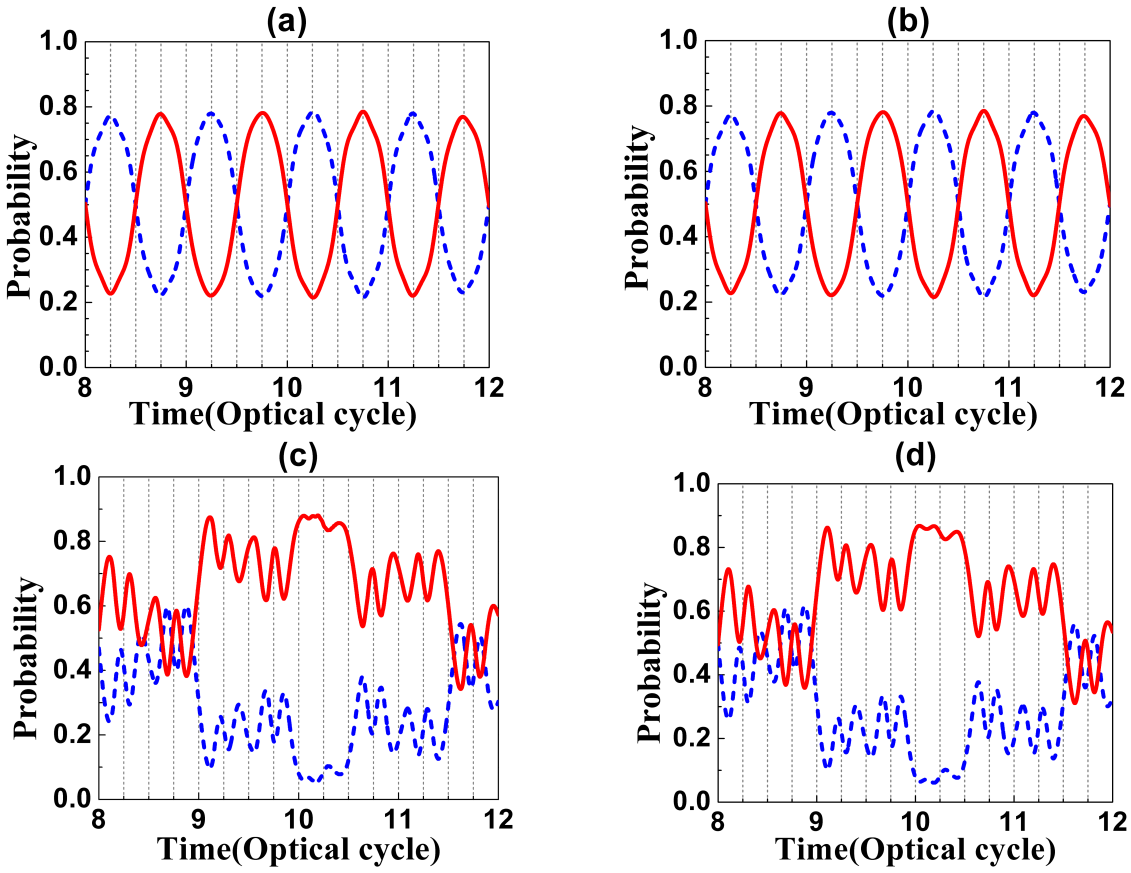

Figure 5.4: Probability to find the electron in the left half-space ($z < 0$) (dashed blue line) and right half-space ($z > 0$) (solid red line) as a function of time in the central part of the laser pulse (8 to 12 optical cycles). Shown are the cases of LP field at $I = 1 \times 10^{14}$ W/cm^2 [panels (a) and (c)] and CP field at $I = 2 \times 10^{14}$ W/cm^2 [panels (b) and (d)]. The internuclear separation R is equal to 3 a.u. [panels (a) and (b)] and 5 a.u. [panels (c) and (d)].

5.4.3 Analysis of HG in quantum systems based on Floquet formalism

The observed features of the HG spectra can be explained with the help of the following approximate theoretical description, based on the analysis of HG in quantum systems described within the Floquet formalism [6, 4, 86]. In the central part of the laser pulse, where the pulse envelope is close to its maximum, the laser field can be approximated as a monochromatic field with the intensity equal to the peak intensity of the pulse. Then the wave function of the electron can be represented as a Floquet wave function. However, strong coupling between the $1\sigma_g$ and $1\sigma_u$ states due to the CR effect and possible tuning into a resonance at the particular carrier frequency and internuclear separation make the picture more complicated. Namely, the electron wave function is represented by a linear combination of *two* Floquet states, originating from the unperturbed $1\sigma_g$ and $1\sigma_u$ states, respectively, and having opposite parities with respect to the half-wave inversion (inversion of the coordinates and shift in time by a half optical cycle):

$$\Psi(\boldsymbol{r},t) = a_1 \exp(-i\varepsilon_1 t) \sum_n \psi_{1,n}(\boldsymbol{r}) \exp(-in\omega t) + a_2 \exp(-i\varepsilon_2 t) \sum_n \psi_{2,n}(\boldsymbol{r}) \exp(-in\omega t). \quad (5.3)$$

Here ε_1, $\psi_{1,n}(\boldsymbol{r})$ and ε_2, $\psi_{2,n}(\boldsymbol{r})$ are the quasienergies and Fourier components of the Floquet states 1 and 2, respectively. The weights a_1 and a_2 of these two Floquet states in the linear combination can be comparable to each other, particularly under the resonance conditions.

The time-dependent dipole moment is calculated as an expectation value of the electron radius-vector $\boldsymbol{r}$:

$$\boldsymbol{D}(t) = \int d^3r \, \boldsymbol{r} \rho(\boldsymbol{r},t) \quad (5.4)$$

and can be expanded in a sum of three contributions:

$$\boldsymbol{D}(t) = \boldsymbol{D}_{11}(t) + \boldsymbol{D}_{22}(t) + \boldsymbol{D}_{12}(t), \quad (5.5)$$

which result from the corresponding expansion of the electron density:

$$\rho(\boldsymbol{r},t) = \rho_{11}(\boldsymbol{r},t) + \rho_{22}(\boldsymbol{r},t) + \rho_{12}(\boldsymbol{r},t), \tag{5.6}$$

$$\begin{aligned}
\rho_{11}(\boldsymbol{r},t) &= \sum_{n,n`} \psi_{1,n}(\boldsymbol{r})\psi^*_{1,n'}(\boldsymbol{r})\exp[i(n'-n)\omega t], && (5.7)\\
\rho_{22}(\boldsymbol{r},t) &= \sum_{n,n`} \psi_{2,n}(\boldsymbol{r})\psi^*_{2,n'}(\boldsymbol{r})\exp[i(n'-n)\omega t], && (5.8)\\
\rho_{12}(\boldsymbol{r},t) &= 2\mathrm{Re}\Big\{ \exp[-i(\varepsilon_1-\varepsilon_2)t] \\
&\times \sum_{n,n`} \psi_{1,n}(\boldsymbol{r})\psi^*_{2,n'}(\boldsymbol{r})\exp[i(n'-n)\omega t]\Big\}. && (5.9)
\end{aligned}$$

The Floquet states 1 and 2 evolve from the symmetric ($1\sigma_g$) and antisymmetric ($1\sigma_u$) unperturbed states of H_2^+, respectively, upon adiabatically slow switch on the laser field. That is why their Fourier components satisfy the following symmetry with respect to the inversion of the coordinates:

$$\begin{aligned}
\psi_{1,n}(-\boldsymbol{r}) &= (-1)^n \psi_{1,n}(\boldsymbol{r}), && (5.10)\\
\psi_{2,n}(-\boldsymbol{r}) &= (-1)^{n+1} \psi_{2,n}(\boldsymbol{r}). && (5.11)
\end{aligned}$$

Consequently, both $\rho_{11}(\boldsymbol{r},t)$ and $\rho_{22}(\boldsymbol{r},t)$ possess the half-wave inversion symmetry:

$$\begin{aligned}
\rho_{11}(-\boldsymbol{r},t+\frac{\pi}{\omega}) &= \rho_{11}(\boldsymbol{r},t), && (5.12)\\
\rho_{22}(-\boldsymbol{r},t+\frac{\pi}{\omega}) &= \rho_{22}(\boldsymbol{r},t). && (5.13)
\end{aligned}$$

Then it follows from Eqs. (5.4)–(5.8) that

$$\boldsymbol{D}_{11}(t+\frac{\pi}{\omega}) = -\boldsymbol{D}_{11}(t), \tag{5.14}$$

$$\boldsymbol{D}_{22}(t+\frac{\pi}{\omega}) = -\boldsymbol{D}_{22}(t). \tag{5.15}$$

According to Eqs. (5.7) and (5.8), $\boldsymbol{D}_{11}(t)$ and $\boldsymbol{D}_{22}(t)$ can be expanded in the Fourier series containing integer multiples of the fundamental frequency ω. Equations (5.14) and (5.15) mean that only odd Fourier components are present in these series expansions, hence only odd harmonics may result from $\boldsymbol{D}_{11}(t)$ and $\boldsymbol{D}_{22}(t)$ contributions to the total dipole moment. This is not the case for $\boldsymbol{D}_{12}(t)$. It follows from Eq. (5.9) that the Fourier series for $\boldsymbol{D}_{12}(t)$ contains the frequencies $n\omega \pm \Delta\varepsilon$ where n is integer and $\Delta\varepsilon = \varepsilon_1 - \varepsilon_2$:

$$\boldsymbol{D}_{12}(t) = \sum_n \Big\{ \exp[i(n\omega - \Delta\varepsilon)t] \sum_{n'} \boldsymbol{d}_{n',n'+n} + \exp[i(n\omega + \Delta\varepsilon)t] \sum_{n'} \boldsymbol{d}^*_{n',n'-n} \Big\}. \tag{5.16}$$

In Eq. (5.16), the notation $\boldsymbol{d}_{n,n'}$ is used for the following dipole matrix element:

$$\boldsymbol{d}_{n,n'} = \int d^3r\, \boldsymbol{r}\, \psi_{1,n}(\boldsymbol{r})\, \psi^*_{2,n'}(\boldsymbol{r}). \tag{5.17}$$

From the wave function symmetry properties (5.10) and (5.11) one can obtain that

$$\boldsymbol{d}_{n',n'\pm n} = (-1)^n \boldsymbol{d}_{n',n'\pm n}. \tag{5.18}$$

Then only even n numbers, $n = 2N$, contribute to the Fourier series of $\boldsymbol{D}_{12}(t)$, and Eq. (5.16) is recast in the following form:

$$\boldsymbol{D}_{12}(t) = \sum_N \Big\{ \exp[i(2N\omega - \Delta\varepsilon)t] \sum_{n'} \boldsymbol{d}_{n',n'+2N} + \exp[i(2N\omega + \Delta\varepsilon)t] \sum_{n'} \boldsymbol{d}^*_{n',n'-2N} \Big\}. \tag{5.19}$$

Generally, the radiation emitted due to the $\boldsymbol{D}_{12}(t)$ term is not restricted to integer multiples of the

fundamental frequency ω and depends on the quasienergy difference $\Delta\varepsilon$. This conclusion is in full agreement with the general Floquet analysis of HG [6, 86] and previosuly established selection rules [4]. We also note that the Floquet theory was successfully used in the past to treat atoms and molecules in laser fields. A complex quasienergy approach in combination with complex scaling of the electronic coordinates provides an accurate description of ionization and HG processes in one-color [87, 121] and two-color [126, 36, 38] laser fields. The shape of the laser pulse can be taken into account, too [120, 37]. More references on the Floquet method can be found in the review paper [20].

For the system under consideration, two limiting cases deserve a special attention, however. The first case is when the quasienergies ε_1 and ε_2 are very close to each other, that is the $1\sigma_g$ and $1\sigma_u$ states are almost degenerate. This happens at large internuclear separations. For example, at $R = 7$ a.u. the unperturbed energies of the $1\sigma_g$ and $1\sigma_u$ states are equal to -0.648 and -0.639 a.u., respectively, and their difference is much smaller than the photon energy (the latter is equal to 0.0428 a.u. for the wavelength 1064 nm). In this case, one can neglect $\Delta\varepsilon$ in Eq. (5.19), and the $\boldsymbol{D}_{12}(t)$ contribution to the total dipole moment will produce *even* harmonics in the HG spectra. This is what we see in figs. 5.1 and 5.2 at $R = 6$ a.u. and $R = 7$ a.u. If small $\Delta\varepsilon$ is taken into account, then the even harmonics exhibit a double-peak structure. The system is far from the one-photon resonance, and only the CR effect is responsible for the population of the second Floquet state. As a result, the even harmonics are relatively weak, compared with the odd harmonics. In Ref. [86], a 1D model of H_2^+ was used, and even harmonics in the HG spectra were found when the initial state was prepared as a superposition of the $1\sigma_g$ and $1\sigma_u$ states with the broken inversion symmetry. We note that in our calculations the initial state is always $1\sigma_g$, and the inversion symmetry is *not* broken at the beginning of the laser pulse. The dynamic rupture of the symmetry is caused by the laser field, which is actually not monochromatic, and the half-wave symmetry equation (5.1) does not apply on the leading and trailing edges of the laser pulse.

The second case is when the quasienergy difference $\Delta\varepsilon$ is close to an odd integer multiple of ω, and the system is in the vicinity of a resonance between $1\sigma_g$ and $1\sigma_u$ states. In this case,

the second Floquet state is significantly populated, and the HG spectra exhibit very strong peaks located outside traditional odd integer multiples of the fundamental frequency. It can be a double-peak structure of odd harmonics, as seen in the case of the narrow five-photon resonance at $R =$ 3 a.u. (see figs. 5.2a and 5.2b), or very strong peaks close to even harmonics in the case of a broader one-photon resonance at $R = 5$ a.u. (figs. 5.2e and 5.2f). We note that the quasienergies, and hence the detuning of the resonance, depend on the intensity of the field. That is why the pattern in the HG spectra for the same laser wavelength and internuclear distance of H_2^+ may change with the peak intensity of the laser pulse.

5.5 Conclusion

We have presented a fully *ab-initio* and accurate study of the electron dynamics during the generation of below-threshold harmonics in H_2^+ molecular ions subject to intense near-infrared linearly and circularly polarized laser fields. The process has been analyzed at different laser wavelengths and internuclear separations in stretched H_2^+ molecules. Strong even harmonics are detected in the emitted radiation spectra. We have shown that this phenomenon has its origin in dynamic rupture of symmetry, when the electron is localized around one nucleus only for a substantial period of time exceeding half optical cycle. The symmetry in the distribution of the electron density is broken under the influence of the laser field when the electronic states with opposite inversion symmetry are both significantly populated. We emphasize the dynamic nature of this phenomenon: it takes place in the laser field despite the initial state ($1\sigma_g$) does have a definite parity, because the laser pulse itself does not satisfy the half-wave symmetry. In H_2^+, this situation is favored by the charge resonance effect, where the $1\sigma_g$ and $1\sigma_u$ states are almost degenerate and have a strong dipole coupling at large internuclear separations. At smaller internuclear distances, possible one-photon resonance between these two states can also lead to generation of intense lines in the radiation spectra at the positions different from the normally expected odd integer multiples of the carrier frequency. We have performed a Floquet theoretical analysis based on the two-state approxima-

tion, which confirms the qualitative considerations given above. Possible experimental observation of even below-threshold harmonics can be done on H_2^+ prepared in excited vibrational states where the molecule spends a substantial amount of time in the stretched configuration or may be subject to dissociation under the influence of the laser field. We expect that even (as well as odd) below-threshold harmonic peaks in the HG spectra are not washed out by the molecular vibration since their positions in the spectra do not depend on R at large internuclear separations.

Chapter 6

Exploration of the Origin of Anomalous Dependence for Near-threshold Harmonics in H_2^+ on the Ellipticity of Driving Laser Fields

6.1 Introduction

High-order harmonic generation (HHG) originating from the interaction of strong laser fields with atoms, ions or molecules, is a unique source of coherent radiation. For the harmonics with energies higher than the ionization threshold, the phenomenon has been extensively studied. Using the conventional three-step model [26], different aspects of HHG process have been accessed both qualitatively and quantitatively by the strong-field approximation (SFA) [74]. Non-vanishing ellipticity of the laser field is an additional resource to control the strong-field phenomena that has been used in production of isolated attosecond pulses [112] and attosecond atomic and molecular imaging [115]. Several theories proved that high harmonics with the photon energies higher than the ionization potential are very sensitive to the driving laser ellipticity [29, 10, 88]. Some well-known

results, such as conditions for two-center interference in molecular HHG spectra, are modified in presence of elliptically-polarized fields [28]. Generally, HHG yield of atoms and molecules in presence of elliptically polarized laser fields drops dramatically with increasing the ellipticity since possible recollisions of the electron with the parent ion are not intuitive. The transverse component of the laser field tilts the trajectory of the electron and prevents it from recombining with the parent nucleus. However, in two-center systems such as diatomic molecules, recombination can still occur on the other nucleus [65].

Near-threshold harmonic spectroscopy is an excellent source of information to explore the specific structures such as resonances. Recently more attention has been paid to the investigation of the near- and below-threshold regime [16, 75, 135, 136, 100]. The harmonic generation (HG) process can be varied by either changing the structure of the bound state or tuning the electron dynamics via controlling the laser ellipticity. In fact, the expansion of high-harmonic spectroscopy to the threshold region still desires a comprehensive knowledge of the underlying HG mechanisms in this specific region.

Traditional semiclassical theories that are based on the three-step model and neglect the influence of the atomic (molecular) core potential on the motion of the detached electron cannot be applied to the generation of harmonics with the photon energies less than the ionization potential. However, extensions of such theories are available, taking into account the electron-ion interaction. It was shown [136] that the atomic (molecular) core potential plays an important role during the excursion of the electron in the laser field. Because of the electron-ion interaction, the returning electron may have the total energy less than zero thus giving rise to generation of below-threshold harmonics. Below-threshold harmonics originate from the long electronic trajectories in the tunneling ionization regime [136]. On the other hand, the contribution of the multiphoton mechanism in generation of below-threshold harmonics cannot be ignored either. The phases of these two contributions have different dependence on the intensity of the driving laser field; their interference results in prominent steps in the intensity-dependent yield of these harmonics [136]. In addition to the quantum path interference mechanism, the electronic structure and resonance effects may

also have a crucial impact on the generation of below-threshold harmonics [135]. Thus several mechanisms beyond the perturbation theory can be involved in the HG process below the ionization threshold, and the HG spectra in this energy region cannot be fully explained using only one mechanism.

So far the anomalous ellipticity dependence of near-threshold harmonics has been reported in several atomic and molecular systems [10, 117, 85, 57, 61]. According to the observations, as the ellipticity grows, the intensity of some of the near-threshold harmonics shows an anomalous maximum at a non-zero ellipticity. A few theoretical explanations have been proposed for this phenomenon. In Ref. [10], it was suggested that free-free transitions subsequent to tunnel ionization could be a candidate mechanism. In Ref. [57], implementing the Coulomb corrections to the SFA model, the authors were able to obtain numerical results in agreement with the experimental data. Another approach [61] attributes the anomalous ellipticity dependence to a near-resonant multiwave-mixing process involving an even number of linearly-polarized photons and a single circularly-polarized photon.

In this chapter, we present fully *ab initio* and high-precision calculations of the HG spectra in the hydrogen molecular ion H_2^+, based on accurate solution of the time-dependent Schrödinger equation in three dimensions. We explore the mechanism of the anomalous ellipticity dependence of some near-threshold harmonics and show unambiguously that this phenomenon is related to the near-resonant excitation of the π-type molecular orbitals. We identify these orbitals responsible for the anomalous ellipticity dependence of different near-threshold harmonics.

6.1.1 Numerical method in calculating the radiation energy emitted in an individual harmonic

We start the calculations of harmonic generation in H_2^+ solving the time-dependent Schrödinger equation

$$i\frac{\partial}{\partial t}\Psi(\boldsymbol{r},t) = H(t)\Psi(\boldsymbol{r},t) \tag{6.1}$$

To discretize the wave function in coordinate space and propagate it in time, we apply the time-dependent generalized pseudospectral method (TDGPS) [122, 128]. The short-time propagation is performed by the second-order split-operator formula in the energy representation:

$$\Psi(\boldsymbol{r},t+\Delta t) \approx \exp\left(-i\frac{\Delta t}{2}H_0(\boldsymbol{r})\right) \times \exp\left(-i\Delta t V(\xi,\eta,t+\frac{\Delta t}{2}\right) \times \exp\left(-i\frac{\Delta t}{2}H_0(\boldsymbol{r})\right)\Psi(\boldsymbol{r},t). \tag{6.2}$$

The operator $\exp\left(-\frac{i}{2}\Delta t\, H_0\right)$ is constructed by the spectral expansion:

$$\exp\left(-\frac{i}{2}\Delta t\, H_0\right) = \sum_n \exp\left(-\frac{i}{2}\Delta t\, E_n\right)|\psi_n\rangle\langle\psi_n| \tag{6.3}$$

where ψ_n and E_n are the eigenvectors and eigenvalues, respectively, of the unperturbed Hamiltonian H_0. In practical calculations, the summation in (6.3) includes all eigenvectors with the energies $E_n < E_b$ where the upper limit E_b should be large enough to describe all relevant physical processes. With the control of high-energy contributions to the propagator matrix, we can avoid population of physically irrelevant regions of the energy spectrum and improve numerical stability of the computations. In the present work, we use E_b=10 a.u.; this is a reasonable value for the carrier frequency and intensities of the laser field used in the present calculations. We obtain the ground state of H_2^+ with the machine accuracy, utilizing the proper numerical parameters such as the number of grid points, the box size, and absorber position. To obtain converged HG spectra for the laser field parameters and internuclear separations used in the calculations, we set the grid size (for the ξ, η, and φ coordinates, respectively) to $160\times48\times48$ and use 4096 time steps per optical cycle (81920 steps total for the pulse of 20 optical cycles) in the time propagation process. All spatial and temporal parameters have been varied to make sure all the results are fully converged. Choosing the linear dimension of the box where Eq. (6.1) is solved at 60 a.u., we guarantee accurate description of all important physics for the laser field parameters used in the calculations. In order to prevent artificial reflections of the wave packet from the grid boundary, we place an absorber in the layer between 40 and 60 a.u. Further details of the numerical procedures can be found

in Refs. [122]. Once the time-dependent wave function is obtained, we can calculate the harmonic radiation spectra. Employing the general semiclassical approach, we can substitute the classical quantities with the corresponding quantum expectation values and calculate the emitted radiation spectra. The spectral density of the harmonic radiation energy can be represented in either the acceleration form,

$$S(\omega) = \frac{2}{3\pi c^3}|\boldsymbol{A}_\omega|^2 \tag{6.4}$$

or the length form,

$$S(\omega) = \frac{2\omega^4}{3\pi c^3}|\boldsymbol{D}_\omega|^2. \tag{6.5}$$

Here $\boldsymbol{D}_\omega$ and $\boldsymbol{A}_\omega$ are the Fourier transforms of the time-dependent dipole moment and dipole acceleration, respectively. The length and acceleration forms provide almost identical results for HG spectra, indicating good quality of our wave functions. The radiation energy emitted in an individual harmonic of the order N_h (N_h is an odd integer number) can be defined as an integral of the spectral density $S(\omega)$ over the corresponding frequency range:

$$E(N_h) = \int_{(N_h-0.5)\omega_0}^{(N_h+0.5)\omega_0} d\omega S(\omega). \tag{6.6}$$

6.2 Harmonic radiation versus ellipticity of the field in H_2^+

We have performed calculations of the HG spectra emitted by the H_2^+ molecular ion initially in the ground ($1\sigma_g$) electronic state. Elliptically-polarized laser pulses have a carrier wavelength of 780 nm, sine-squared envelope, and total duration of 20 optical cycles (52 fs). The harmonic yield was calculated for the ellipticity parameter ε within the range 0 to 0.6 ($\varepsilon = 0$ corresponds to the linear polarization along the molecular axis). In Fig. 6.1(a), we show the harmonic yield versus the ellipticity parameter ε for the equilibrium internuclear distance $R = 2$ a.u. The peak intensity

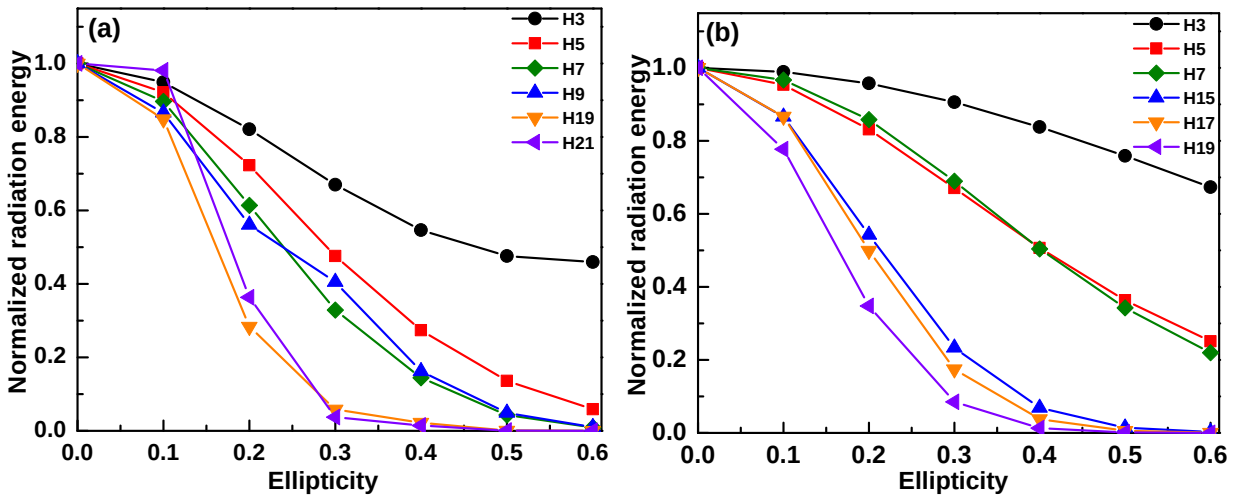

Figure 6.1: Normalized yield of some below-threshold and above-threshold harmonics for H_2^+ molecule initially in the $1\sigma_g$ electronic state: (a) internuclear distance $R = 2$ a.u. and peak intensity 3×10^{14} W/cm^2, (b) internuclear distance $R = 3$ a.u. and peak intensity 2×10^{14} W/cm^2. The sine-squared laser pulse has duration of 20 optical cycles and carrier wavelength of 780 nm.

of the laser pulse is 3×10^{14} W/cm^2. The harmonic signal is normalized to unity at the linear polarization, $\varepsilon = 0$. At $R = 2$ a.u., the vertical ionization potential of H_2^+ is equal to 1.1026 a.u., thus the below-threshold harmonics span the range of orders 3 to 17. As one can see, both below-threshold harmonics of the orders 3 to 9 (H3 to H9) and above-threshold harmonics H19 and H21 exhibit a monotonously decreasing radiation energy with increasing ellipticity, in agreement with the previous observations[29, 10].

A similar pattern is observed at larger internuclear separations, which can be reached in the course of nuclear vibration. In Fig. 6.1b, the results are presented for $R = 3$ a.u. and peak intensity 2×10^{14} W/cm^2 (other laser pulse parameters are the same as in Fig. 6.1a). In this case, the vertical ionization potential of the ground electronic state is equal to 0.9109 a.u., and below-threshold harmonics are those with the orders 3 to 15. As one can see, both the harmonics well below the threshold (H3 to H7) and those in the vicinity of the threshold and above (H15 to H19) exhibit monotonously decreasing radiation energy with increasing ellipticity. This decrease is more rapid for the above-threshold harmonics, and the distribution becomes narrower for higher harmonic orders.

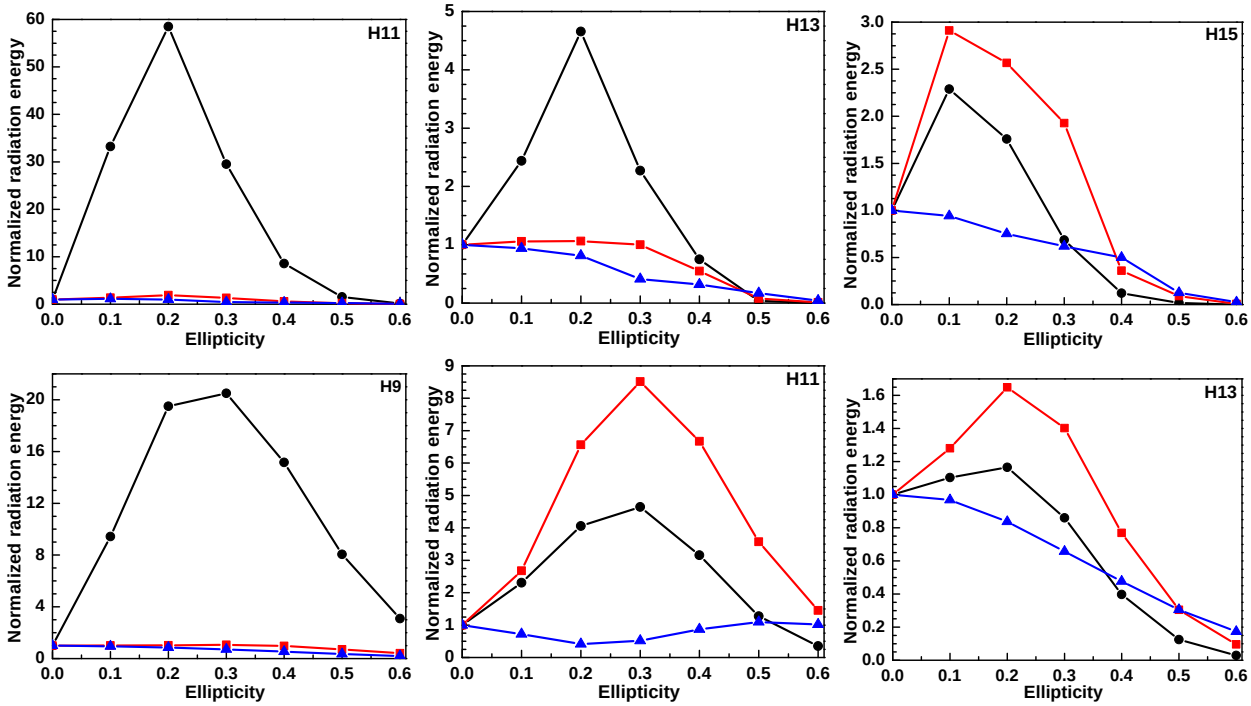

Figure 6.2: Normalized yield of near-threshold harmonics with anomalous ellipticity dependence for H_2^+ molecule initially in the $1\sigma_g$ electronic state. Upper panel: internuclear distance $R = 2$ a.u. and peak intensity 3×10^{14} W/cm^2. Lower panel: internuclear distance $R = 3$ a.u. and peak intensity 2×10^{14} W/cm^2. Black line with circles – full propagator used to obtain the wave function, red line with squares – $1\pi_u$ state removed from the propagator, blue line with triangles – $1\pi_u$ and $2\pi_u$ states removed from the propagator (see text for details). The sine-squared laser pulse has duration of 20 optical cycles and carrier wavelength of 780 nm.

6.3 Anomalous behavior of near-threshold harmonics in H_2^+

The ellipticity dependence is quite different for the below- and near-threshold harmonics (H11–H17 for $R = 2$ a.u. and H9–H13 for $R = 3$ a.u.). As one can see in Fig. 6.2, it becomes non-monotonous, and first the radiation energy grows when the ellipticity parameter is increased starting at $\varepsilon = 0$. The maximum radiation energy is reached somewhere between $\varepsilon = 0.2$ and $\varepsilon = 0.3$, depending on the internuclear distance and harmonic order. Then the harmonic signal starts decreasing if the ellipticity is further increased. The radiation energy at the maximum can be 1-2 orders of magnitude higher than at $\varepsilon = 0$.

The anomalous ellipticity dependence of below-threshold harmonics was observed experimentally in atoms (Ne, Ar, Kr) [10, 85, 61] and diatomic molecules (O_2) [117]. It was suggested

[85, 61] that the effect is due to multiwave-mixing of an even number of linearly-polarized photons with a single circularly-polarized photon. When even number of linearly-polarized photons is in resonance with the excited states of atoms, the sum and/or difference multiwave-mixing can efficiently produce a single circularly-polarized harmonic of a specific order. The role of resonances was also emphasized in the molecular case [117]. Unlike atoms, diatomic molecules do not possess spherical symmetry, and excited electronic states with different projections of the angular momentum onto the molecular axis have different energies. Because of the dipole selection rules, absorption of an even number of linearly-polarized photons by a homonuclear diatomic molecule aligned parallel to the laser field and initially in a σ_g state could result in a resonant excitation of another σ_g state only. Then the harmonic radiation is produced after absorption or emission of an additional circularly-polarized photon, to satisfy the dipole selection rules in the single-photon emission process. If this scheme, suggested previosuly for atoms [85, 61], is also valid for homonuclear diatomic molecules, the resonantly excited σ_g states would play a crucial role in the anomalous ellipticity dependence of the below-threshold harmonics. However, we will show that it is not the case, at least in our study of the H_2^+ molecule, and the major role is played by the excited states of π symmetry.

6.4 Induced dipole contributions to the HG signal

In Figs. 6.3a and 6.3b, we plot the contributions to the HG signal from the projections of the induced dipole acceleration onto the z- and x-axis, for the internuclear distances $R = 2$ a.u. and $R = 3$ a.u. Shown are the HG spectra for the ellipticity parameters $\varepsilon = 0.2$ and $\varepsilon = 0.3$, respectively, where the radiation energy of the near-threshold harmonics reaches its maximum. As one can see in Fig. 6.3a, the HG signal of all the harmonics, except H11–H17, is dominated by the z-projection of the dipole acceleration (parallel to the molecular axis). Consequently, the harmonic radiation is linearly polarized in the z-direction, that is along the major axis of the polarization ellipse of the driving laser field. Harmonics H11 to H17 have the dominant contribution from the

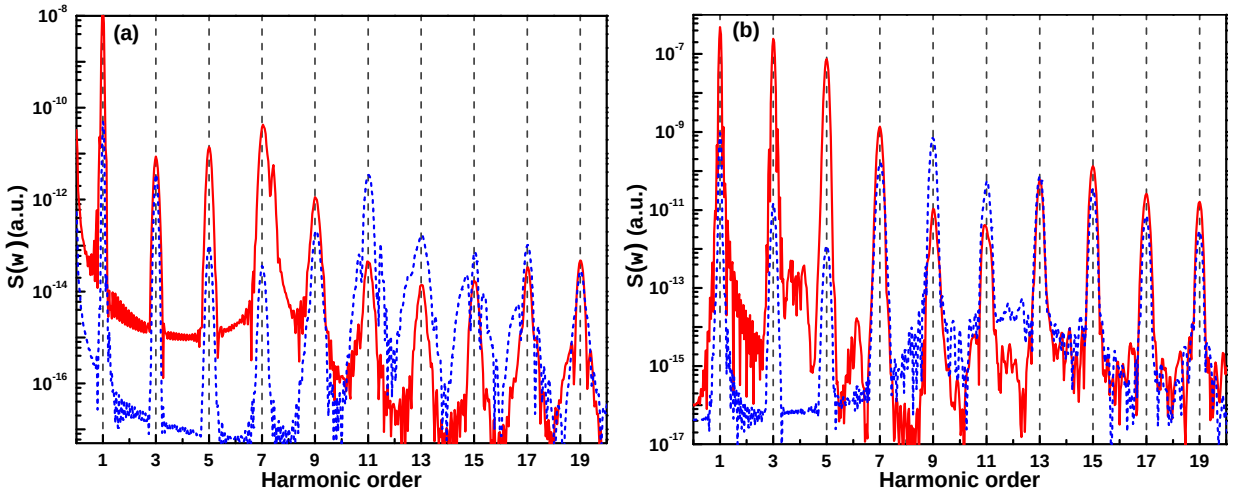

Figure 6.3: Contributions from different polarizations to harmonic spectrum of H_2^+ molecule initially in $1\sigma_g$ electronic state: solid red line, polarization along the major axis of the ellipse; dashed blue line, polarization along the minor axis of the ellipse (see text for details). Upper panel (a): $R = 2$ a.u., $\varepsilon = 0.2$. Lower panel (b): $R = 3$ a.u., $\varepsilon = 0.3$. The sine-squared laser pulse has duration of 20 optical cycles and carrier wavelength of 780 nm.

x-projection of the dipole acceleration and are linearly polarized along the minor axis of the driving field polarization ellipse. A similar picture is seen in the case of $R = 3$ a.u., Fig. 6.3b. Here the dominant contribution for all the harmonics except H9–H13 comes from the z-projection of the dipole acceleration. Harmonics H9 and H11, which exhibit anomalous ellipticity dependence, have dominant contributions from the x-projection of the dipole acceleration and are polarized along the minor axis of the polarization ellipse of the driving laser field. Finally, the harmonic H13 has comparable contributions from both projections of the dipole acceleration and may exhibit elliptical polarization. Note that the contributions from the x-projection of the dipole acceleration dominate the harmonics with anomalous ellipticity dependence in spite of the driving field still having the largest projection in the z-direction. This observation suggests that a resonance mechanism may be involved in the phenomenon of anomalous ellipticity dependence. The resonance emission must occur from the state with the angular momentum projection onto the molecular axis equal to one, otherwise the radiation cannot be polarized in the x-direction. In Table 6.1, we list several first excited states of H_2^+ at $R = 2$ a.u. and $R = 3$ a.u. with their excitation energies. As one can see, $1\pi_u$

Table 6.1: Vertical excitation energies $\Delta E_n = E_n - E_0$ of H_2^+ in atomic units and units of ω_0 at internuclear separations 2 and 3 a.u. The ground state energy $E_0 = -1.1026$ a.u. at $R = 2$ a.u. and $E_0 = -0.9109$ a.u. at $R = 3$ a.u.

$R = 2$ a.u.			$R = 3$ a.u.		
State	ΔE_n (a.u.)	$\Delta E_n/\omega_0$	State	ΔE_n (a.u.)	$\Delta E_n/\omega_0$
$1\sigma_u$	0.43510	7.45	$1\sigma_u$	0.20948	3.59
$1\pi_u$	0.67386	11.54	$1\pi_u$	0.52445	8.98
$2\sigma_g$	0.74177	12.70	$2\sigma_g$	0.59201	10.13
$2\sigma_u$	0.84722	14.50	$3\sigma_g$	0.65392	11.19
$3\sigma_g$	0.86686	14.84	$2\sigma_u$	0.65772	11.26
$1\pi_g$	0.87593	15.00	$1\pi_g$	0.68121	11.66
$1\delta_g$	0.88990	15.23	$1\delta_g$	0.70701	12.10
$2\pi_u$	0.90177	15.44	$2\pi_u$	0.72344	12.38
$4\sigma_g$	0.92495	15.83	$4\sigma_g$	0.74830	12.81
$3\sigma_u$	0.96532	16.53	$5\sigma_g$	0.77134	13.21
$5\sigma_g$	0.97184	16.64	$3\sigma_u$	0.77553	13.28
$2\pi_g$	0.97592	16.71	$4\sigma_u$	0.78201	13.39
$4\sigma_u$	0.97599	16.71	$3\pi_u$	0.78319	13.41
$3\pi_u$	0.97644	16.72	$2\pi_g$	0.78342	13.41
$1\delta_u$	0.97767	16.74	$1\delta_u$	0.78607	13.46
$1\phi_u$	0.97951	16.77	$1\phi_u$	0.78986	13.52
$2\delta_g$	0.98161	16.80	$2\delta_g$	0.79359	13.59
$4\pi_u$	0.98672	16.89	$4\pi_u$	0.80083	13.71

state may be responsible for the anomalous ellipticity dependence of H11 at $R = 2$ a.u. and H9 at $R = 3$ a.u. since its excitation energy is close to the harmonic photon energy. For other harmonics with anomalous ellipticity dependence, $2\pi_u$ and higher-lying excited states with the π_u symmetry may have significant contributions, too.

6.4.1 Resonance analysis in H_2^+

To prove this assumption, we have performed other sets of the calculations. Within our approach, it is possible to remove individual excited states from the propagator in Eq. (6.3) and thus check their importance for the anomalous ellipticity dependence of the harmonics. In Fig. 6.2, besides the results obtained with the help of the full propagator (6.3), we show also the results for the reduced propagators. One set is obtained with the $1\pi_u$ state removed from the propagator, another

set contains the results for both $1\pi_u$ and $2\pi_u$ removed. At $R = 2$ a.u., the harmonics H11 and H13 do not manifest anomalous ellipticity dependence if the $1\pi_u$ state is removed from the time propagation process. Further removal of the $2\pi_u$ state does not change their behavior qualitatively. Thus a conclusion can be made that the anomalous ellipticity dependence of H11 and H13 is mainly due to the resonance excitation of the $1\pi_u$ state. For H15, the situation is more complicated. It seems that excitation of both $1\pi_u$ and $2\pi_u$ states affects the harmonic signal. A significant contribution from the $2\pi_u$ state could be expected since its excitation energy is close to the photon energy of H15 (see Table 6.1). If only the $1\pi_u$ state is removed from the propagator, the maximum in the ellipticity dependence of H15 does not disappear but becomes higher. It requires removal of both the $1\pi_u$ and $2\pi_u$ states for the anomalous ellipticity dependence to disappear. That means, both $1\pi_u$ and $2\pi_u$ states are very important for shaping the anomalous ellipticity dependence of H15. The contributions from these two states to the H15 signal interfere destructively because removing only one of them from the time propagation makes the HG signal not weaker but stronger comapared with the original full propagator result. At the internuclear distance $R = 3$ a.u., the picture appears very clear for H9. This harmonic does not exhibit any anomalous ellipticity dependence when its signal is calculated with the $1\pi_u$ state removed from the propagator. Additional removal of the $2\pi_u$ state does not change the pattern. We may conclude that the anomalous ellipticity dependence of H9 at $R = 3$ a.u. is exclusively due to the resonance excitation of the $1\pi_u$ state, whose excitation energy is indeed very close to that of 9 photons of the fundamental frequency ω_0 (see Table 6.1). For H11 and H13, the maximum in the ellipticity dependence disappears only when both $1\pi_u$ and $2\pi_u$ states are removed. This result resembles that for H15 at $R = 2$ a.u. Excitations of both $1\pi_u$ and $2\pi_u$ states are important in formation of the anomalous ellipticity dependence of H11 and H13; their contributions to the HG signal interfere destructively, and only simultaneous removal of these two states from the propagator destroys the anomalous ellipticity dependence.

The driving laser field with elliptical polarization in the $x-z$ plane can be decomposed into a linearly-polarized components along the z-axis and x-axis. When the ellipticity parameter ε increases, the linearly-polarized component of the field along the z-axis becomes weaker, and that

along the x-axis becomes stronger. Excitation of a molecular orbital with the π symmetry may require absorption of several photons polarized along the z (molecular) axis and at least one photon polarized along the x-axis. Thus the resonant enhancement of the harmonic emission through the π states is not favored by either weak z or x components of the driving field. Then the interplay between the decreasing z and increasing x field components as ε increases yields the anomalous dependence of the affected harmonics with the maximum at a non-zero value of the ellipticity parameter [117]. The position of the maximum depends on the harmonic order (that is, the degree of non-linearity of the HG process) and internuclear separation, which affects the electronic structure and possible tuning into the resonance. Generally one may expect that the maximum is shifted to smaller ellipticities as the harmonic order increases. Emission of higher harmonics requires absorption of a larger number of photons polarized in the z direction. Then, because of the higher degree of non-linearity, the HG signal would drop more rapidly as the z component of the driving field decreases. This expectation is in a fair agreement with the results presented in Fig. 6.2.

6.5 Conclusion

In this work, we have studied the mechanism of anomalous ellipticity dependence of near-threshold harmonics in H_2^+ subject to strong near-infrared laser pulses with the carrier wavelength 780 nm. Our numerical results and analysis reveal that the origin of this phenomenon is mainly in the near-resonant excitation of π_u molecular orbitals in H_2^+. For the lowest affected harmonic (H11 at the intrenuclear distance $R = 2$ a.u. and H9 at $R = 3$ a.u.), the maximum in the ellipticity dependence of the radiation energy is exclusively due to excitation of the $1\pi_u$ state. For higher near-threshold harmonics, higher-lying excited π_u states are important, too. The closer the harmonic to the threshold, the larger number of excited states make significant contributions. All these contributions interfere, resulting in the anomalous ellipticity dependence with a maximum at some non-zero value of the ellipticity parameter. In the vicinity of this value, the harmonics with the anomalous dependence are linearly polarized along the minor axis of the polarization ellipse of the

driving field and may show strong elliptical polarization as well. We note here that the resonances with the π_u states have their signatures in other strong-field processes, such as HHG of oriented molecules [122] and multiphoton ionization [58].

We performed the calculations for the fixed nuclei at two different internuclear separations, $R = 2$ a.u. and $R = 3$ a.u. The group of near-threshold harmonics, which exhibit anomalous ellipticity behavior, only slightly depends on the internuclear separation (H11 to H17 at $R = 2$ a.u. and H9 to H13 at $R = 3$ a.u.). For H_2^+ on the lowest vibrational energy level, the nuclear wave packet does not spread beyond $R = 3$ a.u. Thus we may expect that the near-threshold harmonics will exhibit anomalous ellipticity dependence in vibrating molecules as well.

Chapter 7

Harmonic Generation of Li Atoms in One- and Two-photon Rabi-flopping Regimes

7.1 Introduction

High-order-harmonic generation (HHG) is a fundamental atomic and molecular process in strong laser fields that continues attracting much interest in recent years both experimentally and theoretically [67]. With tunable long-wavelength lasers available, sufficiently high intensities without saturation of ionization can be used for probing both valence and core electrons. HHG processes have a capability of imaging of atomic and molecular structures with high resolution in spatial and temporal domains [56, 116]. The multielectron structural information can be retrieved by means of the HHG interferometry which is established as an effective approach to resolving multielectron dynamics. With laser pulses as short as a few femtoseconds, HHG spectroscopy can also become a possible tool for probing chemical reactions on a femtosecond time scale. Recently the emphasis is more and more shifted from observation of atoms and molecules interacting with laser fields towards their control. Coherent control of photon emission [16] and transient absorption [17] are promising directions in further advancements of ultrafast laser spectroscopy and other related applications.

7.1.1 Rabi oscillations and the population transfer

Since the pioneering work of Rabi [101], coherent population transfer among different energy states has been a powerful technique in controlling quantum systems [18, 7]. In a two-level atomic system interacting with a resonant radiation field, the dynamics of the electronic population presents well-known periodic Rabi oscillations. The phase of Rabi oscillations is associated with the so-called "pulse area". When the latter reaches the value of π (π pulse), the population transfer between the two quantum states is complete. Rabi oscillations play an important role in measuring the pulse area and excited-state population. This is directly incorporated with the pulse duration, intensity, detuning from resonance, and the transition dipole moment. Robust coherent control methods based on the concept of Rabi oscillations are utilized in various recent applications such as ultrafast manipulation of Rydberg states [43, 54, 12], quantum information processing [110], ensembles of cold atoms [104, 59, 31] etc.

Rabi flopping in multiphoton regime also became feasible with advancements in laser technology and pulse shaping techniques [64, 105, 71]. However, this regime requires stronger radiation fields resulting in sloppy population transfer to the target state. The process may become out of control when large a.c. Stark shifts detune the system from the resonance [132]. It should be noted that the origin and dynamics of the population transfer and oscillations are qualitatively different for weak and strong radiation fields [32, 89]. In the one-photon transition, the underlying mechanism of population oscillations is different from that in the two-photon transition since in the latter case the resonant intermediate states are affected. For the same pulse area, complications get more serious as the length of the pulse decreases and the peak intensity becomes higher.

Alkali atoms are of particular interest in both experimental and theoretical studies of light-matter interaction. For the theoretical description, it is important that alkali atoms have a single electron outside the closed shell and can be quite accurately represented by single-active-electron (SAE) models [90, 25]. A recent theoretical work [25] revealed signatures of the carrier-wave Rabi flopping (CWRF) in the harmonic generation spectra of potassium atoms. The CWRF regime [55] is reached when the Rabi frequency becomes comparable with the carrier frequency and charac-

terized by breakdown of the pulse area theorem. In Ref. [25], it was found that the third harmonic in the harmonic generation spectra of K atoms exhibits a complex structure in the CWRF regime. Previously, a similar pattern was reported for the third harmonic generated in narrow-band semiconductors [91].

7.1.2 The self-interaction free time-dependent density-functional theory (TDDFT) in coherent population transfer in Li atoms

In the present work, we study the influence of the coherent population transfer in Li atoms on the harmonic generation (HG) spectra in the one- and two-photon Rabi-flopping regimes. Lithium is the lightest alkali atom and has a single *s* valence electron. On the other hand, it is the simplest atom that exhibits inter-shell electron correlation which can provide a richer testing ground for the theoretical investigation of the interaction of the atom with intense laser fields. While SAE models with the state-of-the-art effective potentials and pseudopotentials may appear very accurate in description of alkali atoms (see, for example, the review article [113] and references therein), they still lack the dynamic multielectron response of the atomic core to the laser fields, which may be significant and affect the outer electron even when the inner electrons are tightly bound. Our theoretical approach goes beyond the SAE approximation and is based on the self-interaction-free time-dependent density-functional theory (TDDFT), which takes into account the electron exchange and correlation through the exchange-correlation functional. Here we use it specifically to study HG of Li atoms driven by strong near-resonant laser fields with realistic parameters such as carrier frequency, peak intensity, and pulse duration that can be used to control the shape and structure of the harmonic peaks. It should be noted that recent TDDFT studies [107, 42, 41] revealed failures to describe the Rabi dynamics in two-electron model systems initially in the ground singlet states. Such systems, when treated by TDDFT with adiabatic exchange-correlation functionals (where the potential at any time is a functional of the density at that time), featured incomplete population transfer to the excited states and detuned Rabi oscillations [42]. The system is driven out of resonance when the density changes significantly due to the population transfer to

the excited states thus causing a change in the adiabatic Kohn-Sham potential. A conclusion was made [42, 41] that non-adiabaticity of the exchange-correlation functional is crucial to properly capture the physics of Rabi oscillations, and adiabatic functionals would fail to do so. However, as our calculations show, this problem is not severe for the Li atom, which has only one $2s$ electron outside the closed $1s$ shell. The transitions of the valence electron do not affect too much the tightly bound core electrons. That is why the Kohn-Sham mean field experienced by the valence electron does not manifest dramatic changes when the population transfer occurs between the $2s$ and excited states, and the system does not go off the resonance.

For the one-photon Rabi-flopping case, we choose the carrier frequency tuned into the resonance with the transition between the ground $2s$ and the first excited $2p$ states (D-line in the radiation spectrum of Li; the experimental wavelength is 671 nm). The two-photon Rabi-flopping regime can be reached when the carrier frequency of the laser pulse is tuned into the two-photon resonance between the ground $2s$ state and excited $3s$ or $3d$ states. In the HG spectra, we observe characteristic oscillatory structures and explain their relations to the Rabi flopping and pulse-shape-induced interferences. We also discuss systematic shifts of the harmonic peaks when the carrier frequency has a small detuning from the resonance. Our findings can be used for the purpose of coherent control of HG in the Rabi-flopping regime.

7.2 Mathematical details on employing self-interaction free TDDFT in Li atoms

We use TDDFT to study harmonic generation of Li atoms driven by strong near-resonant laser fields. The single-particle potential is constructed by means of the Krieger-Li-Iafrate (KLI) procedure [68] with self-interaction correction (SIC) extended to the time-dependent (TD) problems [130]. For the TD-KLI-SIC procedure [130] adopted here, we extend Perdew and Zunger's SIC form [97] to the time domain. It has been shown [130] that the TDKLI procedure [133] can be simplified considerably without the need of using the nonlocal Hartree-Fock energy functional, in

the construction of the time-dependent optimized effective potential. Thus the TD-KLI-SIC procedure [130] is computationally more efficient and yet maintains high accuracy in the calculation of the ground state energies, ionization potentials, excited autoionizing resonances [129], as well as multiphoton ionization dynamics [130, 19]. Within the adiabatic approximation, well justified in the case of low-frequency laser fields [127], the TD-KLI-SIC single-particle potential can be expressed as follows:

$$V_\sigma^{\rm s}(\boldsymbol{r},t) = \sum_{j=1}^{N_\sigma} \frac{\rho_{j\sigma}(\boldsymbol{r},t)}{\rho_\sigma(\boldsymbol{r},t)} \left[v_{j\sigma}(\boldsymbol{r},t) + \bar{V}_{\sigma j}^{\rm s} - \bar{v}_{j\sigma} \right]. \tag{7.1}$$

Here indices j and σ enumerate spin-orbitals (σ corresponds to the spin projection, N_σ is the total number of electrons with the spin σ); $\rho_{j\sigma}$ and ρ_σ are the spin-orbital density and the total spin-density, respectively:

$$\begin{aligned} \rho_{j\sigma}(\boldsymbol{r},t) &= |\psi_{j\sigma}(\boldsymbol{r},t)|^2, \\ \rho_\sigma(\boldsymbol{r},t) &= \sum_{j=1}^{N_\sigma} \rho_{j\sigma}(\boldsymbol{r},t) \end{aligned} \tag{7.2}$$

($\psi_{j\sigma}(\boldsymbol{r},t)$ is the Kohn-Sham spin-orbital). The orbital-dependent potential $v_{j\sigma}(\boldsymbol{r},t)$ includes the Hartree and exchange-correlation parts as well as self-interaction corrections. The mean values $\bar{V}_{\sigma j}^{\rm s}$, $\bar{v}_{j\sigma}$ are calculated with the spin-densities $\rho_{j\sigma}(\boldsymbol{r},t)$:

$$\begin{aligned} \bar{V}_{\sigma j}^{\rm s} &= \int d^3 r \rho_{j\sigma}(\boldsymbol{r},t) V_\sigma^{\rm s}(\boldsymbol{r},t), \\ \bar{v}_{j\sigma} &= \int d^3 r \rho_{j\sigma}(\boldsymbol{r},t) v_{j\sigma}(\boldsymbol{r},t). \end{aligned} \tag{7.3}$$

Eq. (7.1) defines the potential $V_\sigma^{\rm s}(\boldsymbol{r},t)$ up to an arbitrary constant. However, since the exchange-correlation potential vanishes at infinity in the space domain, its expectation value with the highest-occupied spin-orbital $\psi_{m\sigma}(\boldsymbol{r},t)$ must be equal to that of the orbital-dependent potential $v_{m\sigma}(\boldsymbol{r},t)$ [68]:

$$\bar{V}_{\sigma m}^{\rm s} = \bar{v}_{m\sigma}. \tag{7.4}$$

The constraint (7.4) makes the potential (7.1) unique, and all unknown constants $\bar{V}^{\rm s}_{\sigma j}$ ($j < m$) can be obtained solving a set of linear equations [68].

For Li atoms, the procedure is particularly straightforward since N_σ does not exceed 2. For the open-shell Li atom (the electronic structure $1s^2 2s$), the TD-KLI-SIC potential is spin-dependent and can be explicitly written as follows, for the spin up ($\uparrow$) and spin down ($\downarrow$), respectively [124]:

$$\begin{aligned} V^{\rm s}_\uparrow(\boldsymbol{r},t) &= \frac{\rho_{1\uparrow}(\boldsymbol{r},t)}{\rho_\uparrow(\boldsymbol{r},t)}\Big\{v_{1\uparrow}(\boldsymbol{r},t) + \left[\int d^3r \frac{\rho_{2\uparrow}(\boldsymbol{r},t)\rho_{1\uparrow}(\boldsymbol{r},t)}{\rho_\uparrow(\boldsymbol{r},t)}\right]^{-1} \\ &\times \int d^3r \frac{\rho_{2\uparrow}(\boldsymbol{r},t)\rho_{1\uparrow}(\boldsymbol{r},t)}{\rho_\uparrow(\boldsymbol{r},t))}[v_{2\uparrow}(\boldsymbol{r},t) - v_{1\uparrow}(\boldsymbol{r},t)]\Big\} + \frac{\rho_{2\uparrow}(\boldsymbol{r},t)}{\rho_\uparrow(\boldsymbol{r},t)} v_{2\uparrow}(\boldsymbol{r},t), \\ V^{\rm s}_\downarrow(\boldsymbol{r},t) &= v_{1\downarrow}(\boldsymbol{r},t). \end{aligned} \tag{7.5}$$

For the orbital-dependent potentials $v_{j\sigma}(\boldsymbol{r},t)$, we use the exchange-only approximation in the local spin-density (LSD) form, and include Perdew-Zunger [97] self-interaction corrections:

$$v_{j\sigma}(\boldsymbol{r},t) = v_{\rm H}[\rho_\uparrow + \rho_\downarrow](\boldsymbol{r},t) + v^{\rm LSD}_{\rm x}[\rho_\sigma](\boldsymbol{r},t) - v_{\rm H}[\rho_{j\sigma}](\boldsymbol{r},t) - v^{\rm LSD}_{\rm x}[\rho_{j\sigma}](\boldsymbol{r},t) \tag{7.6}$$

where $v_{\rm H}[\rho](\boldsymbol{r},t)$ and $v^{\rm LSD}_{\rm x}[\rho](\boldsymbol{r},t)$ are the Hartree and LSD exchange potentials, respectively:

$$\begin{aligned} v_{\rm H}[\rho](\boldsymbol{r},t) &= \int d^3r' \frac{\rho(\boldsymbol{r},t)}{|\boldsymbol{r}-\boldsymbol{r}'|}, \\ v^{\rm LSD}_{\rm x}[\rho](\boldsymbol{r},t) &= -\left[\frac{6}{\pi}\rho(\boldsymbol{r},t)\right]^{1/3}. \end{aligned} \tag{7.7}$$

The spin-orbital energies computed by the time-independent DFT using these potentials are listed in Table 7.1. The highest-occupied orbital energy is in a good agreement with the experimental data for the ionization potential [5]. In Table 7.2, we list the one-electron excitation energies ($2s \to nl$) calculated as differences of the corresponding eigenvalues of the time-independent DFT Hamiltonian. For comparison, experimental excitation energies are also shown. As one can see, the agreement is fairly good (within 2%). Of course, the differences of the Kohn-Sham orbital energies are only a zero-order approximation to the actual excitation energies of the multielectron atom. A

Table 7.1: Absolute values of spin-orbital energies of Li. (A) Present calculations (a.u.). (B) Experimental ionization energy of Li [5] (a.u.).

Spin-orbital	A	B
$1s\uparrow$	1.993	
$1s\downarrow$	2.476	
$2s\uparrow$	0.196	0.198

better approximation, including the dynamical exchange-correlation effects, can be obtained in the framework of the linear-response TDDFT [13, 98]. For the Li atom, however, the Kohn-Sham level of accuracy is quite good and sufficient to determine the laser frequencies for near-resonant excitations. The same is true for the transition dipole matrix elements calculated between the one-electron Kohn-Sham states with the principal quantum numbers $n = 2$ and $n = 3$ and listed in Table 7.3. Accuracy of these matrix elements is important for correct description of the excitation dynamics in near-resonant laser fields. As one can see, the quality of the calculated transition dipoles is rather good even on the one-electron Kohn-Sham level; they agree well with the matrix elements obtained by the precision linearized coupled-cluster method [111].

7.2.1 Time-dependent electron densities and calculating the harmonic spectra in Li atoms

To obtain the time-dependent electron densities and calculate the harmonic spectra, one has to solve a set of the the time-dependent Kohn-Sham equations for the spin-orbitals $\psi_{j\sigma}(\boldsymbol{r},t)$:

$$i\frac{\partial}{\partial t}\psi_{j\sigma}(\boldsymbol{r},t) = \Big[-\frac{1}{2}\nabla^2 - \frac{Z}{r} + V^{\rm s}_{\sigma}(\boldsymbol{r},t) + v_{\rm ext}(\boldsymbol{r},t)\Big]\psi_{j\sigma}(\boldsymbol{r},t), \quad j = 1,...,N_{\sigma}. \tag{7.8}$$

Besides the discussed single-particle potential $V^{\rm s}_{\sigma}$, the right-hand side of Eq. (7.8) contains the Coulomb interaction with the nucleus (Z is the nucleus charge) and interaction with the external laser field $v_{\rm ext}(\boldsymbol{r},t)$. In our calculations we use a linearly polarized laser pulse; the envelope has a

Table 7.2: $2s \rightarrow nl$ excitation energies of Li. (A) Present calculations (a.u.). (B) Experimental results [102] (a.u.).

nl	A	B
$2p$	0.0673	0.0679
$3s$	0.1219	0.1240
$3p$	0.1389	0.1409
$3d$	0.1401	0.1425

sine-squared shape and contains 20 optical cycles (o.c.):

$$v_{\rm ext}(\boldsymbol{r},t) = (\boldsymbol{F}(t)\cdot\boldsymbol{r}), \tag{7.9}$$

$$\boldsymbol{F}(t) = \boldsymbol{F}_0 \sin^2\frac{\pi t}{T}\sin\omega_0 t, \quad T=\frac{40\pi}{\omega_0}. \tag{7.10}$$

To solve the set (7.8), we apply the time-dependent generalized pseudospectral (TDGPS) method which proved accurate and efficient in our previous atomic TDDFT calculations (see, *e. g.*, Refs. [124, 48, 125, 49]). For the TDGPS discretization in the present calculations, we use 80 radial and 32 angular grid points, and 4096 time steps per optical cycle. The equations (7.8) are solved in space within a sphere with the radius 60 a.u.; between 40 a.u. and 60 a.u. we place an absorber. Absorbed parts of the wave packet localized beyond 40 a.u. describe unbound states populated during the ionization process. We note that the absorber is located far enough from the nucleus, so its influence on the excitation and ionization dynamics is negligible. Because of the absorber, the normalization integrals of the spin-orbital densities $\rho_{j\sigma}(\boldsymbol{r},t)$ decrease in time. The ionization probabilities $P_{j\sigma}$ for each spin orbital are determined by the densities calculated after the pulse:

$$P_{j\sigma} = 1 - \int d^3r \rho_{j\sigma}(\boldsymbol{r},T). \tag{7.11}$$

We note that for the moderate peak intensities used in the calculations (up to 2×10^{12} W/cm^2) only the highest-occupied $2s$ orbital of Li contributes to ionization while the tightly bound inner shell

Table 7.3: Transition dipole matrix elements $\langle n'l'0|z|nl0\rangle$ of Li. (A) Present calculations (a.u.). (B) Ref. [111] (a.u.).

Transition	A	B
$2s \rightarrow 2p$	2.38	2.35
$2s \rightarrow 3p$	0.113	0.129
$2p \rightarrow 3s$	1.77	1.72
$2p \rightarrow 3d$	2.33	2.27

$1s$ electrons do not leave the core. Then the ionization probability of Li $\mathscr{P}$ reads as

$$\mathscr{P} = P_{2\uparrow}. \tag{7.12}$$

To calculate the HG spectra, we use a semiclassical approach, where the basic expressions come from the classical electrodynamics but the classical quantities such as dipole moment and its acceleration are replaced with the corresponding quantum expectation values. The spectral density of radiation energy can be expressed through the Fourier transforms of the dipole acceleration $\boldsymbol{a}(t)$ or dipole moment $\boldsymbol{d}(t)$ [70]:

$$S(\omega) = \frac{2}{3\pi c^3}|\widetilde{\boldsymbol{a}}(\omega)|^2 = \frac{2\omega^4}{3\pi c^3}|\widetilde{\boldsymbol{d}}(\omega)|^2; \tag{7.13}$$

$$\widetilde{\boldsymbol{a}}(\omega) = \int_{-\infty}^{\infty} dt\ \boldsymbol{a}(t)\exp(i\omega t), \tag{7.14}$$

$$\widetilde{\boldsymbol{d}}(\omega) = \int_{-\infty}^{\infty} dt\ \boldsymbol{d}(t)\exp(i\omega t), \tag{7.15}$$

(c is the speed of light) and the expectation values of the dipole moment and its acceleration are defined as follows:

$$\boldsymbol{d}(t) = \int d^3r\ \boldsymbol{r}\ [\rho_\uparrow(\boldsymbol{r},t) + \rho_\downarrow(\boldsymbol{r},t)]; \tag{7.16}$$

$$\boldsymbol{a}(t) = -\int d^3r\ [\rho_\uparrow(\boldsymbol{r},t) + \rho_\downarrow(\boldsymbol{r},t)] \times \nabla[-\frac{Z}{r} + v_{\rm ext}(\boldsymbol{r},t)]. \tag{7.17}$$

They satisfy the same relation as the corresponding classical quantities:

$$\frac{d^2}{dt^2}\boldsymbol{d}(t) = \boldsymbol{a}(t). \tag{7.18}$$

Table 7.4: Ionization probabilities ($\mathscr{P}$), Rabi frequencies (Ω), and pulse areas (Θ) for the resonant 20 o.c. $\sin^2$ laser pulses with the carrier wavelength 676 nm.

Peak intensity (W/cm^2)	$\mathscr{P}$	Ω (a.u.)	Θ/π
2.0×10^{11}	0.019	0.00568	1.69
2.8×10^{11}	0.031	0.00672	2.00
3.0×10^{11}	0.035	0.00696	2.07
3.2×10^{11}	0.038	0.00719	2.13
5.0×10^{11}	0.069	0.00899	2.67
1.0×10^{12}	0.135	0.01271	3.77
1.3×10^{12}	0.170	0.01449	4.30
2.0×10^{12}	0.268	0.01797	5.33

The expression for $\boldsymbol{a}(t)$ can be derived from that for $\boldsymbol{d}(t)$ with the help of the Ehrenfest theorem. We note that only the nuclear and external field potentials are present in Eq. (7.17). When multielectron targets are treated exactly, the electron-electron interaction *does not* contribute to the expectation value of the dipole acceleration due to Newton's third law since the electrons are identical and have the same masses and charges. In TDDFT, that means the *exact* exchange-correlation potential (as well as the Hartree potential) does not contribute to the expectation value of acceleration (the zero-force theorem [134]). For approximate exchange-correlation potentials, this is not always true. Consequently, the length and acceleration forms of the HG spectra (7.13) with the expectation values defined in Eqs. (7.16) and (7.17) are not necessarily identical in TDDFT. This is specifically the case for the TD-KLI-SIC approximation, which is known to violate the zero-force theorem [93]. In this study, we adopt the length form of the HG spectra as defined by equations (7.13), (7.15), and (7.16).

7.2.2 One-photon Rabi flopping regime

In order to have an efficient control over the coherent population transfer in the one-photon Rabi-flopping regime, we set the carrier wavelength to 676 nm ($\omega_0 = 0.0674$ a.u.) corresponding to a resonance one-photon transition between the ground $2s$ and the first excited $2p$ states (D line in the radiation spectrum of Li; the experimental wavelength is 671 nm). Several peak intensities in the range 2×10^{11} to 2×10^{12} W/cm^2 have been used in the calculations. Since the excitation

dynamics in the resonant field is closely related to the Rabi oscillations and Rabi flopping, let us introduce the Rabi frequency and pulse area. The Rabi frequency Ω is defined as a product of the peak value of the laser electric field F_0 and transition dipole D between the resonant atomic states:

$$\Omega = F_0 D. \tag{7.19}$$

Then the pulse area Θ is a product of the Rabi frequency Ω and the full width at the half maximum (FWHM) of the laser pulse τ [for the $\sin^2$ pulse, the latter is just one half of the total pulse duration T, see Eq. (7.10)]:

$$\Theta = \Omega\tau. \tag{7.20}$$

In the Rabi-flopping regime, the population inversion after the pulse occurs if the pulse area is equal to an odd integer in units of π. For the simplified two-level system, it corresponds to the total depletion of the initial ground state and full population of the excited state. For more realistic multilevel system, this is not the case because a part of the initial population of the ground state may go to other (non-resonant) excited states. Still, the population of the resonant excited state at the end of the pulse can be very significant. If the pulse area is equal to an even integer in units of π, then the most of the population returns to the initial ground state after the pulse.

In Table 7.4, we present ionization probabilities, Rabi frequencies, and pulse areas for different peak intensities used in the calculations (our laser pulse always has a $\sin^2$ envelope and duration of 20 o.c.). Note that the Rabi frequency is much less than the laser carrier frequency for all intensities in the range. As one can see, at the highest intensity 2.0×10^{12} W/cm^2 ionization of the Li atom is substantial. Using even higher intensities may result in full ionization on the leading edge of the laser pulse and suppression of harmonic generation. Based on the pulse area calculated according to Eq. (7.20), one may expect the largest ground state population after the 2π-pulse with the peak intensity 2.8×10^{11} W/cm^2. However, the pulse area analysis is an approximate tool coming from the adiabatic two-level system theory. Our numerical calculations show that the largest ground state population after the pulse actually corresponds to the peak intensity $3.2 \times$

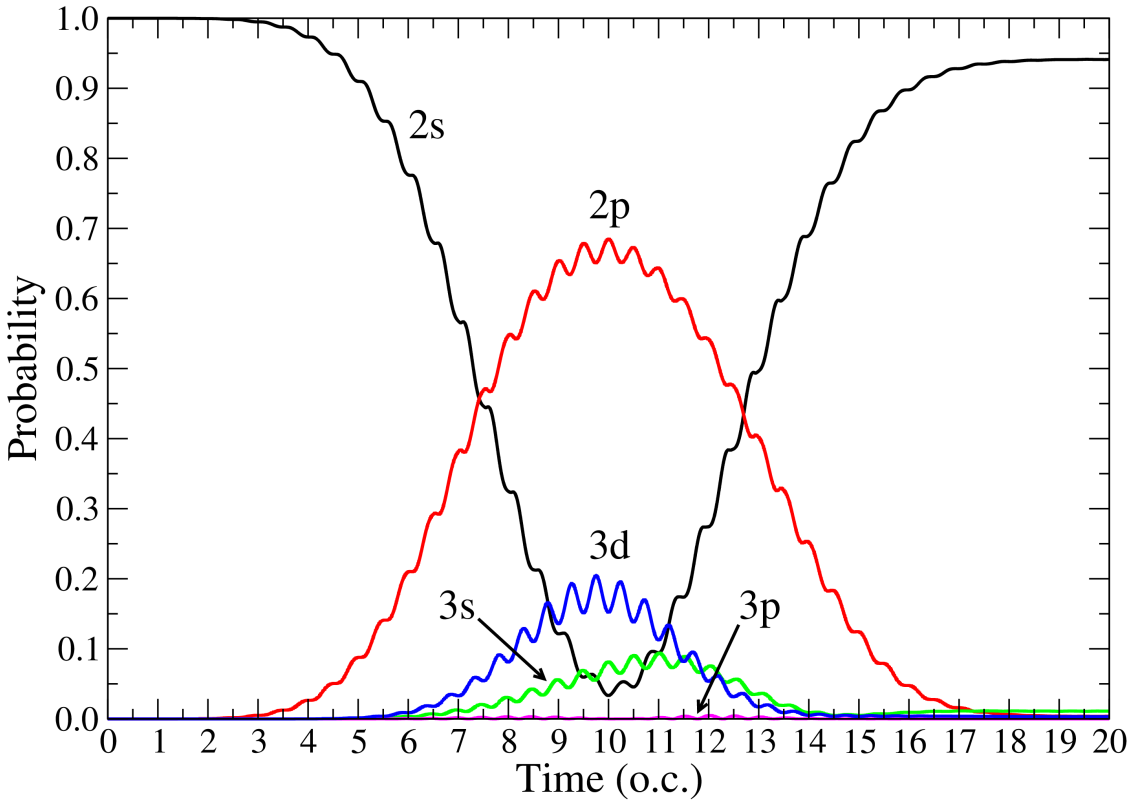

Figure 7.1: Time-dependent populations of the ground and several excited states of Li. The laser pulse has a $\sin^2$ shape, duration of 20 o.c., and peak intensity is 3.2×10^{11} W/cm^2. The carrier wavelength 676 nm corresponds to a one-photon resonance between $2s$ and $2p$ states.

10^{11} W/cm^2 and pulse area 2.13π. In Fig. 7.1, the time-dependent populations of the ground ($2s$) and several excited Kohn-Sham states are shown. Similar to the above discussion of the excitation energies and transition dipoles, we should note here that for the Li atom the Kohn-Sham populations are a good approximation for the populations of the ground and singly-excited multielectron states. Besides the resonant $2p$ state, significant populations in the central part of the laser pulse are acquired by the $3s$ and $3d$ states; this happens because these two states are strongly coupled to the $2p$ state (see transition dipoles in Table 7.3), and their excitation energies (Table 7.2) are not far away from the two-photon resonance with the ground state. On the contrary, the population of the $3p$ state is very low (does not exceed 0.005) because this state is not accessible from the $2p$ state through a one-photon process, and transitions from either $2s$, $3s$, and $3d$ states are far from resonance.

The time-dependent dipole moment for the same laser pulse with the peak intensity 3.2×10^{11} W/cm^2 is shown in Fig. 7.2. The induced dipole moment features a deep low-frequency modulation with the minimum of the envelope at the center of the laser pulse. The modulation frequency is just the Rabi frequency; for this particular laser pulse it is approximately equal to one tenth of the carrier frequency: $\Omega \approx 0.1\omega_0$. The minimum in the induced dipole corresponds to almost full population transfer from the $2s$ state to the $2p$ state at half pulse duration. Note that the dipole moment does not vanish at the end of the laser pulse. It happens because some population still remains in the excited $2p$ state. The frequency of the dipole oscillations at the end of the pulse is not actually the carrier frequency ω_0 of the laser field but the excitation energy of the $2p$ state; the latter, however, is equal to ω_0 in the resonant field.

To calculate the spectrum of radiation emitted during the interaction with the laser field, one has to perform the Fourier transform of the induced dipole moment [see Eqs. (7.13) and (7.15)]. Since we do not propagate the Kohn-Sham orbitals beyond the end of the laser pulse, the temporal integration in Eq. (7.15) is restricted to the interval from 0 to T, that is the pulse duration. This approach assumes that the dipole moment smoothly goes to zero at both beginning and end of the pulse, otherwise the Fourier transform may contain spurious contributions and noise because of

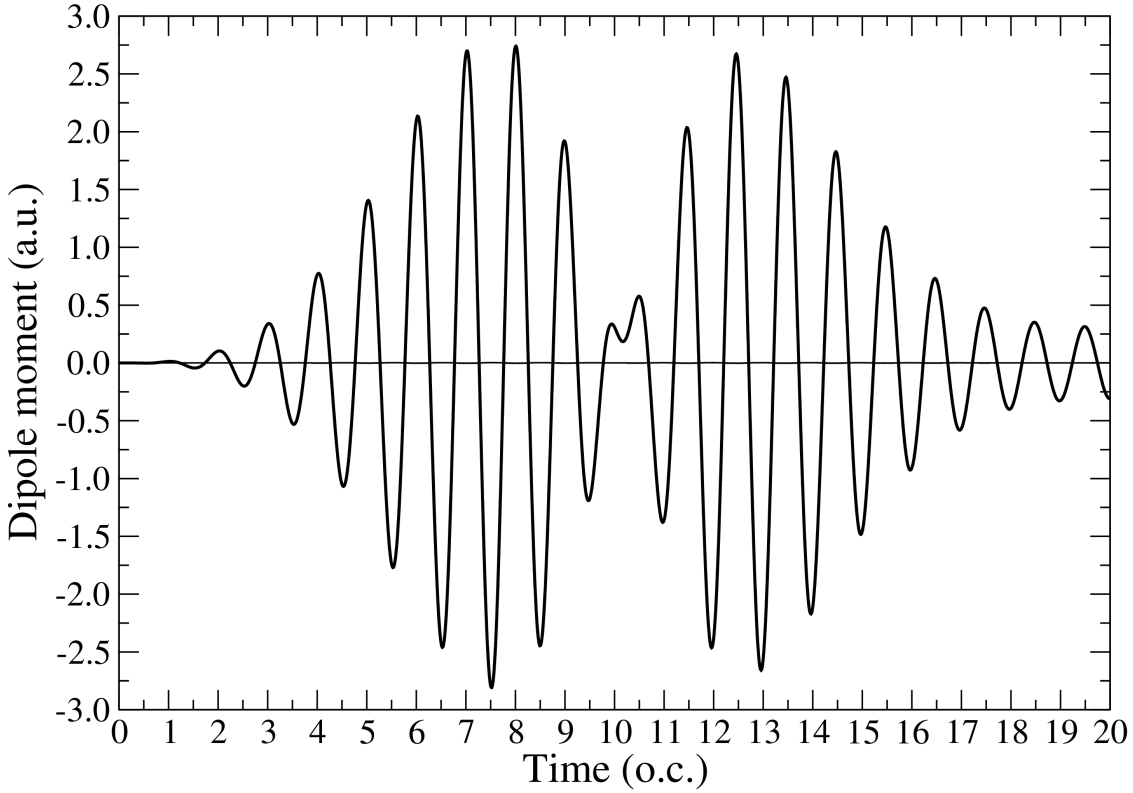

Figure 7.2: Time-dependent induced dipole moment in the resonant field. The laser pulse has a $\sin^2$ shape, duration of 20 o.c., and peak intensity is 3.2×10^{11} W/cm^2. The carrier wavelength 676 nm corresponds to a one-photon resonance between $2s$ and $2p$ states.

abrupt change of the integrand in Eq. (7.15). As one can see in Fig. 7.2, in the case of the resonant (or near-resonant) field, at the end of the pulse the dipole moment still oscillates with a quite large magnitude and does not vanish. To avoid any unwanted effects in the Fourier transform, before taking the integral in Eq. (7.15), we multiply the dipole moment by the window function, which is equal to unity in the central part of the laser pulse and smoothly goes to zero at both $t = 0$ and $t = T$. In our calculations, we use the following window function $W(t)$:

$$W(t) = \begin{cases} \sin^2\left(\dfrac{\omega_0 t}{8}\right), & 0 \le t < \dfrac{4\pi}{\omega_0}; \\ 1, & \dfrac{4\pi}{\omega_0} \le t < T - \dfrac{4\pi}{\omega_0}; \\ \sin^2\left(\dfrac{\omega_0 (T-t)}{8}\right), & T - \dfrac{4\pi}{\omega_0} \le t \le T. \end{cases} \tag{7.21}$$

Defined in this way, the function $W(t)$ gradually raises from 0 to 1 during the first two optical cycles, remain equal to unity for the next 16 optical cycles, and gradually decreases to zero during the last two optical cycles.

In Fig. 7.3, we show the HG spectrum obtained by the Fourier transform with the window function (7.21) for the same laser pulse with the carrier wavelength 676 nm and peak intensity 3.2×10^{11} W/cm^2. The spectrum consists of distinct odd harmonic peaks manifesting fine oscillatory structures. We note that at the laser wavelength 676 nm the third harmonic already corresponds to the photon energy slightly above the ionization threshold, so all generated harmonics are above-threshold, and their frequency profiles are rather broad. The most prominent feature of the spectrum is an oscillatory structure superimposed onto the conventional harmonic peaks. The spacing between the adjacent maxima of this structure is about $0.2\omega_0$, that is twice the Rabi frequency. The origin of these fine oscillations in the frequency domain can be understood from the analysis of the properties of the induced dipole moment in the time domain, which is strongly affected by the population transfer in the resonant field. In the two-level system, the dipole moment vanishes when does so the population of any of the two states strongly coupled by the field. Although this example is oversimplified, it catches the physics of the process; we can see a deep

minimum of the dipole moment induced by the field in the Li atom (Fig. 7.2) when the $2s$ state is almost depleted. The pattern in Fig. 7.2 exhibits two well-separated portions shifted from each other by 5 o.c. or half the Rabi period, π/Ω. Then we can represent the whole function $d(t)$ as a sum of left and right contributions:

$$d(t) = d_L(t) + d_R(t) \tag{7.22}$$

and approximate the right contribution as the left one shifted by π/Ω:

$$d_R(t) = d_L(t - \pi/\Omega). \tag{7.23}$$

Performing the Fourier transform of $d(t)$, one obtains:

$$\widetilde{d}(\omega) = 2\exp\left(i\frac{\pi\omega}{2\Omega}\right)\cos\left(\frac{\pi\omega}{2\Omega}\right)\widetilde{d}_L(\omega). \tag{7.24}$$

The spectral density of emitted radiation energy will manifest an oscillatory structure with the adjacent maxima separated by $\Delta\omega = 2\Omega$:

$$S(\omega) = \frac{8\omega^4}{3\pi c^3}\cos^2\left(\frac{\pi\omega}{2\Omega}\right)|\widetilde{d}_L(\omega)|^2. \tag{7.25}$$

Although the above analysis is approximate, it reveals the origin of the oscillatory structure in the HG spectrum. This structure appears due to low-frequency modulation of the time-dependent dipole moment. The modulation, in turn, has its origin in the population oscillations with the Rabi frequency. We should note that the modulation affects not only the visible time evolution of the dipole moment (with the carrier frequency ω_0) shown in Fig. 7.2. Higher harmonics also exhibit such a modulation. We can extract time profiles for higher harmonics performing inverse Fourier transforms on the limited frequency range, corresponding to the specific harmonic. For example,

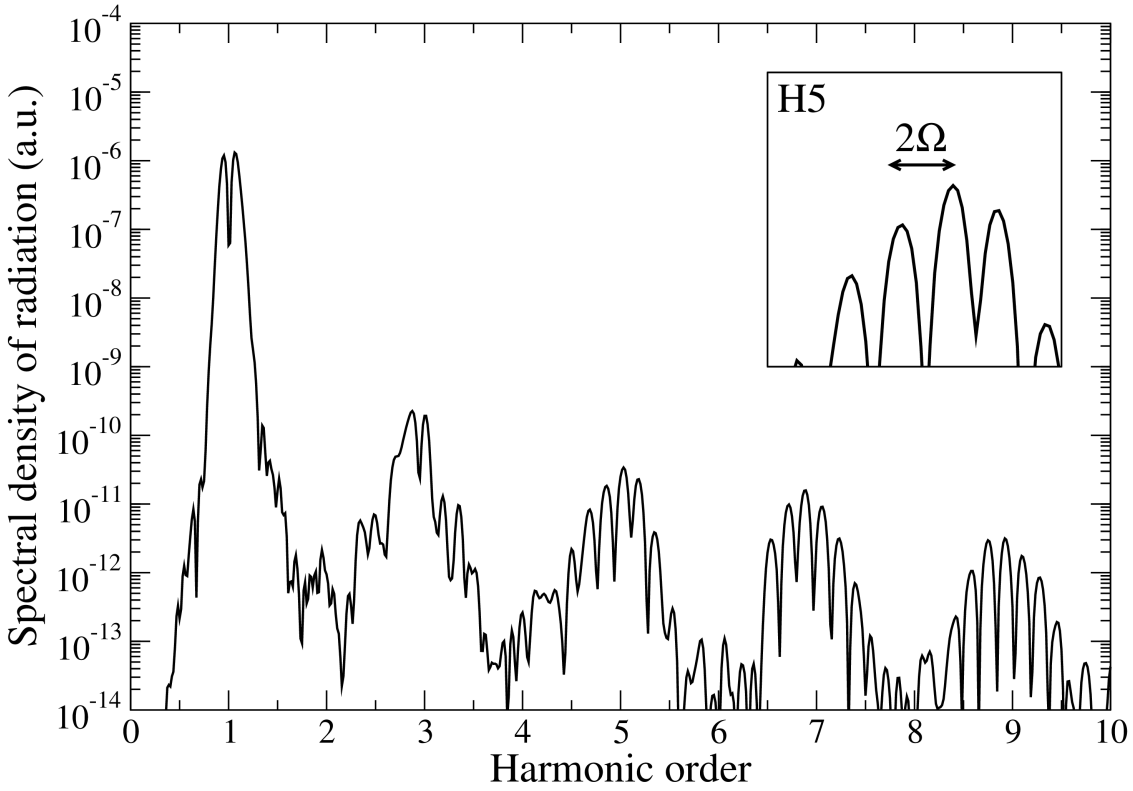

Figure 7.3: HG spectrum of Li. The laser pulse has a $\sin^2$ shape, duration of 20 o.c., and peak intensity is 3.2×10^{11} W/cm^2. The carrier wavelength 676 nm corresponds to a one-photon resonance between $2s$ and $2p$ states. The inset shows enlarged structure of the 5th harmonic with the spacing between two adjacent subpeaks equal to 2Ω.

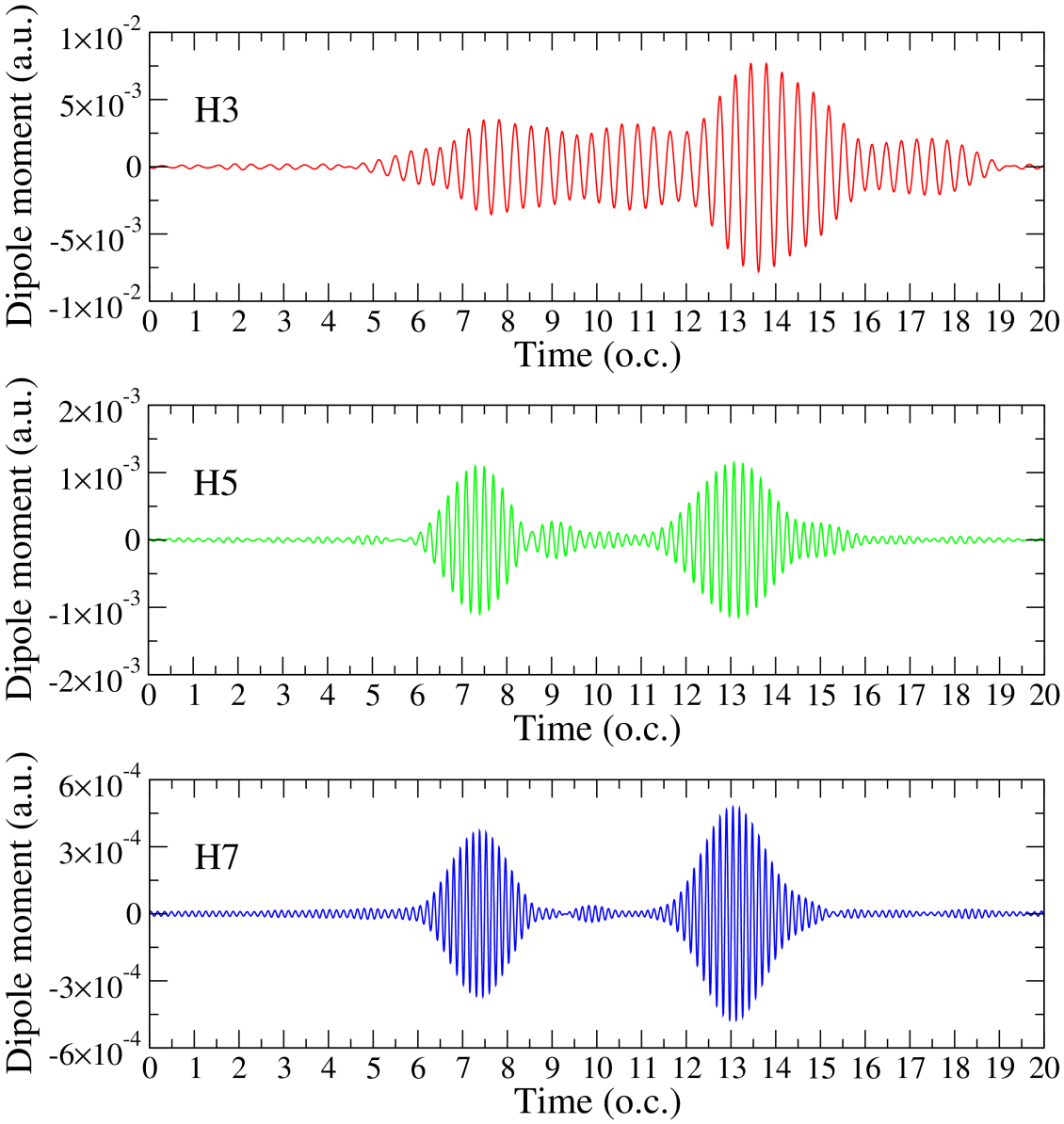

Figure 7.4: Time profiles of the 3rd, 5th, and 7th harmonics. The laser pulse has a $\sin^2$ shape, duration of 20 o.c., and peak intensity is 3.2×10^{11} W/cm^2. The carrier wavelength 676 nm corresponds to a one-photon resonance between $2s$ and $2p$ states.

taking the inverse Fourier transform of $\widetilde{d}(\omega)$ restricted to the frequency range $[2.5\omega_0, 3.5\omega_0]$, we obtain the time profile for the third harmonic, and similar for other harmonics. In Fig. 7.4, the time profiles for the harmonic orders 3, 5, and 7 are shown. As one can see, the 5th and 7th harmonics exhibit a well-pronounced low-frequency modulation similar to that seen in Fig. 7.2. The time profile for the third harmonic is somewhat different; although the modulation is present, its frequency cannot be easily extracted from the time profile since there is only one dominant contribution from the time interval 13 to 15 o.c. Nonetheless, the third harmonic also exhibits a subpeak structure in the frequency domain (see Fig. 7.3) with the spacing between the subpeaks approximately equal to 2Ω.

7.2.3 Effect of the pulse shape: interference oscillatory structures in HG spectra

At higher peak intensities of the laser pulse, fine oscillatory structures with the subpeak spacing less than 2Ω can be noticed in the harmonic peaks. In Fig. 7.5, such structures contained within 2Ω frequency intervals are clearly seen in the 5th and 7th harmonics at the peak intensity 1×10^{12} W/cm^2. This phenomenon can be explained by interference of the contributions to the HG spectrum coming from the leading and trailing edges of the laser pulse. As early as in 1984, it was discovered [108] that the spectrum of resonance fluorescence of a two-level system has a multipeak structure. Similar structures were found in the spectra of resonance ionization [106], resonance autoionization [109, 62] and multiphoton above-threshold detachment [120]. In Refs. [62, 120], a concept of adiabatic Floquet states [51, 35] was used to explain the multipeak structures in the spectra. The same approach is applicable for description of the HG spectra.

For the sake of simplicity, let us consider the case when the carrier frequency is tuned into the exact resonance with the transition between the $2s$ and $2p$ states. In this case, the time-dependent wave function can be represented by an equally weighted linear combination of *two* adiabatic

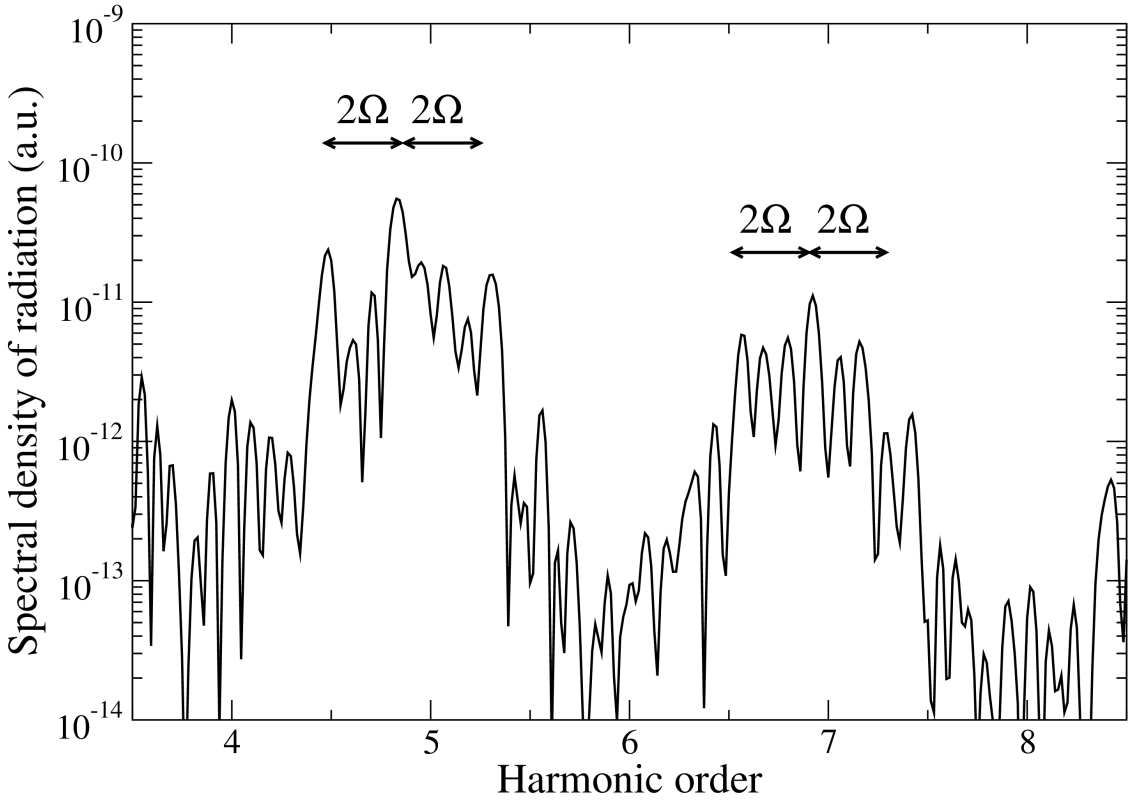

Figure 7.5: Fine structures of the 5th and 7th harmonics. The subpeak spacing is less than 2Ω. The laser pulse has a $\sin^2$ shape, duration of 20 o.c., and peak intensity is 1×10^{12} W/cm^2. The carrier wavelength 676 nm corresponds to a one-photon resonance between $2s$ and $2p$ states.

Floquet states:

$$\psi = \frac{1}{2}\Big\{ \exp\left[-i\int_0^t \varepsilon_a(\tau)d\tau\right]\psi_a + \exp\left[-i\int_0^t \varepsilon_b(\tau)d\tau\right]\psi_b\Big\}, \tag{7.26}$$

where ψ_a and ψ_b can be expanded in Fourier series:

$$\psi_a = \sum_n \psi_{a,n}\exp(-in\omega_0 t), \tag{7.27}$$

$$\psi_b = \sum_n \psi_{b,n}\exp(-in\omega_0 t). \tag{7.28}$$

The quasienergies ε_a, ε_b and Fourier components $\psi_{a,n}$, $\psi_{b,n}$ depend on time *adiabatically* through the pulse envelope function. In the weak laser field limit, the adiabatic quasienergies ε_a and ε_b become degenerate (and equal to the $2s$ orbital energy), and the wave functions have the following approximate expressions:

$$\psi_a \approx \frac{1}{2}\left[\psi_{2s} + \exp(-i\omega_0 t)\psi_{2p}\right], \tag{7.29}$$

$$\psi_b \approx \frac{1}{2}\left[\psi_{2s} - \exp(-i\omega_0 t)\psi_{2p}\right], \tag{7.30}$$

where ψ_{2s} and ψ_{2p} denote unperturbed time-independent $2s$ and $2p$ wave functions, respectively. Then only the $2s$ state is populated at the beginning of the laser pulse ($t = 0$).

With the wave function (7.26), the expectation value of the induced dipole moment is calculated as follows:

$$d(t) = \frac{1}{4}\Big\{ \langle\psi_a|z|\psi_a\rangle + \langle\psi_b|z|\psi_b\rangle + \exp\left[i\int_0^t (\varepsilon_a - \varepsilon_b)d\tau\right]\langle\psi_a|z|\psi_b\rangle + \exp\left[i\int_0^t (\varepsilon_b - \varepsilon_a)d\tau\right]\langle\psi_b|z|\psi_a\rangle\Big\}. \tag{7.31}$$

Note that in the resonance field the difference of adiabatic quasienergies is equal to the adiabatic

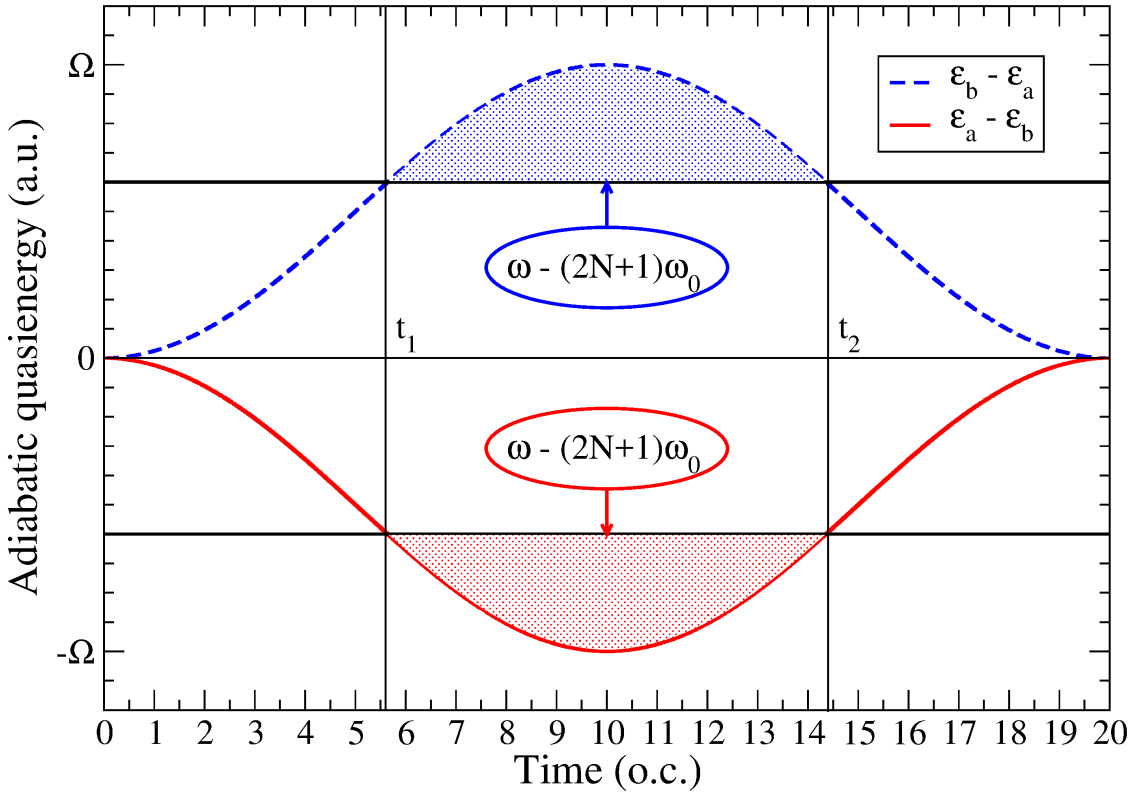

Figure 7.6: Adiabatic quasienergies in the resonance field. The time moments t_1 and t_2 denote the saddle points, and the shaded areas represent the phase difference responsible for the interference oscillations.

Rabi frequency defined for the the electric field peak value at time t:

$$\varepsilon_b(t) - \varepsilon_a(t) = \Omega(t). \tag{7.32}$$

Expanding the right-hand side of Eq. (7.31) in Fourier series, one obtains:

$$\begin{aligned} D(t) = \frac{1}{4}\Big\{ & \sum_n \exp(in\omega_0 t) \left[d_n^{aa} + d_n^{bb} \right] \\ & + \exp\left[i \int_0^t (\varepsilon_a - \varepsilon_b) d\tau \right] \sum_n \exp(in\omega_0 t) d_n^{ab} \\ & + \exp\left[i \int_0^t (\varepsilon_b - \varepsilon_a) d\tau \right] \sum_n \exp(in\omega_0 t) \left[d_{-n}^{ab} \right]^* \Big\} \end{aligned} \tag{7.33}$$

where

$$d_n^{aa} = \sum_m \langle \psi_{a,m+n} | z | \psi_{a,m} \rangle, \tag{7.34}$$

$$d_n^{bb} = \sum_m \langle \psi_{b,m+n} | z | \psi_{b,m} \rangle, \tag{7.35}$$

$$d_n^{ab} = \sum_m \langle \psi_{a,m+n} | z | \psi_{b,m} \rangle. \tag{7.36}$$

Due to parity restrictions, d_n^{aa}, d_n^{aa}, and d_n^{ab} are non-zero for odd n only.

For the laser field parameters used in the present calculations, the adiabatic Rabi frequency is much less than the carrier frequency at any time: $\Omega(t) \ll \omega_0$. Then the interference oscillatory structure is well localized within a single harmonic frequency profile. For the harmonic order $2n+1$, the time-dependent dipole moment is approximately expressed as

$$\begin{aligned} D_{2n+1}(t) = \frac{1}{4}\Big\{ & \exp[i(2n+1)\omega_0 t] \left[d_{2n+1}^{aa} + d_{2n+1}^{bb} \right] \\ & + \exp\left[i(2n+1)\omega_0 t - i \int_0^t (\varepsilon_b - \varepsilon_a) d\tau \right] d_{2n+1}^{ab} \\ & + \exp\left[i(2n+1)\omega_0 t + i \int_0^t (\varepsilon_b - \varepsilon_a) d\tau \right] \left[d_{-(2n+1)}^{ab} \right]^* \Big\}. \end{aligned} \tag{7.37}$$

The Fourier transform of Eq. (7.37) gives the frequency profile of the $(2n+1)$th harmonic. An

oscillatory pattern in this profile appears due to the contributions of the last two terms in the right-hand side of Eq. (7.37). To evaluate these two contributions to the Fourier integral, we apply the saddle-point method. The equations for the saddle points are as follows (ω being the frequency value where the HG spectrum is calculated):

$$\omega = (2n+1)\omega_0 + [\varepsilon_b - \varepsilon_a](t), \tag{7.38}$$

$$\omega = (2n+1)\omega_0 - [\varepsilon_b - \varepsilon_a](t). \tag{7.39}$$

Obviously, real-valued t solutions of Eq. (7.38) exist only if the frequency ω falls into the interval between $(2n+1)\omega_0$ and $(2n+1)\omega_0 + \Omega$. Similarly, real solutions of Eq. (7.39) exist if the ω value is between $(2n+1)\omega_0 - \Omega$ and $(2n+1)\omega_0$. Since the function $[\varepsilon_b - \varepsilon_a](t)$ is even for symmetric laser pulses, Eqs. (7.38) and (7.39) each produce two saddle points, t_1 and $t_2 = -t_1$, as shown in Fig. 7.6. The contributions from t_1 (leading edge of the laser pulse) and t_2 (trailing edge of the laser pulse) interfere resulting in the oscillatory behavior of the Fourier transform as a function of the frequency ω:

$$\widetilde{d}(\omega) \sim d^{ab}_{2n+1}(t_2) \cos\left[\frac{1}{2}\Theta(t_2)\right], \tag{7.40}$$

where t_2 is determined by ω according to the equation

$$\omega = (2n+1)\omega_0 + [\varepsilon_b - \varepsilon_a](t_2) \tag{7.41}$$

and

$$\widetilde{d}(\omega) \sim \left[d^{ab}_{-(2n+1)}(t_2)\right]^* \cos\left[\frac{1}{2}\Theta(t_2)\right], \tag{7.42}$$

where t_2 is determined by the equation

$$\omega = (2n+1)\omega_0 - [\varepsilon_b - \varepsilon_a](t_2). \tag{7.43}$$

Eqs. (7.40) and (7.42) describe oscillations in the frequency profile of the harmonic on the right

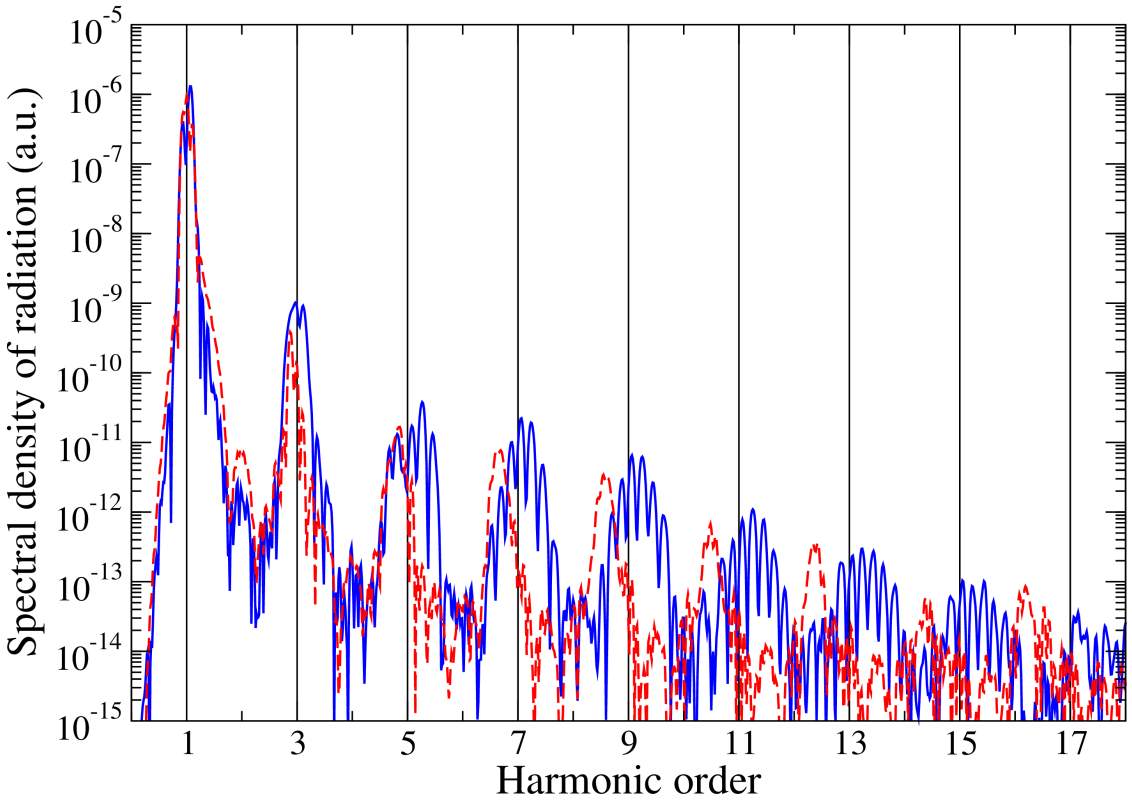

Figure 7.7: HG spectra of Li for the driving field wavelength 650 nm (dashed red line) and 700 nm (solid blue line). The laser pulse has a $\sin^2$ shape, duration of 20 o.c., and peak intensity is 3×10^{11} W/cm^2. The 650 nm and 700 nm spectra are red- and blue-shifted, respectively, from the conventional harmonic positions corresponding to odd integer numbers.

and left of the central line $(2n+1)\omega_0$, respectively. The phase difference $\Theta(t_2)$ is given by the shaded areas in Fig. 7.6 and represents the partial pulse area:

$$\Theta(t_2) = \int_{t_1}^{t_2} dt[\varepsilon_b - \varepsilon_a](t) - (t_2 - t_1)[\varepsilon_b - \varepsilon_a](t_2). \tag{7.44}$$

The multipeak structure due to interference of the contributions from the leading and trailing edges of the laser pulse is contained within the interval of the width 2Ω and appears on both sides of the central line $(2n+1)\omega_0$. The highest subpeaks of this structure are shifted from the central line by the Rabi frequency Ω corresponding to the peak intensity of the laser pulse. The spectral density of the harmonic may exhibit a multipeak structure due to interference as described above if the peak intensity of the pulse is sufficiently high. For the first interference minimum in

the harmonic frequency profile to show up, the pulse area must be greater or equal to π. Since only the central part of the laser pulse (where the field is strong enough) contributes to production of high harmonics, in reality the pulse area should be substantially larger than π to observe this multipeak structure. We should also note that the theoretical description given above is accurate for a two-level system but can be only approximate for real Li atoms. Even in the close vicinity of the $2s-2p$ resonance, population of the other excited states may be significant, especially at high intensities of the laser field, and the resonance approximation involving two adiabatic Floquet states may become invalid.

7.2.4 Blue and red shifts of HG spectra near the resonance

In the vicinity of the resonance, the spectrum of emitted radiation is enhanced and dominated by the transition frequency between the $2s$ and $2p$ states, and its harmonics. When the carrier of the driving laser field has a small detuning from the resonance, the spectrum is still dominated by the harmonics of the transition frequency, and not the carrier frequency. Plotted on the scale of the carrier frequency, the harmonic peaks in the spectrum manifest a blue or red shift from odd integers, depending on the sign of the detuning. In Fig. 7.7, we show the HG spectra for $\sin^2$ laser pulses with the carrier wavelengths 650 nm and 700 nm. For 650 nm, detuning from the resonance (676 nm) is positive (in terms of the frequency), and for 700 nm, detuning is negative. As one can see, the 650 nm and 700 nm spectra have pronounced red and blue shifts, respectively. The shifts of the harmonic peaks are linearly increasing with the harmonic order. This pattern is well explained if it is understood that the positions of the peaks are determined by odd integers of the transition frequency. Then the very first peak is shifted by the negative value of the resonance detuning δ. For the harmonic of the order $2n+1$, the shift is equal to $-(2n+1)\delta$. We note that the systematic red and blue shifts of the harmonics can only be detected in the close vicinity of the resonance. Far from the resonance, the role of the transition frequency in the radiation spectra is not so important, and the harmonic peaks return to their conventional positions at odd integer multiples of the driving field frequency.

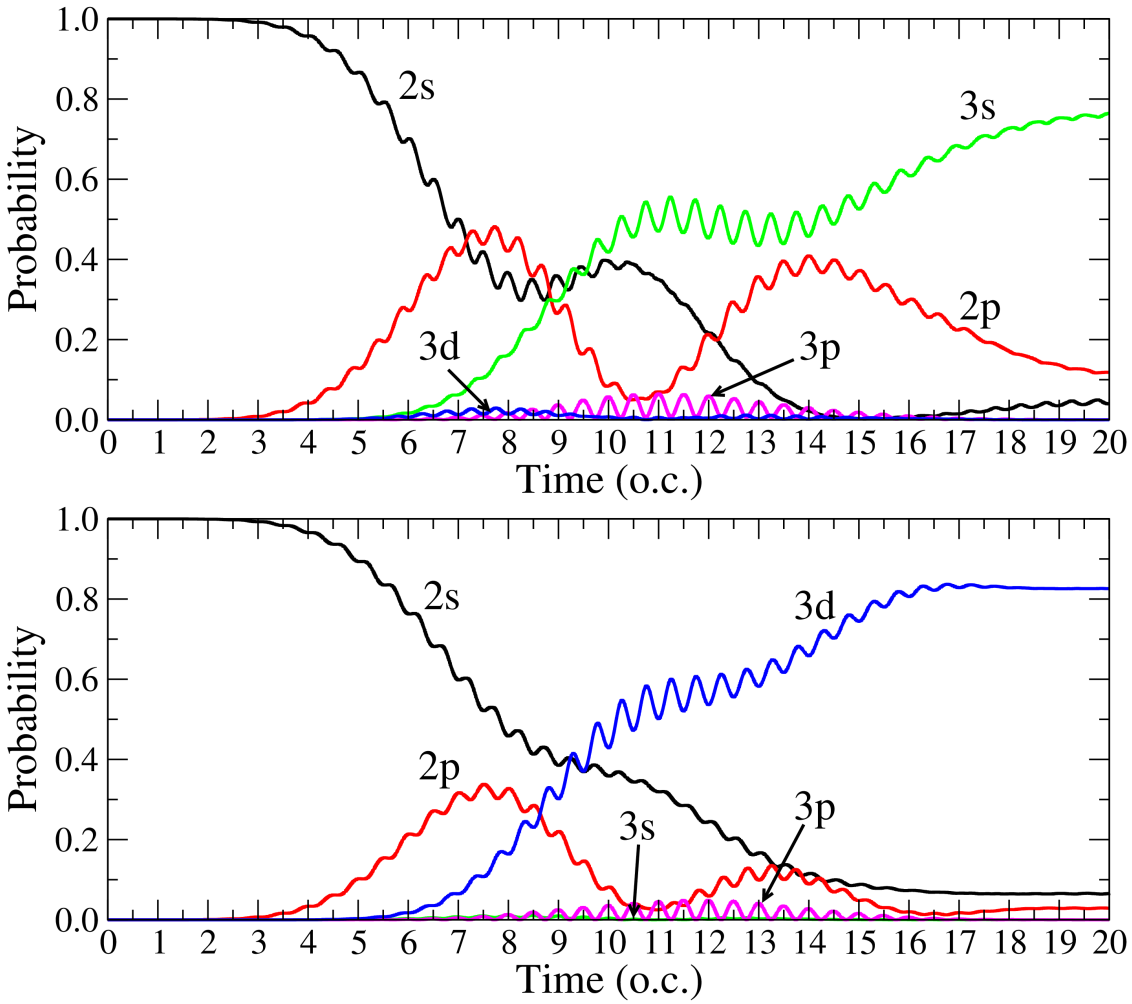

Figure 7.8: Time-dependent populations of the ground and several excited states of Li. The laser pulse has a $\sin^2$ shape, duration of 20 o.c., and peak intensity is 5×10^{11} W/cm^2. The carrier wavelength is 730 nm (upper panel) and 640 nm (lower panel).

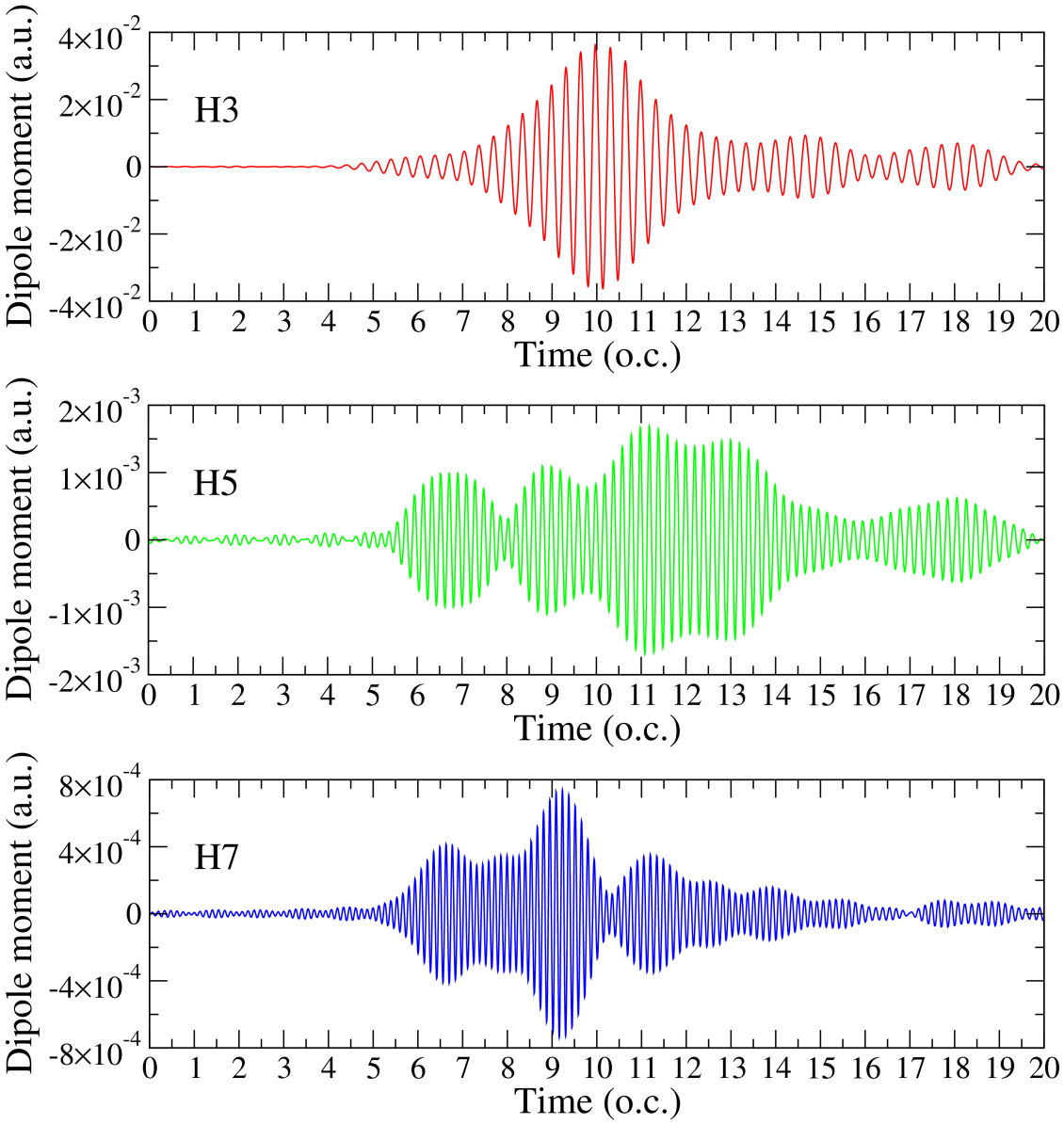

Figure 7.9: Time profiles of the 3rd, 5th, and 7th harmonics. The laser pulse has a $\sin^2$ shape, duration of 20 o.c., and peak intensity is 5×10^{11} W/cm^2. The carrier wavelength 730 nm corresponds to a two-photon Rabi-flopping regime between $2s$ and $3s$ states.

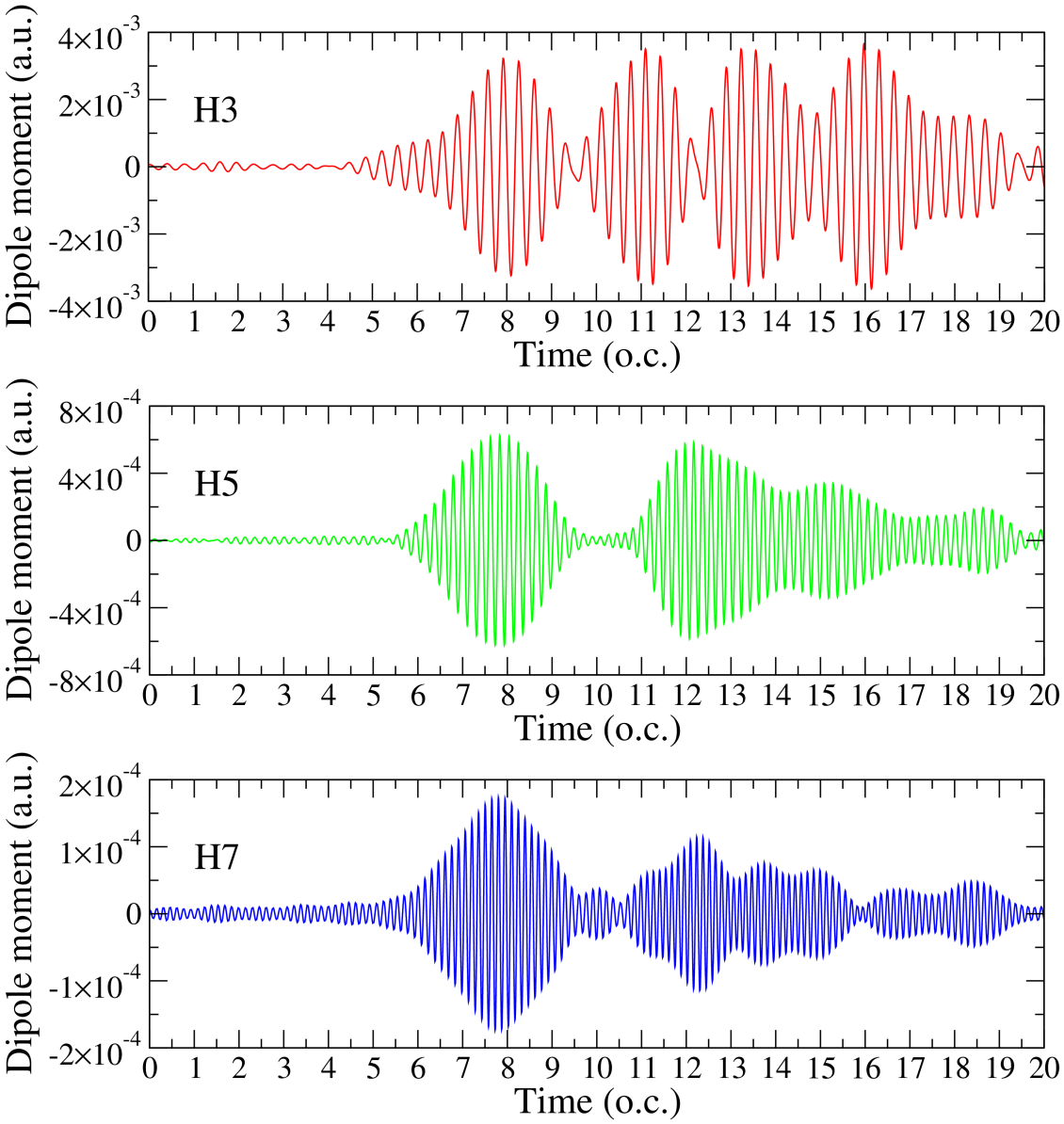

Figure 7.10: Time profiles of the 3rd, 5th, and 7th harmonics. The laser pulse has a $\sin^2$ shape, duration of 20 o.c., and peak intensity is 5×10^{11} W/cm^2. The carrier wavelength 640 nm corresponds to a two-photon Rabi-flopping regime between $2s$ and $3d$ states.

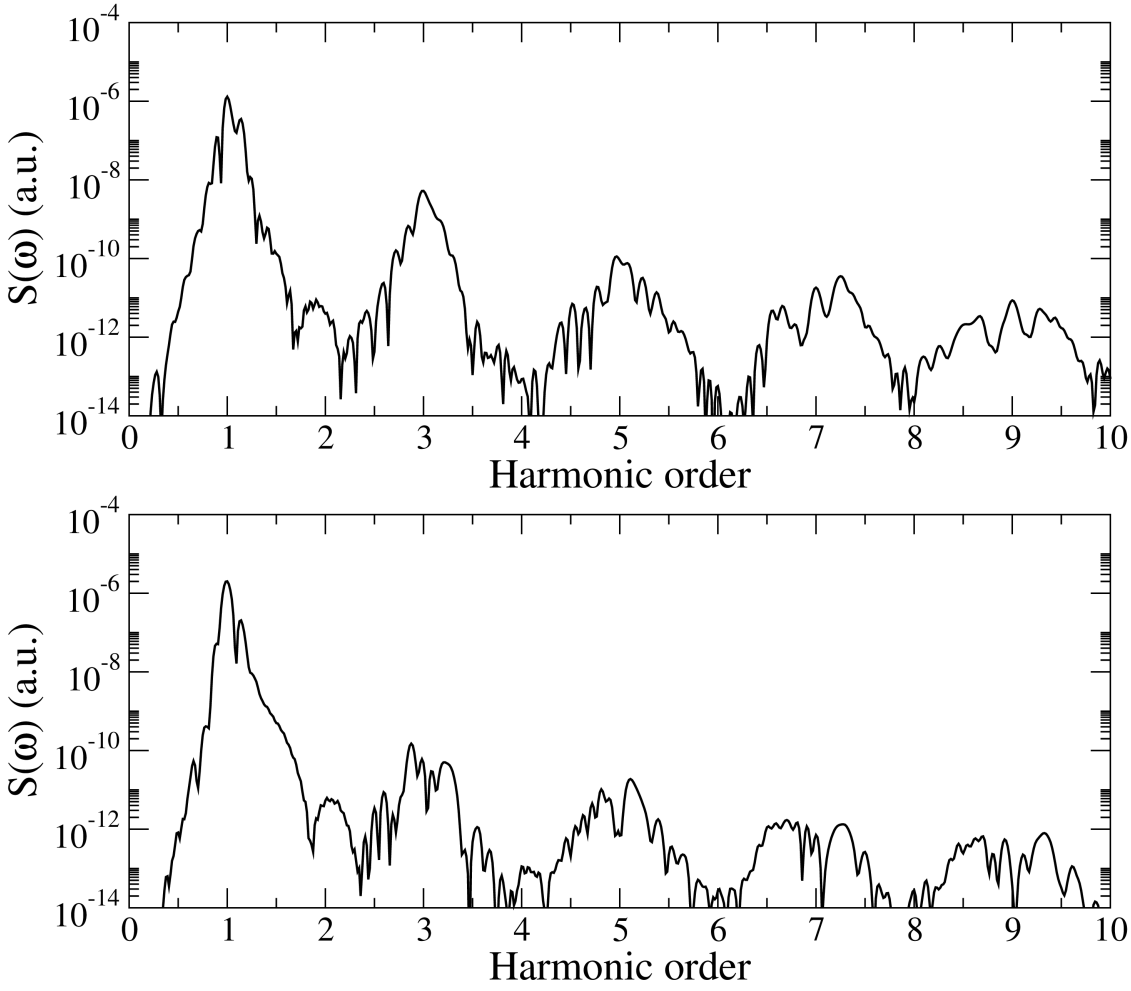

Figure 7.11: HG spectra of Li for the driving field wavelengths 730 nm (upper panel) and 640 nm (lower panel), corresponding to two-photon Rabi flopping. The laser pulse has a $\sin^2$ shape, duration of 20 o.c., and peak intensity is 5×10^{11} W/cm^2.

7.2.5 Two-photon Rabi flopping regime

The two-photon Rabi-flopping regime can be reached when the carrier frequency of the laser pulse is tuned into the two-photon resonance between the ground $2s$ state and excited $3s$ or $3d$ states. According to the data in Table 7.2, the corresponding wavelengths must be 748 and 650 nm. However, we have found that larger population transfers to the $3s$ and $3d$ states occur at slightly different carrier wavelengths, 730 and 640 nm, respectively. This may happen due to the interplay between the one-photon $2s-2p$ and two-photon resonance transitions, as well as because of slight difference between the one-electron Kohn-Sham and TDDFT excitation energies. In Fig. 7.8, we

show the time-dependent populations for the peak intensity of the laser pulse 5×10^{11} W/cm^2 and carrier wavelengths 730 and 640 nm. At the end of the laser pulse, the population inversion is observed, with the largest population in the $3s$ state (730 nm) and $3d$ state (640 nm). In the central part of the pulse, one can see a complex pattern with comparable populations of $2s$, $2p$, and $3s$ states at 730 nm and $2s$, $2p$, and $3d$ states at 640 nm. This population behavior is reflected in a more complex modulation of the dipole moments (see harmonic time profiles in Figs. 7.9 and 7.10) and additional fine structure of the harmonics in the frequency domain (Fig. 7.11) not seen in the case of one-photon Rabi flopping at the same peak intensity. At the carrier wavelength 730 nm, the time profile of the 3rd harmonic has a dominant maximum in the center of the laser pulse, while the time profiles of the 5th and 7th harmonics exhibit several maxima and modulations with the frequency higher than the Rabi frequency for the $2s-2p$ transition (see Fig. 7.9). Accordingly, in the HG spectrum (Fig. 7.11, upper panel) the 5th and 7th harmonics have complex multipeak structures while the 3rd harmonic is dominated by a single peak. At the wavelength 640 nm, the pattern is somewhat different. Here the time profile of the 3rd harmonic displays a deep low-frequency modulation with four distinct maxima (Fig. 7.10). This modulation is reflected in a clear multipeak structure of the 3rd harmonic in the frequency domain (Fig. 7.11, lower panel). The 5th harmonic in the time domain has two main maxima, corresponding to the modulation with the Rabi frequency (similar to that in the one-photon Rabi-flopping regime, see Fig. 7.4). In the frequency domain, this harmonic exhibits two distinct peaks separated by 2Ω, although a fine higher-frequency oscillatory structure is also present. Similar structures in the time and frequency domains are also observed in the 7th harmonic.

7.3 Conclusion

In this chapter, we have studied harmonic generation of the lithium atoms in one- and two-photon Rabi-flopping regimes where the population transfer from the ground $2s$ state to the excited $2p$, $3s$, and $3d$ states is substantial. The Li atoms interacting with strong laser fields are described

in the framework of the self-interaction-free time-dependent density-functional theory, taking into account dynamic multielectron response to the external field. Using the time-dependent generalized pseudospectral method with sufficient number of spatial grid points and time steps ensures the accuracy and efficiency of the computational procedure.

In the one-photon Rabi-flopping regime, when the carrier frequency of the driving field is tuned in the resonance between $2s$ and $2p$ states, the spectrum of emitted harmonic radiation exhibits a fine oscillatory structure, with the spacing between the adjacent subpeaks equal to twice the Rabi frequency. We have shown that this structure results from the low-frequency modulation of the time-dependent dipole moment. This modulation affects not only the fundamental frequency component of the dipole moment but also the higher frequency Fourier components. The low-frequency modulation of the dipole moment has its origin in the Rabi oscillations of the electronic population between the $2s$ and $2p$ states. Minima in the envelope function of the dipole moment are observed when the $2s$ or $2p$ population becomes extremely small. The number of the minima and their position on the time scale depend on the laser pulse area, that is the peak intensity and pulse duration.

When the peak intensity is increased, the pattern in the harmonic generation spectra becomes more complicated. First, since we study not a two-level system but a realistic multilevel atomic system, population transfer to other excited states becomes more significant with increasing intensity thus disrupting pure two-state Rabi oscillations. Second, the pulse-shape-induced interference effects also become more important at higher intensities. Using the concept of adiabatic Floquet states, we have shown that interference of the contributions to the harmonic generation spectra from the leading and trailing edges of the laser pulse also leads to oscillatory structures of the harmonic peaks but on a smaller frequency scale, well within the double Rabi frequency interval.

Increasing the peak intensity and changing the carrier frequency of the laser field, we can reach the two-photon Rabi-flopping regime. With the electronic structure of Li atoms, detuning the frequency by $\pm 10\%$ off the $2s-2p$ resonance, we can tune into $2s-3s$ or $2s-3d$ two-photon resonances. In this regime, depending on the frequency selected, the population transfer to the $3s$

or $3d$ states may be substantial. In the two-photon $2s-3s$ and $2s-3d$ transitions, the $2p$ energy level plays a role of an intermediate state. Since the detuning from the $2s-2p$ resonance is not very large, population of the $2p$ state may be significant, too. Then in the central part of the laser pulse the population is transferred among three different states ($2s$, $2p$, $3s$ or $2s$, $2p$, $3d$), and all these states may have comparable populations. Such a behavior of the electronic population is reflected in complex modulation patterns of the dipole moment and complex oscillatory structures of the harmonic peaks in the frequency domain.

Chapter 8

Future work

8.1 HHG in multielectron diatomic

We have presented ab *ab initio* high-precision study of high-order harmonic generation of the hydrogen molecular ion in intense elliptical polarized laser fields. The method discussed in the present work for the one-electron molecular ion, H_2^+ can be generalized for multielectron diatomic molecules with the help of the self-interaction-free time-dependent density functional theory [123, 23, 47]. For multielectron molecules, commonly used restriction to the highest-occupied molecular orbital may appear insufficient. Correct description of the HHG spectra in this case may require taking into account the inner-shell orbitals as well. Extension of the TDDFT for the study of HHG from multielectron diatomic molecules in EP laser fields is in progress.

We expect that even (as well as odd) below-threshold harmonic peaks in the HG spectra is not specific for H_2^+ only. The charge resonance effect, which favors generation of even harmonics, may take place in any odd-charged homonuclear molecular ions. For the multielectron targets, our theoretical and computational approach can be extended with the help of the self-interaction free time-dependent density functional theory[123, 47]. We should also note that the multipeak oscillatory pattern emerging in the harmonic generation spectra in the Rabi-flopping regime is not specific to the lithium atoms only. With appropriate adjustment of the laser pulse parameters, it

can also show up in other atomic and molecular targets with a similar structure of electronic energy levels.

8.2 Generalized Floquet formalism and the applications

For atoms and molecules in the presence of weak field, perturbative and diagrammatic methods are often used for non-resonant phenomena, whereas the rotating-wave approximation (RWA) is most commonly adopted for near-resonant processes. However, at intense field domain, this approach cannot be applied due to the existence of the anti-rotating terms and a.c. Stark shifts. The description of the response of atoms and molecules to monochromatic laser fields can be greatly facilitated by the use of the Floquet theorem. Many-mode Floquet theory (MMFT) approach [21] allows the transformation of the polychromatic time-dependent problem into an equivalent time-independent infinite-dimensional eigenvalue problem. Particularly detailed information on multiphoton transition probabilities, resonance shifts and widths, and line-shape characteristics can be obtained well beyond the RWA. Employing Floquet-Liouville supermatrix (FLSM) approach [21, 50, 52] allows us for a rigorous non-perturbative treatment of the time-dependent Liouville equation (quantum master equation) for the density-matrix operator of atoms and molecules, undergoing radiative and/or collisional relaxations polychromatic fields. By means of the MMFT [21], the TD-Liouville equation can be transformed into an equivalent time-independent FLSM eigenvalue problem [21]. This yields a powerful theoretical approach for the unified treatment of non-resonant and resonant, one- and multiple- photon, steady-state and transient phenomena in time-dependent high-order nonlinear optical processes, farther the RWA and traditional perturbative methods. The FLSM approach provides a valuable resource to study the multiphoton resonance fluorescence spectrum ; the time averaged power spectrum and the time-dependent physical spectrum in details for the density matrix of quantum systems undergoing relaxations (due to radiative decays and collisional damping, etc.), and exhibits novel new features in intense fields.

8.2.1 Floquet formalism in multiphoton process in solid state in presence of strong-field laser

My experience in atomic and molecular optics in subfemtosecond time scale metrology constitutes a powerful tool for exploring the dynamical evolution of not only gas-phase isolated atomic/molecular systems, but also fundamental electronic processes occurring on the attosecond timescale in the condensed matter systems. This is an emerging field with the potential to address fundamental problems of interest in atomic, molecular, and condensed matter physics. Excitation of solids in presence of strong laser field can lead to extremely nonlinear electronic and optical behavior. For instance, it has shown that HHG in solids and in dilute atomic gases take place essentially differently. But the underlying microscopic mechanisms in the solid and the difference from gas is still an open discussion. High density, periodicity and bonding and how they relate to atomic HHG, mechanism of tunneling across the direct band gap, roles of inter- and intraband dynamics is not clear yet. Since the theoretical results of multiphoton process is sensitive to details of the band structure through the interactions beyond nearest neighbors, choosing the right theoretical method to produce the correct results are significantly important. By extending our rigorous DFT method, we can calculate the band structure information and dipole transition elements and use them with the Floquet Hamiltonian technique to study the multiphoton excitation of solid. Considering lowest strongly coupled bands, as number of transition level of our system, the time-dependent Schrödinger equation transform into an equivalent infinite dimensional time-independent Floquet matrix eigenvalue problem. Then the transitions between the instantaneous, field-dressed, eigenstates of the system and dynamics of the electron in the system can be explained clearly. Equipped with these tools we can explore the electron dynamics in condensed matter in strong field.

8.2.2 Time-resolved four-wave Mixing(FWM) spectroscopy

Probing faster dynamics such as electronic motions requires shorter EUV pulses with a few femtosecond or even subfemtosecond duration. This can be accomplished using high order harmon-

ics (HH), which have have two distinctive properties: a broad spectral range spanning from the vacuum-ultraviolet (VUV) to the soft x-ray and regular spectral phase that supports extremely short light burst generation. Therefore, HH serve as an excellent FWM source with both wide wavelength tunability and unprecedented time resolution for triggering ultrafast dynamics [11, 30]. By extending the generalized Floquet theorem and the time-independent Floquet Hamiltonian, we can study the "nonlinear optical susceptibility in Four-wave mixing(XUV+NIR) in Argon/-Neon". Using Floquet-Liouville supermatrix (FLSM) approach, more detailed information about the density matrix of this quantum system undergoing relaxations due to radiative decays and also on the intensity-dependent nonlinear optical susceptibilities at the probe frequency are obtained. This nonlinear response is the essence of all nonlinear spectroscopies and the basis for developing new frequency light sources through nonlinear optical methods including frequency doubling and tripling, four-wave mixing (FWM), and high-order harmonic generation. The nonlinear response also underlies time-resolved studies of ultrafast dynamics in atoms, molecules, and solids.

8.2.3 Floquet formalism in dynamical decoupling or decoherence

Dynamical decoupling or decoherence is a main hindrance to the realization of any applications of quantum coherence, e.g., quantum information processing, quantum metrology, and quantum simulation. In fact, decoherence of dissipative systems couples tightly with the energy spectrum characters of the total system consisting of the system and its environment. In practical solid state systems, one generally addresses that it is hard to manipulate the spectral density via changing the spatial confinement once the material of system is fabricated. Thus a more efficient way in engineering the bound state than changing the spectral density is desired. Utilizing FLSM theory, and having information on the time averaged power spectrum and the time-dependent physical spectrum, we can find the control parameter to the decoherence suppression in the periodic driving external filed. In real open system the phenomena may take place in a chain of multilevel coupled system undergoing relaxation which can be resolved by adding the interaction coupling term with neighbors in the Floquet Hamiltonian as well.

8.2.4 Floquet formalism in dynamical localization

In all experimental systems with long-range interactions: trapped ions, polar molecules, Rydberg atoms, nitrogen-vacancy (NV) centers, and cavity QED, Floquet is a powerful approach to uncover the ongoing mechanism in the phenomenon of "dynamical localization," connected with the spectrum of the transition rate matrix. In these type of systems, Floquet states are greatly approved for a non-perturbative understanding of the processes induced by external field. Detailed information on multiphoton transition probabilities, resonance shifts and widths, and line-shape characteristics can be obtained much beyond the RWA. In cavity optomechanical system, FLSM can be extensively employed to solve the quantum master equations for the numerical simulations and exploring the electrodynamics. Taking advantage of FLSM, the characteristic power spectrum and the time evolution of physical spectrum for the density matrix of relaxing quantum systems can be explored in details.

8.2.5 Floquet formalism in topology (condensed matter)

Topology is one of the major considerations in modern condensed matter physics. It was believed that "topology is robust against perturbation", but later it was shown that if the electrons become photo-dressed then the Berry curvature, Chern number and the chiral edge state in almost ANY two dimensional multi-band systems can be disciplined or promoted by external time periodic fields such as laser. Employing Floquet theorem, we can show that the topology of the quasi-energy bands can be changed as a function of the laser intensity, polarization and frequency. From then we can control various phenomena connected to quantum localization, by tuning the amplitude or the frequency of the external drive. The idea of using Floquet formulation is not restricted to an electron-laser system, but can be universally applied to several physical systems, such as electron-coherent phonon, photon-optical wave guide, cold atom-optical lattice etc. In fact, this formulation bridge the topological insulators, laser physics and nonequilibrium statistical mechanics and push them in forefront research.

References

[sup] *See Supplemental Material at URL for the evolution of the electron density within one optical cycle*.

[2] Abramowitz, E. M. & Stegunz, I. (1965). *Handbook of Mathematical Functions*. New York: Dover.

[3] Agostini, P., Fabre, F., Mainfray, G., Petite, G., & Rahman, N. K. (1979). *Phys. Rev. Lett.*, 42, 1127.

[4] Alon, O. E., Averbukh, V., & Moiseyev, N. (1998).

[5] Anwar-ul Haq, M., Mahmood, S., Riaz, M., Ali, R., & Baig, M. A. (2005). *J. Phys. B*, 38(2), S77–S86.

[6] Bavli, R. & Metiu, H. (1993). *Phys. Rev. A*, 47, 3299.

[7] Bergmann, K., Theuer, H., & Shore, B. W. (1998). *Rev. Mod. Phys.*, 70, 1003–1025.

[8] Bian, X. B. & Bandrauk, A. D. (2012). *Phys. Rev. Lett.*, 108, 263003.

[9] Budil, K. S., Salières, P., L'Huillier, A., Ditmire, T., & Perry, M. D. (1993). *Phys. Rev. A*, 48, R3437–R3440.

[10] Burnett, N. H., Kan, C., & Corkum, P. B. (1995). *Phys. Rev. A*, 51, R3418–R3421.

[11] Cao, W., Warrick, E. R., Fidler, A., Leone, S. R., & Neumark, D. M. (2016). *Phys. Rev. A*, 94, 021802.

[12] Carrera, J. J. & Chu, S. I. (2007). *J. Phys. Chem. A*, 111, 9320–9325.

[13] Casida, M. E. (1995). In D. P. Chong (Ed.), *Recent Advances in Density Functional Methods, Part I* (pp. 155). Singapore: World Scientific.

[14] Castiglia, G., Corso, P. P., Daniele, R., Fiordilino, E., Morales, F., & Orlando, G. (2007). *Laser Physics*, 17, 1240.

[15] Chang, Z. & Corkum, P. (2010). *J. Opt. Soc. Am. B*, 27(11), B9–B17.

[16] Chini, M., Wang, X., Cheng, Y., Wang, H., Wu, Y., Cunningham, E., Li, P.-C., Heslar, J., Telnov, D. A., Chu, S. I., & Chang, Z. (2014). Coherent phase-matched vuv generation by field-controlled bound states. *Nature Photonics*, 8, 437.

[17] Chini, M., Wang, X., Cheng, Y., Wu, Y., Zhao, D., Telnov, D. A., Chu, S.-I., & Chang, Z. (2013). *Sci. Rep.*, 3, 1105.

[18] Chu, S. I. (1989). *Adv. Chem. Phys.*, 73, 739–799.

[19] Chu, S.-I. (2005). *J. Chem. Phys.*, 123(6), 062207.

[20] Chu, S. I. & Telnov, D. A. (2004a). *Phys. Rep.*, 390, 1.

[21] Chu, S. I. & Telnov, D. A. (2004b). *Phys. Rep.*, 390, 1–131.

[22] Chu, X. & Chu, S.-I. (2000). *Phys. Rev. A*, 63, 013414.

[23] Chu, X. & Chu, S. I. (2001). *Phys. Rev. A*, 63, 013414.

[24] Chui, C. K. (1992). *An Introduction to Wavelets*. New York: Academic Press.

[25] Ciappina, M. F., Pérez-Hernández, J. A., Landsman, A. S., Zimmermann, T., Lewenstein, M., Roso, L., & Krausz, F. (2015). *Phys. Rev. Lett.*, 114, 143902.

[26] Corkum, P. B. (1993). *Phys. Rev. Lett.*, 71, 1994–1997.

[27] Corso, P. P., Fiordilino, E., Orlando, G., & Persico, F. (2007). *J. Mod. Optics*, 54, 1387–1393.

[28] Das, T., Augstein, B. B., & Figueira de Morisson Faria, C. (2013). *Phys. Rev. A*, 88, 023404.

[29] Dietrich, P., Burnett, N. H., Ivanov, M., & Corkum, P. (1994). *Phys. Rev. A*, 50, R3585.

[30] Ding, T., Ott, C., Kaldun, A., Blättermann, A., Meyer, K., Stooss, V., Rebholz, M., Birk, P., Hartmann, M., Brown, A., Hart, H. V. D., & Pfeifer, T. (2016). *Opt. Lett.*, 41(4), 709–712.

[31] Dudin, Y. O., Li, L., Bariani, F., & Kuzmich, A. (2012). *Nature Physics*, 8, 790–794.

[32] Dudovich, N., Polack, T., Pe'er, A., & Silberberg, Y. (2005). *Phys. Rev. Lett.*, 94, 083002.

[33] Eden, J. (2004). *Progress in Quantum Electronics*, 28(3–4), 197 – 246.

[34] Eden, J. (2005). *Progress in Quantum Electronics*, 29(3–5), 257 – 260.

[35] Fainshtein, A. G., Manakov, N. L., Ovsiannikov, V. D., & Rapoport, L. P. (1992). *Phys. Rep.*, 210(3), 111–221.

[36] Fleischer, A., Gupta, A. K., & Moiseyev, N. (2005). *International Journal of Quantum Chemistry*, 103(6), 824–840.

[37] Fleischer, A. & Moiseyev, N. (2005). *Phys. Rev. A*, 72, 032103.

[38] Fleischer, A. & Moiseyev, N. (2006). *Phys. Rev. A*, 74, 053806.

[39] Frolov, M. V., Manakov, N. L., Sarantseva, T. S., & Starace, A. F. (2012). *Phys. Rev. A*, 86, 063406.

[40] Frumker, E., Hebeisen, C. T., Kajumba, N., Bertrand, J. B., Wörner, H. J., Spanner, M., Villeneuve, D. M., Naumov, A., & Corkum, P. B. (2012). *Phys. Rev. Lett.*, 109, 113901.

[41] Fuks, J. I., Farzanehpour, M., Tokatly, I. V., Appel, H., Kurth, S., & Rubio, A. (2013). *Phys. Rev. A*, 88, 062512.

[42] Fuks, J. I., Helbig, N., Tokatly, I. V., & Rubio, A. (2011). *Phys. Rev. B*, 84, 075107.

[43] Fushitani, M., Liu, C.-N., Matsuda, A., Endo, T., Toida, Y., Nagasono, M., Togashi, T., Yabashi, M., Ishikawa, T., Hikosaka, Y., Morishita, T., & Hishikawa, A. (2016). *Nat. Photon.*, 10(0), 102.

[44] Goulielmakis, E., Schultze, M., Hofstetter, M., Yakovlev, V. S., Gagnon, J., Uiberacker, M., Aquila, A. L., Gullikson, E. M., Attwood, D. T., Kienberger, R., Krausz, F., & Kleineberg, U. (2008). *Science*, 320, 1614.

[45] Henkel, J., Witting, T., Fabris, D., Lein, M., Knight, P. L., Tisch, J. W. G., & Marangos, J. P. (2013). *Phys. Rev. A*, 87, 043818.

[46] Hentschel, M., Kienberger, R., Spielmann, C., Reider, G. A., Milosevic, N., Brabec, T., Corkum, P., Heinzmann, U., Drescher, M., & Krausz, F. (2001). *Nature*, 414, 509".

[47] Heslar, J., Telnov, D., & Chu, S.-I. (2011). *Phys. Rev. A*, 83, 043414.

[48] Heslar, J., Telnov, D. A., & Chu, S.-I. (2013). *Phys. Rev. A*, 87(5), 052513.

[49] Heslar, J., Telnov, D. A., & Chu, S.-I. (2015). *Phys. Rev. A*, 91(2), 023420.

[50] Ho, T. S. & Chu, S. I. (1985). *Chem. Phys. Lett.*, 122(4), 327–332.

[51] Ho, T.-S. & Chu, S.-I. (1987). *Chem. Phys. Lett.*, 141(4), 315 – 322.

[52] Ho, T. S., Wang, K., & Chu, S. I. (1986). *Phys. Rev. A*, 33, 1798–1816.

[53] Hostetter, J. A., Tate, J. L., Schafer, K. J., & Gaarde, M. B. (2010). *Phys. Rev. A*, 82, 023401.

[54] Huber, B., Baluktsian, T., Schlagmüller, M., Kölle, A., Kübler, H., Löw, R., & Pfau, T. (2011). *Phys. Rev. Lett.*, 107, 243001.

[55] Hughes, S. (1998). *Phys. Rev. Lett.*, 81(16), 3363.

[56] Itatani, J., Levesque, J., Zeidler, D., Niikura, H., Pépin, H., Kieffer, J. C., Corkum, P. B., & Villeneuve, D. M. (2004). *Nature*, 432, 867.

[57] Ivanov, M. Y., Brabec, T., & Burnett, N. (1996). *Phys. Rev. A*, 54, 742–745.

[58] Jin, Y.-J., Tong, X.-M., & Toshima, N. (2010). *Phys. Rev. A*, 81, 013408.

[59] Johnson, T. A., Urban, E., Henage, T., Isenhower, L., Yavuz, D. D., Walker, T. G., & Saffman, M. (2008). *Phys. Rev. Lett.*, 100, 113003.

[60] Jooya, H. Z., Telnov, D. A., Li, P.-C., & Chu, S. I. (2015). *Phys. Rev. A*, 91, 063412.

[61] Kakehata, M., Takada, H., Yumoto, H., & Miyazaki, K. (1997). *Phys. Rev. A*, 55, R861–R864.

[62] Kazansky, A. K. & Telnov, D. A. (1988). *Sov. Phys. - JETP*, 67(2), 253–256.

[63] Khan, S. D., Cheng, Y., Möller, M., Zhao, K., Zhao, B., Chini, M., Paulus, G. G., , & Chang, Z. (2011). *Appl. Phys. Lett.*, 99, 161106.

[64] Kittelmann, O., Ringling, J., Nazarkin, A., Korn, G., & Hertel, I. V. (1996). *Phys. Rev. Lett.*, 76, 2682–2685.

[65] Kopold, R., Becker, W., & Kleber, M. (1998). *Phys. Rev. A*, 58, 4022–4038.

[66] Kozlov, M., Kfir, O., Fleischer, A., Kaplan, A., Carmon, T., Schwefel, H. G. L., Barta, G., & Cohen, O. (2012). *New Journal of Physics*, 14, 063036.

[67] Krausz, F. & Ivanov, M. (2009). *Rev. Mod. Phys.*, 81, 163.

[68] Krieger, J. B., Li, Y., & Iafrate, G. J. (1992). *Phys. Rev. A*, 45(1), 101.

[69] Kulander, K. C., Schafer, K. J., & Krause, J. L. (1993). *Dynamics of Short-Pulse Excitation, Ionization and Harmonic Conversion*, (pp. 95–110). Springer US: Boston, MA.

[70] Landau, L. D. & Lifshitz, E. M. (1975). *The classical theory of fields*. Oxford: Pergamon Press.

[71] Lee, S., Lim, J., Ahn, J., Hakobyan, V., & Guérin, S. (2010). *Phys. Rev. A*, 82, 023408.

[72] Lein, M., Hay, N., Velotta, R., Marangos, J. P., & Knight, P. L. (2002). *Phys. Rev. A*, 66, 023805.

[73] Leone, S. R., McCurdy, C. W., Burgdorfer, J., Cederbaum, L. S., Chang, Z., Dudovich, N., Feist, J., Greene, C. H., Ivanov, M., Kienberger, R., Keller, U., Kling, M. F., Loh, Z.-H., Pfeifer, T., Pfeiffer, A. N., Santra, R., Schafer, K., Stolow, A., Thumm, U., & Vrakking, M. J. J. (2014). *Nature Photonic*, 8, 162.

[74] Lewenstein, M., Balcou, P., Ivanov, M. Y., L'Huillier, A., & Corkum, P. B. (1994). *Phys. Rev. A*, 49, 2117–2132.

[75] Li, P.-C., Sheu, Y.-L., Laughlin, C., & Chu, S.-I. (2015). *Nature Communications*, 6, 7178.

[76] Li, W., Zhou, X., Lock, R., Patchkovskii, S., Stolow, A., Kapteyn, H. C., & Murnane, M. M. (2008). *Science*, 322, 1207.

[77] Liang, Y., Augst, S., Chin, S. L., Beaudoin, Y., & Chaker, M. (1994). *Journal of Physics B: Atomic, Molecular and Optical Physics*, 27(20), 5119.

[78] Liu, J.-C., Kohler, M. C., Keitel, C. H., & Hatsagortsyan, K. Z. (2011). *Phys. Rev. A*, 84, 063817.

[79] Mainfray, G. & Manus, C. (1991). *Rep. Prog. Phys.*, 54, 1333.

[80] Martín, F., Fernández, J., Havermeier, T., Foucar, L., Weber, T., Kreidi, K., Schöffler, M., Schmidt, L., Jahnke, T., Jagutzki, O., Czasch, A., Benis, E. P., Osipov, T., Landers, A. L., Belkacem, A., Prior, M. H., Schmidt-Böcking, H., Cocke, C. L., & Dörner, R. (2007). *Science*, 315(5812), 629–633.

[81] Martín, F., Fernández, J., Havermeier, T., Foucar, L., Weber, T., Kreidi, K., Schöffler, M., Schmidt, L., Jahnke, T., Jagutzki, O., Czasch, A., Benis, E. P., Osipov, T., Landers, A. L.,

Belkacem, A., Prior, M. H., Schmidt-Böcking, H., Cocke, C. L., & Dörner, R. (2007). *Science*, 315(5812), 629–633.

[82] Meckel, M., Comtois, D., Zeidler, D., Staudte, A., Pavičić, D., Bandulet, H. C., Pépin, H., Kieffer, J. C., Dörner, R., Villneuve, D. M., & Corkum, P. B. (2008). *Science*, 320, 1478.

[83] Milošević, D. B., Becker, W., & Kopold, R. (2000). *Phys. Rev. A*, 61, 063403.

[84] Mittleman, M. H. (1992). *Theory of Laser Atom Interaction*. New York: Plenum.

[85] Miyazaki, K. & Takada, H. (1995). *Phys. Rev. A*, 52, 3007–3021.

[86] Moiseyev, N. & Lein, M. (2003). *J. Phys. Chem. A*, 107, 7181.

[87] Moiseyev, N. & Weinhold, F. (1997). *Phys. Rev. Lett.*, 78, 2100–2103.

[88] Moller, M., Cheng, Y., Khan, S. D., Zhao, B., Zhao, K., Chini, M., Paulus, G. G., & Chang, Z. (2012). *Phys. Rev. A*, 86, 011401.

[89] Monmayrant, A., Chatel, B., & Girard, B. (2006). *Phys. Rev. Lett.*, 96, 103002.

[90] Morishita, T. & Lin, C. D. (2013). *Phys. Rev. A*, 87, 063405.

[91] Mücke, O. D., Tritschler, T., Wegener, M., Morgner, U., & Kärtner, F. X. (2001). *Phys. Rev. Lett.*, 87, 057401.

[92] Mulliken, R. S. (1939). *J. Chem. Phys.*, 7, 20.

[93] Mundt, M., Kümmel, S., van Leeuwen, R., & Reinhard, P.-G. (2007). *Phys. Rev. A*, 75(5), 050501.

[94] Paolo Corso, P., Fiordilino, E., orlando, G., & Persico, F. (2007). *Journal of Modern Optics*, 54, 1387.

[95] Paul, P. M., Toma, E. S., Breger, P., Mullot, G., Augé, F., Balcou, P., Muller, H. G., & Agostini, P. (2001). *Science*, 292, 689.

[96] Paulus, G. G., Nicklich, W., Xu, H., Lambropoulos, P., & Walther, H. (1994). *Phys. Rev. Lett.*, 72, 2851.

[97] Perdew, J. P. & Zunger, A. (1981). *Phys. Rev. B*, 23(10), 5048–5079.

[98] Petersilka, M., Gossmann, U. J., & Gross, E. K. U. (1996). *Phys. Rev. Lett.*, 76, 1212–1215.

[99] Posthumus, J. H. (2004). *Rep. Prog. Phys.*, 67, 623.

[100] Power, E. P., March, A. M., Catoire, F., Sistrunk, E., Krushelnick, K., Agostini, P., & DiMauro, L. F. (2010). *Nature Photonics*, 4, 352.

[101] Rabi, I. I. (1937). *Phys. Rev.*, 51, 652–654.

[102] Radziemski, L. J., Engleman Jr, R., & Brault, J. W. (1995). *Phys. Rev. A*, 52(6), 4462.

[103] Ray, D., Ulrich, B., Bocharova, I., Maharjan, C., Ranitovic, P., Gramkow, B., Magrakvelidze, M., De, S., Litvinyuk, I., Le, A. T., Morishita, T., Lin, C. D., Paulus, G. G., & Cocke, C. L. (2008). *Phys. Rev. Lett.*, 100, 143002.

[104] Reetz-Lamour, M., Amthor, T., Deiglmayr, J., & Weidemüller, M. (2008). *Phys. Rev. Lett.*, 100, 253001.

[105] Rickes, T., Yatsenko, L. P., Steuerwald, S., Halfmann, T., Shore, B. W., Vitanov, N. V., & Bergmann, K. (2000). *The Journal of Chemical Physics*, 113(2), 534–546.

[106] Roguś, D. & Lewenstein, M. (1986). *J. Phys. B*, 19(19), 3051.

[107] Ruggenthaler, M. & Bauer, D. (2009). *Phys. Rev. Lett.*, 102, 233001.

[108] Rzazewski, K. & Florjanczyk, M. (1984). *J. Phys. B*, 17(15), L509.

[109] Rzazewski, K., Zakrzewski, J., Lewenstein, M., & Haus, J. W. (1985). *Phys. Rev. A*, 31(5), 2995–3002.

[110] Saffman, M., Walker, T. G., & Mølmer, K. (2010). *Rev. Mod. Phys.*, 82, 2313–2363.

[111] Safronova, M. S., Safronova, U. I., & Clark, C. W. (2012). *Phys. Rev. A*, 86(4), 042505.

[112] Sansone, G., Benedetti, E., Calegari, F., Vozzi, C., Avaldi, L., Flammini, R., Poletto, L., Villoresi, P., Altucci, C., Velotta, R., Stagira, S., De Silvestri, S., & Nisoli, M. (2006). Isolated Single-Cycle Attosecond Pulses. *Science*, 314(5798), 443–446.

[113] Schafer, K. J. (2008). Numerical methods in strong field physics. In T. Brabec (Ed.), *Strong Field Laser Physics* (pp. 111). New York: Springer.

[114] Schultze, M., Fieß, M., Karpowicz, N., Gagnon, J., Korbman, M., Hofstetter, M., Neppl, S., Cavalieri, A. L., Komninos, Y., Mercouris, T., Nicolaides, C. A., Pazourek, R., Nagele, S., Feist, J., Burgdörfer, J., Azzeer, A. M., Ernstorfer, R., Kienberger, R., Kleineberg, U., Goulielmakis, E., Krausz, F., & Yakovlev, V. S. (2010). *Science*, 328, 1658.

[115] Shafir, D., Mairesse, Y., Villeneuve, D. M., Corkum, P. B., & Dudovich, N. (2009). *Nature Physics*, 5(6), 412–416.

[116] Smirnova, O., Mairesse, Y., Patchkovskii, S., Dudovich, N., Villeneuve, D., Corkum, P., & Ivanov, M. Y. (2009). *Nature*, 460(7258), 972–977.

[117] Soifer, H., Botheron, P., Shafir, D., Diner, A., Raz, O., Bruner, B. D., Mairesse, Y., Pons, B., & Dudovich, N. (2010). *Phys. Rev. Lett.*, 105, 143904.

[118] Takemoto, N. & Becker, A. (2010). *Phys. Rev. Lett.*, 105, 203004.

[119] Takemoto, N. & Becker, A. (2011). *Phys. Rev. A*, 84, 023401.

[120] Telnov, D. A. & Chu, S. I. (1995). *J. Phys. B*, 28, 2407.

[121] Telnov, D. A. & Chu, S. I. (2005). *Phys. Rev. A*, 71, 013408.

[122] Telnov, D. A. & Chu, S.-I. (2007). *Phys. Rev. A*, 76, 043412.

[123] Telnov, D. A. & Chu, S.-I. (2009). *Phys. Rev. A*, 80, 043412.

[124] Telnov, D. A., Heslar, J. T., & Chu, S.-I. (2011). *Chem. Phys.*, 391(1), 88–91.

[125] Telnov, D. A., Sosnova, K. E., Rozenbaum, E., & Chu, S. I. (2013). *Phys. Rev. A*, 87, 053406.

[126] Telnov, D. A., Wang, J., & Chu, S. I. (1995). *Phys. Rev. A*, 52, 3988.

[127] Thiele, M., Gross, E. K. U., & Kümmel, S. (2008). *Phys. Rev. Lett.*, 100(15), 153004.

[128] Tong, X. M. & Chu, S. I. (1997a). *Chem. Phys.*, 217, 119.

[129] Tong, X.-M. & Chu, S.-I. (1997b). *Phys. Rev. A*, 55(5), 3406.

[130] Tong, X.-M. & Chu, S.-I. (1998). *Phys. Rev. A*, 57(1), 452.

[131] Tong, X.-M. & Chu, S.-I. (2000). *Phys. Rev. A*, 61, 021802.

[132] Trallero-Herrero, C., Cohen, J. L., & Weinacht, T. (2006). *Phys. Rev. Lett.*, 96, 063603.

[133] Ullrich, C. A., Gossmann, U. J., & Gross, E. K. U. (1995). *Phys. Rev. Lett.*, 74(6), 872.

[134] Vignale, G. (1995). *Phys. Rev. Lett.*, 74(16), 3233.

[135] Xiong, W.-H., Geng, J.-W., Tang, J.-Y., Peng, L.-Y., & Gong, Q. (2014). *Phys. Rev. Lett.*, 112, 233001.

[136] Yost, D. C., Schibli, Ye, J., Tate, J. L., Hostetter, J., Gaarde, M. B., & Schafer, K. J. (2009). *Nature Phys.*, 5, 815.